LATTICE DETERMINATION OF THE LEADING ORDER HADRONIC CONTRIBUTION TO THE ANOMALOUS MAGNETIC MOMENT OF THE MUON

DIPLOMARBEIT IM FACHBEREICH PHYSIK

BENJAMIN JÄGER

Institut für Kernphysik
Johannes Gutenberg Universität Mainz

23.09.2010

CONTENTS

Part I

INTRODUCTION

1

OVERVIEW

The anomalous magnetic moment of the muon $a_\mu \equiv \frac{g_\mu - 2}{2}$ is probably one of the most precisely measured quantities in physics and therefore the object of high precision experiments and theoretical calculations. Experiments are able to determine this quantity with high accuracy up to the ppm level, and therefore a_μ is sensitive to physics beyond the *Standard Model of Particle Physics* (SM). Indeed a_μ shows a disagreement between theoretical predictions and experiments of 3.2 standard derivations. This could be a first sign of new physics, so there are many efforts to reduce the uncertainties of experiments and theoretical calculations. Chapter 3 gives an overview of the results from experiments and the prediction by SM interactions.

This work will consider the hadronic contribution to the anomalous magnetic moment of the muon resulting from strong interactions, which are described by Quantum ChromoDynamics (QCD). Since the hadronic contribution to a_μ is of the same order as experimental sensitivity, whether or not the tension of 3.2 σ persist, depends on the accuracy with which this contribution is known theoretically. Usually the hadronic contribution is determined in a semi-phenomenological approach, using the experimentally determined cross sections for $e^+e^- \to$ hadrons. This approach needs an independent theoretical calculation to confirm the phenomenological estimate. QCD at a low energy regime cannot be expanded perturbatively, so other techniques are needed. Lattice QCD is an *ab initio* method to treat strong interactions non-perturbatively and has shown to deliver accurate results for a lot of quantities in physics. A brief introduction to Lattice QCD, concentrating on topics relevant for this work, is shown in chapter 2.

2

LATTICE QCD

Quantum Chromo Dynamics (QCD) has been generally accepted as the theory describing the strong interactions, one of four fundamental forces in nature. QCD is a non-Abelian gauge theory with a SU(3)-color-symmetry. The constituents of this model are the spin-1/2 particles called *quarks*, and the force-mediating bosons are called *gluons*. Quarks occur in 6 different flavors[1] with 3 different colors. These colors can be considered as the charges of QCD. The gluons are massless bosons which couple to the color. Since gluons carry color and anti-color, they can couple to themselves. The Lagrangian $\mathscr{L}$ of QCD can be formally written as:

$$\mathscr{L} = -\frac{1}{2g_0^2}\mathrm{Tr}\,(F_{\mu\nu}F_{\mu\nu}) + \sum_{f=u,d,s,\ldots} \bar{\psi}_f(\gamma_\mu D_\mu + m_f)\psi_f. \tag{2.1}$$

The sum in equation (2.1) is performed over all quark flavors ψ_f. The gluons are represented by the gauge fields A_μ, which form the field strength tensor $F_{\mu\nu}$:

$$F_{\mu\nu} = \partial_\mu A_\nu - \partial_\nu A_\mu + [A_\mu, A_\nu]\ , \quad A_\mu^\dagger = A_\mu. \tag{2.2}$$

Because of the non-vanishing commutator in equation (2.2), the field strength tensor includes self-interaction of the gauge fields. D_μ is the covariant derivative ensuring local gauge invariance of the Lagrangian:

$$D_\mu = \partial_\mu + A_\mu. \tag{2.3}$$

In the high-energy regime the coupling becomes weak, so perturbation theory can be applied. This behavior is referred as *asymptotic freedom* [1] and its discovery was rewarded with the 2004 Nobel prize in physics.

In the low-energy regime the coupling increases to the order of 1, so a perturbative expansion in powers of the coupling is useless. In this region the quarks are said to be confined. *Confinement* provides an explanation why quarks cannot be observed as free particles. All possible hadronic states have to be color singlets, so the simplest combination of quarks are mesons $\bar{q}q$ and baryons qqq. These combinations form the building blocks for almost every observed particle in nature.

2.1 INTRODUCTION

"Lattice QCD is the non-perturbative approach to the gauge theory of the strong interaction through regularized, Euclidean functional integrals. The regularization is based on a discretization of the QCD action which preserves gauge invariance at all stages." [2]

1 The quark flavors are: up, down, charm, strange, top, bottom.

This summary contains all necessary ingredients. The lattice QCD approach is based on Euclidean functional integral, which allows to construct the theory from first principles. The input parameters for this theory are the strong coupling constant and the masses of the quarks. So the lattice approach delivers an *ab initio* method treating QCD. The Euclidean metric is obtained by rotating the time in Minkoswki spacetime to imaginary times ($t \to -it$), a procedure called Wick rotation. This ensures that the metric is positive definite $g_{\mu\nu} = \delta_{\mu\nu}$. As a consequence, there is no difference between a covariant or contravariant vector. The Euclidean functional integral connects quantum field theory to statistical mechanics, where it corresponds to a partition function in the canonical ensemble. This correspondence allows the usage of Monte Carlo integration schemes to "measure" expectation values of physical observables in the quantum theory on a computer. To this end spacetime is discretized by introducing a hypercubic lattice, which makes the measure well-defined, finite and calculable, so no gauge fixing is needed in order to regularize the theory.

In the following a brief introduction to lattice QCD is shown, following the lines of [2][2].

2.2 SCALAR ϕ^4 THEORY

To keep things simple, a scalar ϕ^4 theory is used to establish the lattice techniques. The action of the model is given by:

$$S_E[\phi] = \int d^4x \left(\frac{1}{2}\partial_\mu\phi(x)\partial_\mu\phi(x) + \frac{1}{2}m^2\phi(x)^2 + \frac{\lambda}{4!}\phi(x)^4 \right). \tag{2.4}$$

Spacetime is discretized by the introduction of a hypercubic lattice

$$\Lambda = \left\{ x \in \mathbb{R}^4 \,|\, x_0/a = 1, \dots, T\,;\, x_i/a = 1, \dots, L\,;\, i = 1, \dots, 3 \right\}. \tag{2.5}$$

The quantity a is known as the lattice spacing, which is the minimal step in a time or space direction. So there are $T \cdot L^3$ lattice sites which form a physical volume of $a^4 T \cdot L^3$. The next step is to quantize the action by introducing a discrete derivative:

$$d_\mu\phi(x) = \frac{1}{a}\left(\phi(x + a\hat{\mu}) - \phi(x)\right), \tag{2.6}$$

$$d^*_\mu\phi(x) = \frac{1}{a}\left(\phi(x) - \phi(x - a\hat{\mu})\right). \tag{2.7}$$

Inserting these discrete derivatives in the action yields:

$$S_E[\phi] = a^4 \sum_{x\in\Lambda} \left(\frac{1}{2}d_\mu\phi(x)d_\mu\phi(x) + \frac{1}{2}m^2\phi(x)^2 + \frac{\lambda}{4!}\phi(x)^4 \right). \tag{2.8}$$

2 A more detailed introduction to lattice QCD can be found in various textbooks [3, 4, 5, 6].

Here the introduction of the hypercubic lattice Λ changed the integral to a discrete sum over all lattice sites. The theory is quantized by the functional integral in the following way:

$$Z_E = \int D[\phi] e^{-S_E[\phi]}, \quad D[\phi] = \prod_{x \in \Lambda} d\phi(x). \tag{2.9}$$

The introduction of the Euclidean metric changed the oscillating factor e^{iS} to a peaked *weight* factor e^{-S}, which can be numerically determined using *importance sampling*. The introduction of a hypercubic lattice reduces the functional integral to a multi-dimensional integration. Correlation functions are now connected to the Euclidean correlation functions:

$$\langle \phi(x_1) \dots \phi(x_n) \rangle = \frac{1}{Z_E} \int D[\phi] \phi(x_1) \dots \phi(x_n) e^{-S_E[\phi]}. \tag{2.10}$$

All operators that can be expressed in powers of the field ϕ, are thus accessible using equation (2.10).

2.3 QCD ON THE LATTICE

From equation (2.1) the continuum action of QCD can be read off:

$$S_{QCD} = \int d^4x \left(-\frac{1}{2g_0^2} \mathrm{Tr}\,(F_{\mu\nu} F^{\mu\nu}) + \sum_{f=u,d,s,\dots} \bar{\psi}_f (\gamma_\mu D_\mu + m_f) \psi_f \right). \tag{2.11}$$

The next step is the discretization of the derivative and the integral in equation (2.11). The naïve replacement of $\partial_\mu \to d_\mu$ violates the transformation law:

$$A_\mu(x) \to g(x) A_\mu(x) g(x)^{-1} + g(x) \partial_\mu g(x)^{-1}, \; g(x) \in SU(3). \tag{2.12}$$

It is shown below, that a consistent formulation can be achieved using the parallel transporter instead of the more familiar gauge potential A_μ.

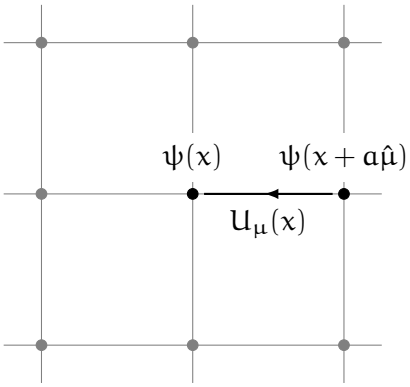

Figure 1: Graphical representation of the lattice Λ in two dimensions

The discretization is performed by introducing a hypercubic lattice Λ analogous to equation (2.5):

$$\Lambda = \left\{ x \in \mathbb{R}^4 \,|\, x_0/a = 1, \ldots, T \,;\, x_i/a = 1, \ldots, L \,;\, i = 1, \ldots, 3 \right\}. \tag{2.13}$$

The fields $\psi(x)$ and $\bar{\psi}(x)$ are associated with the lattice points, whereas the links variables U_μ are representations of the parallel transporters. Figure 1 shows a graphical representation of those quantities in two dimensions.

The dual lattice

$$\Lambda^* = \left\{ p \in \mathbb{R}^4 \,|\, p_0 = \frac{2\pi}{T} n_0 \,;\, p_i = \frac{2\pi}{L} n_i \right\}, \tag{2.14}$$

can be obtained by a Fourier transformation into momentum space. The integer n_0 is in a range of $-T/2, -T/2+1, \ldots, T/2$ and n_i respectively $-L/2, -L/2+1, \ldots, L/2$. Consequently the momentum p_μ is quantized as well and limited to the first Brillouin zone:

$$-\frac{\pi}{a} \leqslant p_\mu \leqslant \frac{\pi}{a}. \tag{2.15}$$

A parallel transporter moves a field from one point y in spacetime to another point x. Along its way the field absorbs a non-Abelian phase due to the gauge fields. Formally the transporter is given by:

$$U(x, y) = \text{P.O.} \exp\left(-\int_y^x dz\, A_\mu(z) \right). \tag{2.16}$$

The path-ordering "P.O." in equation (2.16) takes into account that QCD is an non-Abelian gauge theory. The parallel transporter $U(x, y)$ itself is an element of the gauge group $SU(3)$, whereas the gauge potential A_μ is an element of the corresponding $su(3)$ algebra. On the lattice the parallel transporter connects the fermion fields of two neighbouring lattice sites. This leads to the following definition of $U_\mu(x)$:

$$U_\mu(x) := U(x, x + a\hat{\mu}), \quad U_\mu(x)^{-1} = U(x + a\hat{\mu}, x) = U(x, x + a\hat{\mu})^{-1}. \tag{2.17}$$

The parallel transporter should transform in a way that the transformation law

$$U_\mu(x) \to g(x) U_\mu(x) g(x + a\hat{\mu})^{-1}, \quad g(x), g(x + a\hat{\mu})^{-1} \in SU(3) \tag{2.18}$$

persists in order to construct a gauge invariant lattice formulation of QCD. The transformation law for the fields is given by:

$$\psi(x) \to g(x)\psi(x), \quad \bar{\psi}(x) \to \bar{\psi}(x) g(x)^{-1}. \tag{2.19}$$

Additionally the plaquette

$$P_{\mu\nu} = U_\mu(x) U_\nu(x + a\hat{\mu}) U_\mu(x + a\hat{\mu})^{-1} U_\nu(x)^{-1} \tag{2.20}$$

is defined as the smallest closed loop on the lattice. Figure 2 shows a graphical representation of the plaquette in two dimensions. The plaquette is needed to construct the *Wilson plaquette action*

$$S_G = \beta \sum_{x \in \Lambda} \sum_{\mu < \nu} \left(1 - \frac{1}{3} \mathrm{Re}\,\mathrm{Tr}\, P_{\mu\nu}(x) \right) \tag{2.21}$$

serving as a discretization of the Yang-Mills action. The gauge coupling g_0 is included via the parameter $\beta = 6/g_0^2$

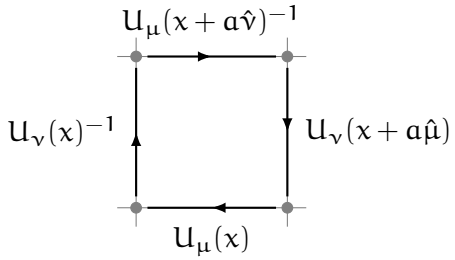

Figure 2: Graphical representation of the plaquette $P_{\mu\nu}$ in two dimensions

Using the parallel transporter U_μ, two discrete versions of the derivative can be formulated, the forward derivative ∇_μ and the backward derivative ∇_μ^*:

$$\nabla_\mu \psi(x) = \frac{1}{a} \left(U_\mu(x) \psi(x + a\hat{\mu}) - \psi(x) \right), \tag{2.22}$$

$$\nabla_\mu^* \psi(x) = \frac{1}{a} \left(\psi(x) - U_\mu(x - a\hat{\mu})^{-1} \psi(x - a\hat{\mu}) \right). \tag{2.23}$$

Ideally a discretized Dirac operator D and its Fourier transformed $\tilde{D}$ should satisfy the following statements:

a) D is local.
Locality is demanded for any quantum field theories describing elementary particles.

b) $\tilde{D}(p) = i\gamma_\mu p_\mu + \mathcal{O}(ap^2)$.
This statement ensures that the correct continuum limit of QCD is obtained.

c) $\tilde{D}(p)$ is invertible for $p \neq 0$.
This property guarantees the correct fermion spectrum. The mass of a fermion can be evaluated at a pole of the inverse Dirac operator.

d) $\gamma_5 D + D\gamma_5 = 0$.
If this equation is fulfilled, the massless theory has a chiral symmetry.

The *No-Go-Theorem* [7] by Nielsen and Ninomiya showed that the discretization requirements of the lattice actions mentioned above cannot be fulfilled simultaneously. So any lattice action will violate at least one of the conditions (a) - (d).

The naïve discretization of the Dirac operator

$$D_{\text{naïve}} = \frac{1}{2}\gamma_\mu \left(\nabla_\mu + \nabla_\mu^*\right) \tag{2.24}$$

turns out to violate condition c). This operator automatically incorporates instead of one 16 fermions, known as the fermion doubling problem. The Fourier transformed Dirac operator

$$\tilde{D}_{\text{naïve}} = i\gamma_\mu \frac{1}{a}\sin(ap_\mu) \tag{2.25}$$

vanishes for $p = 0$ as well as for $p = \frac{\pi}{a}$, so there are 2 poles to the Dirac operator in every dimension, in total $2^4 = 16$ poles of the Dirac operator, corresponding to 16 fermions on the lattice. The freedom to add operators to the action which vanish in the limit $a \to 0$, allows one to obtain a solution for this problem. Historically, Wilson [8] was the first who solved the fermion doubling problem by adding an two derivative term to the naïve Dirac operator. The price to pay is the loss of chiral symmetry in this discretization. The next section will focus on this discretization in a more detailed way.

2.4 WILSON FERMIONS

The massless Wilson Dirac operator

$$D_W = \frac{1}{2}\gamma_\mu \left(\nabla_\mu + \nabla_\mu^*\right) + ar\nabla_\mu^*\nabla_\mu \tag{2.26}$$

includes an additional contribution with a free coefficient r, the additional term vanishes in the limit $a \to 0$. The Fourier transform of equation (2.26) then solves the fermion doubling problem, but breaks chiral symmetry explicitly. As can be seen by the last term, the discretization effects in Wilson fermions are of order a, whereas the naïve discretization errors would be of order a^2. This issue can be solved by the *$\mathcal{O}(a)$ improvement program* introduced by Symanzik [9, 10]. Sheikholeslami and Wohlert [11] have shown that $\mathcal{O}(a)$ improvement can be achieved by adding a suitable counter term to the Dirac operator, which vanishes in the limit $a \to 0$. This counter term requires an appropriate tuning of a coefficient c_{SW} for each lattice spacing a. For the massless theory the Dirac operator

$$D_{SW} = D_W + \frac{ia}{4}c_{SW}\sigma_{\mu\nu}\hat{F}_{\mu\nu} \tag{2.27}$$

is constructed using a combination of gamma matrices $\sigma_{\mu\nu} = \frac{i}{2}[\gamma_\mu, \gamma_\nu]$ and the definition of the field strength tensor on the lattice

$$\hat{F}_{\mu\nu} = \frac{1}{8a^2}\left(Q_{\mu\nu}(x) - Q_{\nu\mu}(x)\right). \tag{2.28}$$

The quantity $Q_{\mu\nu}$ in equation (2.28) is the sum over all 4 plaquettes around one lattice point. It is called clover-leaf because of the shape of its graphical representation illustrated in figure 3.

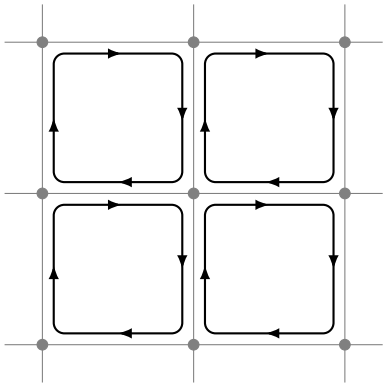

Figure 3: Graphical representation of the clover-leaf $Q_{\mu\nu}$ in two dimensions

The parameters of QCD, the bare coupling g_0 and the masses of the quarks, are redefined in lattice calculations by introducing new parameters β and the hopping parameter κ in the following way:

$$\beta = \frac{6}{g_0^2}, \tag{2.29}$$

$$\kappa = \frac{1}{2am_0 + 8r}. \tag{2.30}$$

With these definitions the fermionic part of the action for the Wilson fermions can be written as:

$$\begin{aligned} S_{WF} &= a^4 \sum_{x\in\Lambda} \bar{\psi}(x)\,(D_W + m_0)\,\psi(x) \\ &= a^4 \sum_{x\in\Lambda} \Bigg(-\frac{\kappa}{a} \sum_{\mu=0}^{3} \Big[\bar{\psi}(x)(r-\gamma_\mu)U_\mu(x)\psi(x+a\hat{\mu}) \\ &\qquad + \bar{\psi}(x+a\hat{\mu})(r+\gamma_\mu)U_\mu(x)^{-1}\psi(x) \Big] + \bar{\psi}(x)\psi(x) \Bigg). \end{aligned} \tag{2.31}$$

As a consequence of the introduction of the Wilson term, the point where the quarks mass vanishes is in an interacting theory a priori unknown and has to be determined. The point denoted by κ_c, can be evaluated for instance by obtaining the point where the pion mass vanishes. The bare quark mass and the hopping parameter are then related by:

$$m = \frac{1}{2a}\left(\frac{1}{\kappa} - \frac{1}{\kappa_c}\right). \tag{2.32}$$

Table 1 shows different actions, which are commonly used in Lattice QCD[3], together with their properties.

3 More details on these different actions can be found in [2, 12, 13, 14, 15, 16, 17].

action	discr. errors	chiral symmetry	doublers
naïve (2.24)	$\mathcal{O}(a^2)$	preserved	16
Wilson (2.26)	$\mathcal{O}(a)$	broken	none
Wilson + SW (2.27)	$\mathcal{O}(a^2)$	broken	none
Staggered [12]	$\mathcal{O}(a^2)$	subgroup unbroken	4
Neuberger [13, 14]	$\mathcal{O}(a^2)$	preserved	none
Domain Wall [15]	$\mathcal{O}(a^2)$	broken, exp. suppressed	none
Twisted Mass [16]	$\mathcal{O}(a^2)$	broken	none

Table 1: Different discretizations and its properties

2.5 PARTIALLY TWISTED BOUNDARY CONDITION

Due to the finite amount of memory on a computer, the simulation volume has to be finite, and usually one imposes periodic boundary conditions to the resulting box:

$$\psi(x + L) = \psi(x). \tag{2.33}$$

The simulation box is aligned to copies of itself. This can be geometrically interpreted as torus and so boundary effects are minimized. Anyway the effects of a finite volume have to be studied in every simulation to ensure that the simulation is reasonably close to the limit of infinite volume. Sachrajda and Villadoro [18] have proposed to use twisted boundary conditions in lattice simulations:

$$\psi(x_i + L) = U_i \psi(x_i). \tag{2.34}$$

With the generators T^a of the Cartan sub-algebra of the flavor group, the twisted boundary condition for a simulation can be written in the following way:

$$\psi(x_i + L) = U_i \psi(x_i) = \exp(i\theta_i^a T^a)\psi(x_i) = \exp(i\Theta_i)\psi(x_i). \tag{2.35}$$

The quark fields ψ can be redefined according to

$$\psi(x) = \exp\left(i\frac{\Theta_i}{L}x_i\right)\tilde{\psi}(x) \tag{2.36}$$

such that periodic boundary conditions are automatically fulfilled by the new fields $\tilde{\psi}(x)$. This procedure changes the Dirac operator in a way, in which the momentum is tuned by the twist angle Θ_i. Since the twist angle is a continuous variable, the momentum is now not longer discrete and can obtain any continuous value in the range of $[0, 2\pi]$ according to:

$$p_i = \frac{2\pi n_i}{L} + \frac{\Theta_i}{L}. \tag{2.37}$$

Sachrajda and Villadoro [18] have shown that for hadronic processes which do not involve final state interactions, twisted boundary conditions can be applied to the valence quarks only. The sea quarks then remain with periodic boundary conditions, which avoids the need to generate a new set of gauge configurations. Using this procedure, called partially twisted boundary condition, may introduce finite volume effects; Jüttner, Sachrajda and Flynn [19] have demonstrated that these are suppressed.

2.6 NUMERICAL SIMULATIONS

The expectation value of any operator A, which can be expressed in powers of the quark fields ψ, the antiquark fields $\bar{\psi}$ and the link-variables U_μ, can be evaluated using the functional integral. The expectation value $\langle A \rangle$ can be written as an Euclidean functional integral as

$$\langle A \rangle = \frac{1}{Z} \int D[U] D[\psi, \bar{\psi}] A e^{-S_G[U]} e^{-S_F[U,\psi,\bar{\psi}]}, \tag{2.38}$$

where S_G is the gluonic part of the action and S_F the fermionic part of the action. The integration involves an integration over all degrees of freedom in the fields ψ and $\bar{\psi}$ as well as over the gauge group $SU(3)$. The normalizing constant Z can be obtained by the condition $1 = \langle \mathbb{1} \rangle$. The fermionic part of the action is bilinear in the quark fields and the anti-quark fields, so this part of the integral can be performed analytically by Grassmann integration

$$\langle A \rangle = \frac{1}{Z} \int \prod_{x \in \Lambda} \prod_{\mu=0}^{3} dU_\mu(x) \tilde{A} \left(\det D_{\text{lat}}\right)^{N_f} e^{-S_G[U]}, \tag{2.39}$$

where $\tilde{A}$ denotes the operator with the fermionic degrees of freedom integrated out and $D_{\text{lat}} = D_W + m_0$ is the Dirac operator on the lattice. The measure $dU_\mu(x)$ is the group invariant Haar measure of the $SU(3)$ gauge group and N_f corresponds to the number of degenerate quark flavors. This equation can be generalized to non-degenerate quark flavors, but this work explicitly considers two degenerate flavors. The expectation value $\langle A \rangle$ is a high dimensional integral and a *Monte Carlo* integration scheme is applied in order to evaluate this integral.

The first step is to generate a set of gauge configurations. A configuration is a collection of all link variables on the lattice:

$$\{U_\mu(x) \,|\, x \in \Lambda\,,\ \mu = 0, \ldots 3\}. \tag{2.40}$$

An ensemble is an infinite set of configurations. For each configuration the statistical weight is given by:

$$W = \left(\det D_{\text{lat}}\right)^{N_f} e^{-S_G[U]}. \tag{2.41}$$

The weight is exponentially suppressed, so it is possible to consider only configurations for which the weight is large. This procedure is called *importance sampling*.

Configurations are constructed by generating a *Markov chain* of configurations $(\{U_\mu(x)\}_i \to \{U_\mu(x)\}_{i+1})$. Each one has to be accepted or rejected by a *Metropolis accept-reject step* [20], ensuring that the configurations are distributed according to their statistical weight. In lattice QCD commonly a procedure known as *Hybrid Monte Carlo* [21] is applied to generate a Markov chain of configurations. At first random initial momenta from a Gaussian distribution are chosen. Then the fields are evolved by integrating the Hamiltonian equations of motions for a small time step numerically. Afterwards, a Metropolis accept-reject step is applied to determine whether the configuration is used or discarded.

With a given set of configurations constructed as described above, the expectation value $\langle A \rangle$ can be estimated by the arithmetic mean $\bar{A}$ of an observable A_i over the gauge configurations:

$$\bar{A} = \frac{1}{N_{cfg}} \sum_{i=1}^{N_{cfg}} A_i. \tag{2.42}$$

In the limit $N_{cfg} \to \infty$ this estimate reproduces the expectation value exactly, but due to a finite amount of simulation time, this limit is out of reach. One therefore has to take the remaining statistical uncertainties into account. A more detailed discussion will follow in section 5.4.

2.7 PARTIALLY QUENCHED CALCULATION

In a pure Yang-Mills simulation of QCD, also called quenched simulation, the fermion determinant $\det D_{lat}$ is set to 1, corresponding to a simulation with no dynamical quarks, $N_f = 0$. Quenched simulations have been studied in the past, since the evaluation of the fermion determinant requires much computing power. The development of faster computers and more efficient algorithms allowed the use of dynamical quarks in last few years. This work considers lattice simulations with non-pertubatively $\mathcal{O}(a)$ improved Wilson fermions with two dynamical quarks ($N_f = 2$). In this case the masses for the quarks in terms of the hopping parameter κ are the same for sea and valence quarks $\kappa_{sea} = \kappa_v$.

The parameters of lattice simulations, the bare coupling and the quark masses, can be expressed by renormalized hadronic quantities like hadrons masses or decay constants. The mass of a generic pseudoscalar meson $am_{PS}(m_1, m_2)$ is a function of the free input parameters m_1, m_2, which corresponds to the mass of the quark m_1 and anti-quark m_2 in the pseudoscalar meson. Postulating exact isospin symmetry, the mass of the up and down quarks can be expressed by $\hat{m} = \frac{1}{2}(m_u + m_d)$. Assuming the lattice spacing a can be calibrated by some input quantity Q, the value for the light quark masses $\hat{m}$ is obtained when

$$\frac{m_{PS}(m_1, m_2)}{Q} = \left.\frac{m_\pi}{Q}\right|_{exp}, m_1 = m_2 \tag{2.43}$$

is matched to the experimental value m_π. Usually the masses are expressed in terms of the hopping parameter κ shown in equation (2.32).

It is possible to perform a partially quenched (PQ) simulation for instance for the strange quark by setting the hopping parameter for the valence quark κ_{val} to the hopping parameter of the strange quark κ_s. This simulation is performed with a sea of up and down quarks and a quenched valence strange quark. Partially quenched simulations require the knowledge of the hopping parameter for the strange quark κ_s which can be obtained by the data and procedure described in [22, 23]. Here, the ratio of the masses for a pseudoscalar and vector are determined for several calculations for some values of κ_2:

$$\left(\frac{m_{PS}(\hat{\kappa},\kappa_2)}{m_V(\hat{\kappa},\kappa_2)}\right)^2 = \left(\frac{m_K}{m_{K^*}}\right)^2\Big|_{exp} = 0.554^2 \tag{2.44}$$

Plotting these results against the inverse of κ_2 should show a straight line and the value for κ_s can be determined at the physical ratio $\left(\frac{m_K}{m_{K^*}}\right)^2 = 0.554^2$ which is for example shown for the D3[4] ensemble data in figure 4.

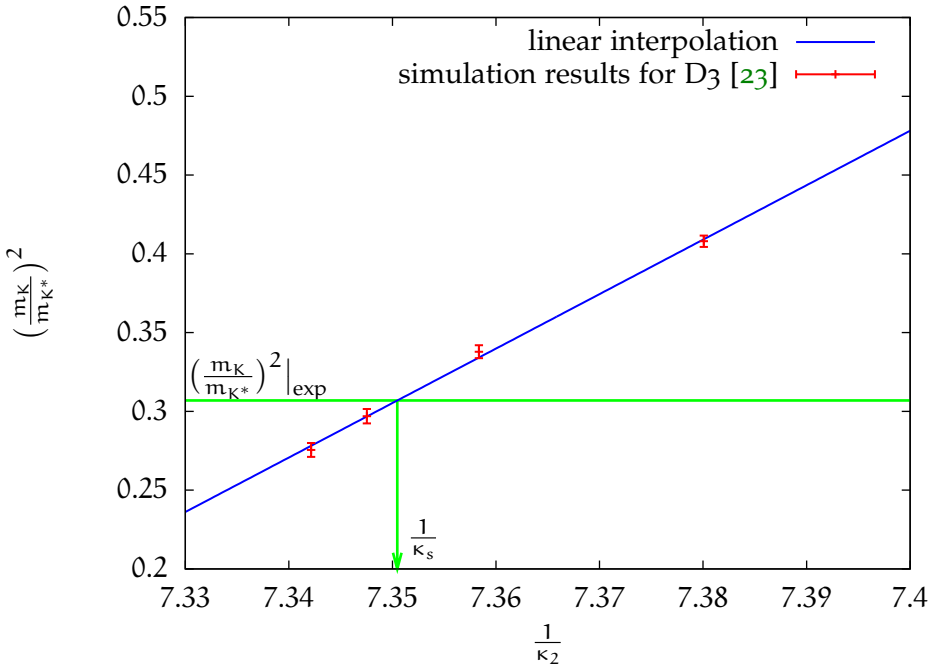

Figure 4: Determination of κ_s for D3 ensemble using data from [23]

4 This ensemble is used to illustrate the determination of κ_s. The corresponding parameters of this simulation are shown in table 2 in chapter 4.

3

ANOMALOUS MAGNETIC MOMENT OF THE MUON

The *Standard Model of Particle Physics* (SM) is highly successful in describing all known phenomena in strong, weak, and electromagnetic interactions. The *anomalous magnetic moment of the muon*

$$a_\mu \equiv \frac{g_\mu - 2}{2} \tag{3.1}$$

is one of the quantities in high energy physics that can be measured and calculated to very high precision and used to test the SM. Indeed, a discrepancy of 3.2 standard derivations occurs between measurements and theoretical predictions. This discrepancy might be a sign for new physics beyond the SM. The anomalous magnetic moment of the muon is more sensitive to unknown high energy effects than the electron, because of the relative mass scale $a_\mu/a_e \sim (m_\mu/m_e)^2$. This ratio could be improved by using the tau lepton instead of the muon, but due to the very short lifetime of the tau, the measurement is beyond current experimental possibilities. There are many efforts in order to improve the determination of the magnetic moment of the muon a_μ in experiments as well as in theoretical calculations. A detailed review on this topic can be found in [24] and the current data is available in a Particle Data Group review [25]. In the following sections the experimental determination as well as the theoretical predictions from different interactions are summarized.

3.1 EXPERIMENT

In principle the experimental determination [26, 24] of the anomalous magnetic moment of the muon a_μ is quite simple. The movement of a highly polarized muon in a storage ring in a constant magnetic field can be described by the *Larmor Precession*. A sketch of the experimental setup is shown in figure 5.

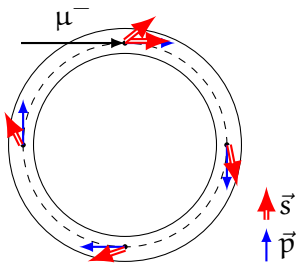

Figure 5: Systematic sketch of experimental setup showing the precessing muon and its spin in a storage ring

The muon performs a circular motion in the storage ring, where the spin of the muon is precessing along the momentum. The frequency difference ω_a between the angular frequency ω_c and the precession of the spin ω_s directly contains the anomalous magnetic moment of the muon a_μ:

$$\omega_a = \omega_s - \omega_c = \left(\frac{eB}{m_\mu \gamma} + a_\mu \frac{eB}{m_\mu}\right) - \frac{eB}{m_\mu \gamma} = a_\mu \frac{eB}{m_\mu}. \tag{3.2}$$

To measure the Larmor precession ω_a one exploits the fact that the decay of the muon ($\mu^- \to e^- \nu_\mu \bar{\nu}_e$) is spin polarized. The momentum of the emerging

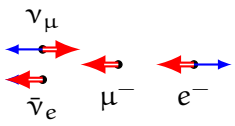

Figure 6: Decay pattern of the muon

electron is anti-parallel to the spin of the muon. Figure 6 shows the decay pattern. The weak interaction causing this decay couples only the left-handed leptons or right-handed anti-leptons. If the neutrinos are massless, the violation of the parity (P) prefers that left-handed electrons are emitted. Since the masses of the neutrinos have been shown to be small, this certainly is a good approximation. The polarized muon itself is produced by the decay of a boosted pion.

The E821 experiment in Brookhaven [26] has evaluated this quantity with a very high precision over a few years. The world average for the experimental value for the muon and anti-muon are:

$$a_{\mu^+}^{\text{exp}} = 11659204(6)(5) \cdot 10^{-10}, \tag{3.3}$$

$$a_{\mu^-}^{\text{exp}} = 11659215(8)(3) \cdot 10^{-10}, \tag{3.4}$$

$$\tag{3.5}$$

which show a good agreement. Lepton universality allows to combine these values to the mean:

$$a_\mu^{\text{exp}} = 11659208.9(5.4)(3.3) \cdot 10^{-10}. \tag{3.6}$$

3.2 THEORY PART I: ELECTROMAGNETIC CONTRIBUTION

Quantum Electro Dynamics (QED) is the quantum field theory describing the electromagnetic interaction. For QED it is possible to apply perturbation theory, because the bare coupling has a value of smaller than one $\alpha^{-1} = 137.035999084(51)$ [25]. Since experiments show a precision up to ppm, QED contributions need to be estimated up to fifth order.

The leading order QED contribution $a_\mu^{(1)}$ is given by the Feynman diagram in figure 7. This diagram describes the biggest contribution to the anomalous magnetic moment of the muon.

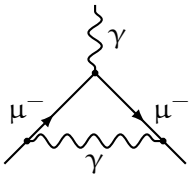

Figure 7: Lowest order QED contribution

This graph can be evaluated analytically

$$a_\mu^{(1)} = \frac{\alpha}{2\pi} = 11614097.3289(43) \cdot 10^{-10}, \tag{3.7}$$

which was done by Schwinger [27] a long time ago. The error takes into account the uncertainty of input value α and the mass ratios of the different leptons. The number of Feynman diagrams for higher order perturbations increases exponentially. For the second order this leads to 9 diagrams, the third order involves 72 diagrams. Beyond three loops the diagram appearing in the perturbative expansion must be evaluated numerically. At four loops there are 891 diagrams. For the fifth order there are 9080 diagrams. Having computed this contribution through 4-loops and estimated the fifth order contribution, the summarized result and the corresponding estimated errors [25] are:

$$\begin{aligned} a_\mu^{QED} = \frac{\alpha}{2\pi} + 0.765857410(27)\left(\frac{\alpha}{2\pi}\right)^2 + 24.05050964(43)\left(\frac{\alpha}{2\pi}\right)^3 \\ + 130.8055(80)\left(\frac{\alpha}{2\pi}\right)^4 + 663(20)\left(\frac{\alpha}{2\pi}\right)^5 + \dots \end{aligned} \tag{3.8}$$

The contributions of the electromagnetic interactions up to fifth order sum up to:

$$a_\mu^{QED} = 11658471.81(2) \cdot 10^{-10}. \tag{3.9}$$

The contribution from QED determines 99.994% of the theoretical prediction of a_μ, so the weak and strong interaction add small corrections to a_μ which will be discussed in the following sections.

3.3 THEORY PART II: WEAK CONTRIBUTION

The weak interaction is mediated by massive $W^\pm$ and Z bosons. These bosons couple to left-handed fermions and right-handed anti-fermions. The weak interactions allow to change the flavor of a quark and are responsible for the well known beta decay. Only the weak interactions violate P (parity) and CP (C:charge conjugation) whereas all other interactions conserve them. The masses of the bosons are about $\sim 100\ \mathrm{GeV}/c^2$, the interaction is weak compared to the electromagnetic interaction at a low energy scale. The leading order Feynman diagrams are shown in figure 8.

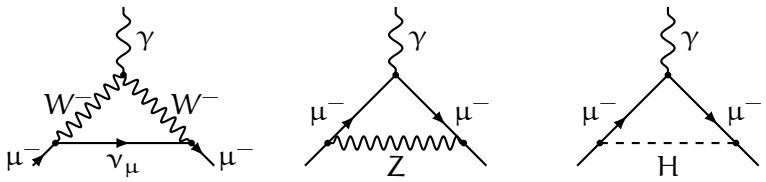

Figure 8: Lowest order weak contribution and hypothetical Higgs boson contribution

The third diagram involves the yet unobserved Higgs boson whose mass and existence is subject of the current LHC experiments. Nevertheless a lower bound for the Higgs mass enables an estimate for the contribution of the Higgs boson[25]

$$a_\mu(H) < 5 \cdot 10^{-14}, \tag{3.10}$$

which is actually completely negligible. The other diagrams as well as higher order contribution up to 2-loops can be evaluated and it turns out that the leading 3-loop logarithms are negligible and of $\mathcal{O}(10^{-12})$. The resulting contributions [25] at one and two loop order are given by:

$$a_\mu^{weak}[1-\text{loop}] = 19.482(2) \cdot 10^{-10}, \tag{3.11}$$

$$a_\mu^{weak}[2-\text{loop}] = -4.07(10)(18) \cdot 10^{-10}. \tag{3.12}$$

As expected, the resulting summed contribution of the weak interaction [25] is small but not negligible:

$$a_\mu^{weak} = 15.4(1)(2) \cdot 10^{-10}. \tag{3.13}$$

3.4 THEORY PART III: STRONG CONTRIBUTION

As already discussed , the strong interactions are described by QCD. These interactions show different behavior in a high and low energy regime. At a high energy scale, the theory becomes asymptotically free, an expansion in terms of the strong coupling α_s is possible. At a low energy scale the coupling grows to the order of 1, so that a perturbative treatment makes no sense.

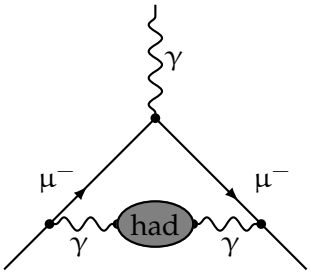

Figure 9: Lowest order hadronic contribution

In order to extract the hadronic contribution to the anomalous magnetic moment other techniques than perturbation theory have to be applied. Commonly, dispersion relation and the optical theorem are used to estimate the leading

order hadronic contribution shown in figure 9. The dispersion relation can be derived from causality for the vacuum polarization amplitude Π, which leads to:

$$\Pi(k^2) - \Pi(0) = \frac{k^2}{\pi} \int_0^\infty ds \frac{\operatorname{Im}\Pi(s)}{s\,(s - k^2 - i\epsilon)}, \tag{3.14}$$

in which $\sqrt{s}$ is the center of mass energy and k the momentum transfer. The optical theorem connects the imaginary part of the vacuum polarization amplitude to the total cross section from e^+e^- annihilation into hadrons. The optical theorem is a consequence of unitarity which can be expressed as below:

$$R(s) = \frac{3s}{4\pi\alpha_s(s)^2}\sigma_{tot}(e^+e^- \to \text{hadrons}), \tag{3.15}$$

$$\operatorname{Im}\Pi(s) = \frac{s}{4\pi\alpha_s(s)}\sigma_{tot}(e^+e^- \to \text{hadrons}) = \frac{\alpha_s(s)}{3}R(s). \tag{3.16}$$

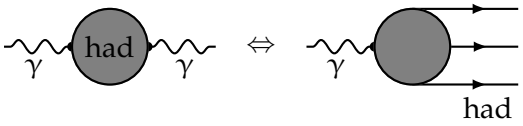

Figure 10: Optical theorem: Connecting vacuum polarization to hadronic total cross section

In a high energy regime QCD can be expanded perturbatively, so the calculation can be cut at an energy scale E_{cut} in which perturbation theory of QCD is known to work ($E_{cut} \gtrsim 2\,\text{GeV}$). The low energy part has to be evaluated using the experimental data for the cross section introducing experimental uncertainties to hadronic contribution. The resulting integral is a convolution of the ratio $R(s)$ and an analytical known function $\tilde{K}(s)$:

$$a_\mu^{had} = \left(\frac{\alpha_s m_\mu}{3\pi}\right)^2 \left(\int_{m_\pi^2}^{E_{cut}^2} ds \frac{R_{data}(s)\tilde{K}(s)}{s^2} + \int_{E_{cut}^2}^\infty ds \frac{R_{per}(s)\tilde{K}(s)}{s^2} \right), \tag{3.17}$$

$$\tilde{K}(s) = \frac{3s}{m_\mu^2}\left(\frac{s^2}{2}(2 - s^2) + \frac{(1+s^2)(1+s^2)}{s^2}\left(\ln(1+s) - s + \frac{s^2}{2}\right) + \frac{(1+s)}{(1-s)}s^2\ln(s)\right). \tag{3.18}$$

Using all available $e^+e^- \to$ hadrons data the leading hadronic contribution to the anomalous magnetic moment [25] is

$$a_\mu^{had} = 695.5(4.0)(0.7) \cdot 10^{-10}. \tag{3.19}$$

The error of the leading order hadronic contribution limits the theoretical prediction. An improvement of this contribution is needed in order to improve the

error bars of the theoretical calculations.The first error addresses the experimental uncertainties, whereas the second error involves uncertainties of perturbation QCD.

Another approach involves the vector spectral functions from the tau decay ($\tau \to \nu_\tau + \text{hadrons}$). This decay can be connected to the $e^+e^- \to \text{hadrons}$ cross section by an isospin rotation. Including isospin violation corrections to the tau decay data, the hadronic contribution [25] changes a_μ^{had} to :

$$a_\mu^{had,\tau} = 705.3(4.0)(1.9)(0.7) \cdot 10^{-10}. \tag{3.20}$$

The leading order hadronic contribution to a_μ shows a discrepancy between the approaches using e^+e^- data or τ decay data. The difference exceeds the estimated uncertainties. The τ decay approach could underestimate isospin-breaking effects, but shows a better agreement with the experimental measured a_μ. The e^+e^- data can be directly related via the dispersion integral and is a theoretical cleaner estimate.

Higher order $\mathcal{O}(\alpha^3)$ contribution, including an additional photon line in figure 9, can be evaluated using the same e^+e^- data from experiments [25]:

$$a_\mu^{had,\alpha^3} = -9.8(0.1) \cdot 10^{-10}. \tag{3.21}$$

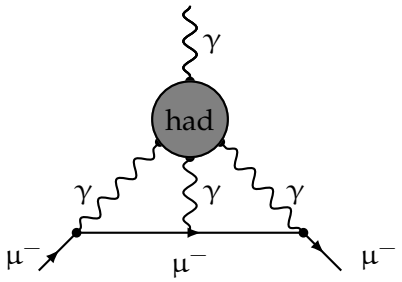

Figure 11: Light-by-light scattering contribution

The light-by-light scattering contribution (lbl), which can be seen in figure 11, enters at an $\mathcal{O}(\alpha^3)$ level. This can be evaluated by a model-independent approach using large N_C QCD [25] to:

$$a_\mu^{lbl} = 10.5(2.6) \cdot 10^{-10}. \tag{3.22}$$

3.5 COMPARISON BETWEEN EXPERIMENT AND THEORY

Summing up all contributions of different SM interactions leads to a theoretical prediction for the anomalous magnetic moment of the muon:

$$a_\mu^{theo} = 11659183.4(0.2)(4.1)(2.6) \cdot 10^{-10}, \tag{3.23}$$

$$a_\mu^{exp} = 11659208.9(5.4)(3.3) \cdot 10^{-10}, \tag{3.24}$$

$$\Delta a_\mu = a_\mu^{exp} - a_\mu^{theo} = 25.5(6.3)(4.9) \cdot 10^{-10}. \tag{3.25}$$

The theoretical prediction can be compared to the result of the experimental determination and a significant deviation of 3.2 σ between theory and experiment is observed. If the τ data is included in the determination of the hadronic vacuum polarization, the deviation is reduced to 1.9 σ.

The combined uncertainties from experiments are larger than the combined theoretical error, where the strong interaction, especially the hadronic vacuum polarization, is dominant in the theoretical uncertainty. Currently the limitations for the magnetic moment of the muon are given by the experimental determination and there are newly proposed experiments at Fermilab [28] and JPARC [29], which could improve the precision of the experiment by a factor of 4. Reducing both theoretical and experimental errors is going to show whether the 3.2 σ deviation remains. If it remains or even increases, the anomalous magnetic moment of the muon would be one of the first signals for physics beyond the SM. If not, it would prove the validity of the SM with a very high precision.

Part II

LATTICE DETERMINATION OF THE HADRONIC VACUUM POLARIZATION

4

CONSTRUCTING THE VACUUM POLARIZATION

In this chapter I will focus on a non-perturbative method to construct the leading hadronic contribution as shown in figure 12 to a_μ[1] using lattice gauge theory techniques.

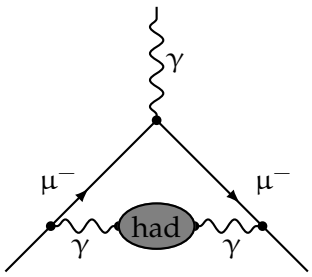

Figure 12: Lowest order hadronic contribution

In this case no other inputs than the physical parameters of QCD are needed, so it can be considered to be a purely theoretical prediction. In contrast to the dispersive approach discussed in section 3.4, the simulations using lattice QCD do not require an experimental input, beyond that which is required to fix the physical values of the QCD parameters.

There have been already attempts to calculate a_μ using different lattice actions. In the past, groups used the quenched approximation with $\mathcal{O}(a)$ improved Wilson fermions as valence quarks in [31] and domain wall fermions in [32]. In addition, there have been simulations with 2+1 dynamical quarks using staggered fermions in [33] and 2 flavor twisted mass fermions in [34]. In the literature there is an ongoing debate on the rooting problem of staggered fermions [35] using a fourth root trick to get rid of the fermion doubling problem. In order to understand systematic effects by different discretizations here a different approach is used to study a_μ.

The lattice QCD simulations of this work are done using non-perturbatively $\mathcal{O}(a)$ improved Wilson fermions with two degenerate, dynamical quarks. In addition partially twisted boundary conditions, discussed in section 2.5 and 4.4, are applied to the computation of the vacuum polarization to achieve an improvement of the momentum resolution.

1 In the following the hadronic contribution to the anomalous magnetic moment of the muon is abbreviated by $a_\mu \equiv a_\mu^{had}$.

4.1 LATTICE SETUP

The vacuum polarization amplitude $\Pi(q^2)$ is related to the current-current correlator via:

$$\Pi_{\mu\nu}(q) = i \int d^4x e^{iqx} \left\langle J^{em}_\mu(x) J^{em}_\nu(0) \right\rangle = \left(q_\mu q_\nu - q^2 g_{\mu\nu}\right) \Pi(q^2). \tag{4.1}$$

The charges for the different quark flavors z_f can be separated by redefining the electromagnetic vector currents $J^{em}_\mu(x) = \sum_f z_f J^f_\mu(x)$. The correlator needed for equation (4.1) can be split up into two separate parts shown in figure 13, a connected part and a disconnected part.

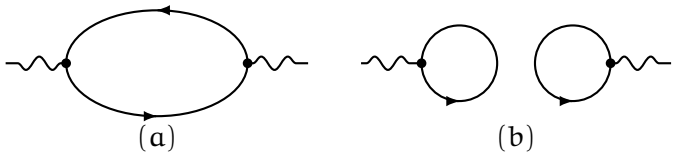

Figure 13: Two possible Wick contractions for the vacuum polarization: (a) connected diagram, (b) disconnected diagram

Imposing isospin symmetry for up and down quark, the new vector current $J_\mu(x) \equiv J^u_\mu(x) = J^d_\mu(x)$ is the same for both quark types and therefore the vacuum polarization as well. In the following the connected diagram of figure 13 (a) is studied using lattice simulations. The disconnected diagram as shown in figure 13 (b) is more difficult to evaluate in lattice simulations, since it requires propagators from all lattice points to all others. This disconnected diagram is not the subject of this work and has been estimated by Jüttner and Della Morte [36] using two flavor chiral perturbation theory to reduce the connected diagram by 10%.

As mentioned before Wilson fermions break chiral symmetry explicitly. This has the consequence that the vector current $\bar\psi\gamma_\mu\psi$ is not conserved. It can be renormalized in order to fulfill $\partial_\mu J^{ren}_\mu = 0$, but this requires a renormalizing factor, which has to be determined independently. Here instead the point-split vector current is used, which is conserved and requires no renormalizing constant. The Noether theorem connects symmetries to conserved quantities. Since the lattice action is invariant under gauge transformations, the Noether theorem implies a conserved current connected to that symmetry. Following [37] this current can be obtained by an infinitesimal, unitary, local transformation

$$\begin{aligned} \bar\psi' &= \bar\psi\left(1 - i\epsilon(x)\right), \\ \psi' &= \psi\left(1 + i\epsilon(x)\right) \end{aligned} \tag{4.2}$$

up to second order in the infinitesimal parameter $\epsilon(x)$ on the Wilson fermion action S_{WF}. The lattice action S_{WF} shown in equation (2.31) and as a result the partition function Z should be invariant under the transformations in equation (4.2). For simplicity we consider expectations values with respect to fermionic degrees

of freedom only. Gauge invariance ensures that the partition function is given by:

$$Z = \int D[\psi,\bar{\psi}]e^{-S}\left(1 - i\sum_{x\in\Lambda}\left(\frac{\partial S}{\partial\psi(x)}\epsilon(x)\psi(x) - \bar{\psi}(x)\epsilon(x)\frac{\partial S}{\partial\bar{\psi}(x)}\right)\right). \quad (4.3)$$

So all additional terms in $\epsilon(x)$ should vanish, implying

$$\langle\nabla_\mu J_\mu(x)\rangle_{\bar{\psi}\psi} = \left\langle\frac{\partial S}{\partial\psi(x)}\epsilon(x)\psi(x) - \bar{\psi}(x)\epsilon(x)\frac{\partial S}{\partial\bar{\psi}(x)}\right\rangle_{\bar{\psi}\psi} = 0, \quad (4.4)$$

from which the conserved vector current

$$J_\mu(x) = \frac{1}{2}\left(\bar{\psi}(x+a\hat{\mu})(r+\gamma_\mu)U^+_\mu(x)\psi(x) - \bar{\psi}(x)(r-\gamma_\mu)U_\mu(x)\psi(x+a\hat{\mu})\right) \quad (4.5)$$

can be extracted, setting $\epsilon(x)$ to δ_{xy}. The vector current J_μ is anti-Hermitian due to the properties of the γ-matrices:

$$J^\dagger_\mu(x) = -J_\mu(x). \quad (4.6)$$

In non-forward matrix elements, like the vacuum polarization amplitude, the point-split vector current is accurate up to $\mathcal{O}(a)$. In momentum space equation (4.4) transforms to:

$$\frac{2}{a}\sin\left(\frac{q_\mu a}{2}\right)\sum_n e^{iqna+iqa\hat{\mu}/2}\langle J_\mu(x)\rangle_{\bar{\psi}\psi} = 0 \quad (4.7)$$

Introducing the momentum variable:

$$\hat{q}_\mu = \frac{2}{a}\sin\left(\frac{q_\mu a}{2}\right) \quad (4.8)$$

on the lattice and the Fourier transformed vector current

$$\sum_n e^{iqna+iqa\hat{\mu}/2}\langle J_\mu(x)\rangle_{\bar{\psi}\psi} = \langle J_\mu(q)\rangle_{\bar{\psi}\psi}, \quad (4.9)$$

equation (4.7), the Ward-Takahashi identity [38, 39] for the vector current, can be written as:

$$\hat{q}_\mu\langle J_\mu(q)\rangle_{\bar{\psi}\psi} = 0 \quad (4.10)$$

To derive the vacuum polarization, the expectation value of an operator $\langle A\rangle_{\bar{\psi}\psi}$, which is a function of the fields $\psi,\bar{\psi}$ and U, is expanded using the transformations in equation (4.2). Since the vacuum polarization is the expectation value of two vector currents, the operator A is set to the vector current J_ν. Again one demands that all terms linear in $\epsilon(x)$ vanish, and setting $\epsilon(x)$ to δ_{xy} leads to:

$$\langle J_\nu(y)\nabla_\mu J_\mu(x)\rangle_{\bar{\psi}\psi} + \left\langle\frac{\partial J_\nu}{\partial\psi(x)}\psi(x) - \bar{\psi}(x)\frac{\partial J_\nu}{\partial\bar{\psi}(x)}\right\rangle_{\bar{\psi}\psi} = 0. \quad (4.11)$$

Using the definition

$$J_\mu^{(2)}(x) = \frac{a}{2}\left(\bar\psi(x+a\hat\mu)(r+\gamma_\mu)U_\mu^+(x)\psi(x) + \bar\psi(x)(r-\gamma_\mu)U_\mu(x)\psi(x+a\hat\mu)\right) \tag{4.12}$$

this can be condensed to:

$$\langle J_\mu(y)\nabla_\nu J_\nu(x)\rangle_{\bar\psi\psi} + \left\langle J^{(2)}(x)_\nu\right\rangle_{\bar\psi\psi}\delta_{xy}\delta_{\mu\nu} = 0. \tag{4.13}$$

A Fourier transformation of equation (4.13) allows one to obtain the vacuum polarization tensor

$$\Pi_{\mu\nu}(\hat q) = \Pi_{\mu\nu}^{(1)}(\hat q) + \Pi_{\mu\nu}^{(2)}(\hat q), \tag{4.14}$$

where

$$\Pi_{\mu\nu}^{(1)}(\hat q) = \frac{a^4}{T\cdot L^3}\sum_{x,y\in\Lambda} e^{i\hat q x - i\hat q y + i\hat q a\hat\mu/2 - i\hat q a\hat\nu 2}\left\langle J_\mu(y)J_\nu(x)\right\rangle, \tag{4.15}$$

$$\Pi_{\mu\nu}^{(2)}(\hat q) = -\frac{a^4}{T\cdot L^3}\sum_{x,y\in\Lambda} e^{i\hat q x - i\hat q y}\left\langle J_\mu^{(2)}(x)\right\rangle\delta_{xy}\delta_{\mu\nu}. \tag{4.16}$$

The coefficients in equations (4.15) and (4.16) are chosen to reproduce the correct continuum limit. The expectation values in equations (4.15) and (4.16) involve all degrees of freedom $\psi, \bar\psi$ and U. The first part $\Pi_{\mu\nu}^{(1)}(\hat q)$ of the vacuum polarization corresponds to the diagram (a) in figure 14, while the second part is illustrated in diagram (b), which vanishes in the continuum theory.

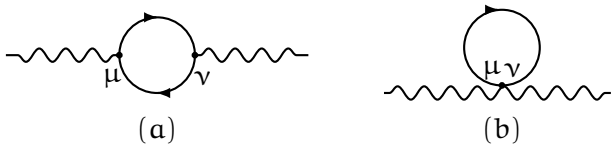

(a) (b)

Figure 14: Contribution to the vacuum polarization tensor: (a) corresponding to $\Pi_{\mu\nu}^{(1)}$, (b) depicting $\Pi_{\mu\nu}^{(2)}$

Translation invariance in the gauge average allows one to perform a variable substitution $\tilde x = x - y$, $\tilde y = y - y = 0$ reducing the number of inversions of the propagator from $T\cdot L^3$ to five. In the end the vacuum polarization can be written as:

$$\Pi_{\mu\nu}^{(1)}(\hat q) = a^4\sum_{\tilde x\in\Lambda} e^{i\hat q(\tilde x + a\hat\mu/2 - a\hat\nu/2)}\left\langle J_\mu(\tilde x)J_\nu(0)\right\rangle \tag{4.17}$$

$$\Pi_{\mu\nu}^{(2)}(\hat q) = -a^4\left\langle J_\mu^{(2)}(0)\right\rangle\delta_{\mu\nu} \tag{4.18}$$

With these definitions the Ward-Takahashi identities

$$\langle\hat q_\mu\Pi_{\mu\nu}(\hat q)\rangle = \langle\hat q_\nu\Pi_{\mu\nu}(\hat q)\rangle = 0 \tag{4.19}$$

are fulfilled. These identities are conserved in the gauge average, because of the use of translation invariance.

Using the γ_5-hermicity of the Wilson-Dirac operator, the two parts of the vacuum polarization tensor $\Pi_{\mu\nu}$ can be written in terms of the quark propagator

$$S(y,x) = \gamma_5 S^\dagger(x,y)\gamma_5, \tag{4.20}$$

and the gauge links $U_\mu(x)$:

$$\begin{aligned}\Pi^{(1)}_{\mu\nu}(\hat{q}) = \frac{a^4}{4}\sum_{x\in\Lambda} e^{i\hat{q}(x+a\hat{\mu}/2-a\hat{\nu}/2)}\,\mathrm{Tr}\big[&\\ &(r+\gamma_\nu)U^\dagger_\nu(0)\gamma_5 S^\dagger(x+a\hat{\mu},0)\gamma_5(r+\gamma_\mu)U^\dagger_\mu(x)S(x,a\hat{\nu})\\ -&(r-\gamma_\nu)U_\nu(0)\gamma_5 S^\dagger(x+a\hat{\mu},a\hat{\nu})\gamma_5(r+\gamma_\mu)U^\dagger_\mu(x)S(x,0)\\ -&(r+\gamma_\nu)U^\dagger_\nu(0)\gamma_5 S^\dagger(x,0)\gamma_5(r-\gamma_\mu)U_\mu(x)S(x+a\hat{\mu},a\hat{\nu})\\ +&(r-\gamma_\nu)U_\nu(0)\gamma_5 S^\dagger(x,a\hat{\nu})\gamma_5(r-\gamma_\mu)U_\mu(x)S(x+a\hat{\mu},0)\big],\end{aligned} \tag{4.21}$$

$$\Pi^{(2)}_{\mu\nu}(\hat{q}) = \frac{a}{2}\delta_{\mu\nu}\,\mathrm{Tr}\big[(1+\gamma_\nu)U^\dagger_\nu(0)S(0,a\hat{\nu}) + (1+\gamma_\nu)U_\nu(0)S^\dagger_\nu(0,a\hat{\nu})\big]. \tag{4.22}$$

The quark propagator $S(y,x)$ starting from a fixed point x can be obtained by a numerical inversion of the Wilson-Dirac operator using for instance the conjugate-gradient algorithm [40]. In order to measure the quantities in equation (4.21) on the lattice, one needs at least five inversions with sources located at $0, a\hat{e}_0, a\hat{e}_1, a\hat{e}_2$ and $a\hat{e}_3$.

Having computed the vacuum polarization tensor $\Pi_{\mu\nu}(q)$ on the lattice by equations (4.21) and (4.22), the vacuum polarization $\Pi(q^2)$ can be extracted as

$$\Pi(\hat{q}^2) = \sum_{\mu,\nu=0}^{3} \frac{\Pi_{\mu\nu}(\hat{q})}{\hat{q}_\mu\hat{q}_\nu - \delta_{\mu\nu}\hat{q}^2} \tag{4.23}$$

by contracting both indices μ and ν. In addition contributions with a denominator of zero are not measurable and left out. Before discussing the methods to determine the function $\Pi(q^2)$, simulation details and tests of the implementation are presented.

4.2 IMPLEMENTATION DETAILS AND TEST

The implementation uses Wilson fermions with two mass-degenerate quarks. The discretization errors have been improved by the Sheikholeslami-Wohlert term [11] to achieve an $\mathcal{O}(a^2)$ lattice formulation. The input parameter for the calculations are the inverse bare coupling $\beta = 5.3$ and the hopping parameter κ connected to the quark masses. $c_{sw} = 1.90952$ has been tuned appropriately according to [41] to ensure $\mathcal{O}(a)$ improvement of spectral quantities. The simulation code is based on the DD-HMC algorithm developed by Lüscher [42]. This

algorithm combines the ideas of domain decomposition and deflation[2] with the Hybrid Monte Carlo algorithm shown in 2.6. The calculation of the vacuum polarizations tensor is integrated into the measure code developed by us.

run	κ_{sea}	volume	L [fm]	N_{cfg}	m_π [MeV]	κ_s
D2	0.13590	$48 \cdot 24^3$	1.7	149	704.8(2.6)	0.13632
D3	0.13610	$48 \cdot 24^3$	1.7	168	552.5(3.4)	0.13605
D4	0.13620	$48 \cdot 24^3$	1.7	168	485.4(4.0)	0.13591
D5	0.13625	$48 \cdot 24^3$	1.7	169	429.3(4.3)	0.13574
E2	0.13590	$64 \cdot 32^3$	2.2	158	696.5(0.9)	0.13632
E3	0.13605	$64 \cdot 32^3$	2.2	156	593.4(1.1)	0.13609
E4	0.13610	$64 \cdot 32^3$	2.2	162	554.2(1.1)	0.13605
E5	0.13625	$64 \cdot 32^3$	2.2	168	414.4(1.4)	0.13574
F6	0.13635	$96 \cdot 48^3$	3.3	200	297.9(0.9)	0.13575

Table 2: Parameters for the different runs and results for m_π and κ_s

Table 2 shows the run parameters of the simulations as well as corresponding pion mass m_π and hopping parameter of the strange quarks κ_s, which is needed for the partially quenched simulation with $N_f = 2 + 1$. For all simulations a lattice spacing of $a = 0.0689$ [45] has been used. This value has been obtained by an appropriate rescaling of the lattice spacing for $\beta = 5.5$ ensembles using the hadronic radius. The scale for $\beta = 5.5$ ensembles has been determined using the mass of the Ω^- baryon. Nevertheless a scale determination for $\beta = 5.3$ is currently investigated by us. The pion masses for the E and F ensembles also have been determined in this study. The pion masses for the D ensembles are obtained from [22]. The values for κ_s have been evaluated as shown in section 2.7.

In order to identify implementation errors of the vacuum polarization tensor, several tests can be performed. The lattice formulation itself ensures gauge invariance, so a random gauge transformation $g(x), g(x + a\hat{\mu})^{-1}$ can be applied:

$$U_\mu(x) \to g(x) U_\mu(x) g(x + a\hat{\mu})^{-1}, \quad g(x), g(x + a\hat{\mu})^{-1} \in SU(3). \tag{4.24}$$

This transformation should leave the vacuum polarization tensor invariant up to numerical precision and the test shows that this is fulfilled.

An additional test is to check the imaginary part of the vacuum polarization tensor. The definition of the vacuum polarization tensor, equation (4.1), includes an expectation value of two vector currents. This expectation value should be

2 Details on the implementation of the DD-HMC and its acceleration techniques are shown in [43, 42, 44]

real, since the operators $J_\mu(x)J_\nu(0)$ and $J_\mu^{(2)}(x)$ are self-adjoined. Indeed the imaginary part vanishes up to numerical precision.

The Ward-Takahashi identities

$$\langle \hat{q}_\mu \Pi_{\mu\nu}(\hat{q}) \rangle = \langle \hat{q}_\nu \Pi_{\mu\nu}(\hat{q}) \rangle = 0 \tag{4.25}$$

also serve as a check. This identity is valid for all possible combinations of momentum and indices μ and ν. This relation has been checked for a few combinations of momentum and indices.

4.3 EXTRACTING a_μ

Having computed the vacuum polarization tensor $\Pi_{\mu\nu}(q)$ for different ensembles the next step is the calculation of the vacuum polarization $\Pi(q^2)$ via equation (4.23). Starting from the vacuum polarization $\Pi(q^2)$, it is in principle quite simple to write down the hadronic contribution to the anomalous magnetic moment of the muon a_μ by a convolution integral [32]:

$$a_\mu^{\text{had}} = \frac{\alpha^2}{3\pi^2} \sum_f z_f^2 \int_0^\infty \frac{dq^2}{q^2} \, 12\pi^2 \, F(q^2) \left(\Pi(0) - \Pi(q^2) \right). \tag{4.26}$$

The kernel

$$F(q^2) = \frac{\left(\frac{4m_\mu^2}{q^2} \right)^2}{\left(1 + \sqrt{1 + \frac{4m_\mu^2}{q^2}} \right)^4 \sqrt{1 + \frac{4m_\mu^2}{q^2}}} \tag{4.27}$$

depends on the mass of the muon m_μ and the momentum transfer q^2. This kernel is peaked below the mass of the muon $m_\mu = 105.658367(4)\,\text{MeV}^2/c^2$ [46] as shown in figure 15 and it suppresses large momentum contributions to the anomalous magnetic moment a_μ. Figure 15 shows a plot of the kernel $F(q^2)$ scaled logarithmically in the momentum q^2.

An example for the simulation results for the vacuum polarization $\Pi(q^2)$ for the E4 ensemble is shown in figure 16 plotted against the momentum transfer q^2. Since equation (4.26) needs the vacuum polarization at zero momentum transfer, the intercept $\Pi(0)$ is essential to determinate a_μ. The limiting factor for the accuracy of lattice estimates for a_μ is the ability to constrain the low-momentum region.

The basic idea is to fit the vacuum polarization amplitude to an analytic function and use this function to extract a_μ by integrating equation (4.26) numerically. These functions are expected not to contain singularities, so the numerical integration is straightforward.

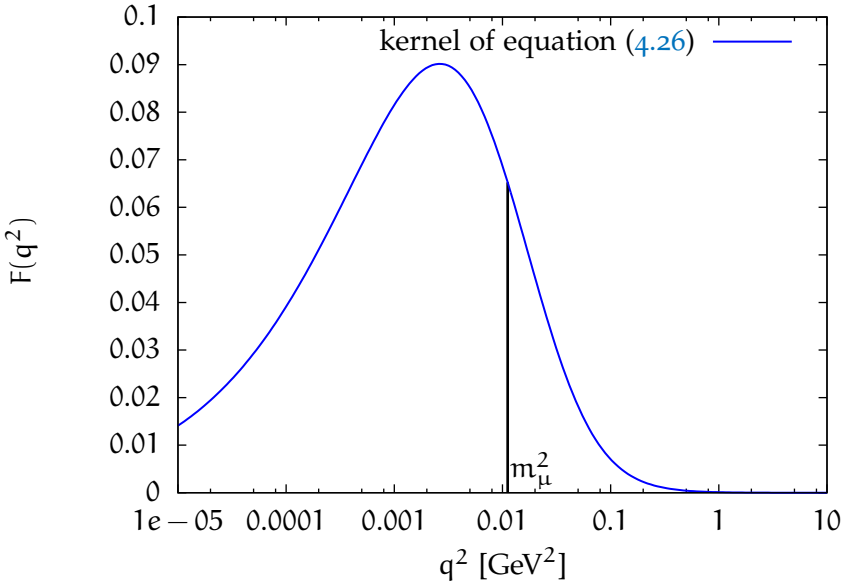

Figure 15: Plot of the kernel function $F(q^2)$ of the equation (4.26).

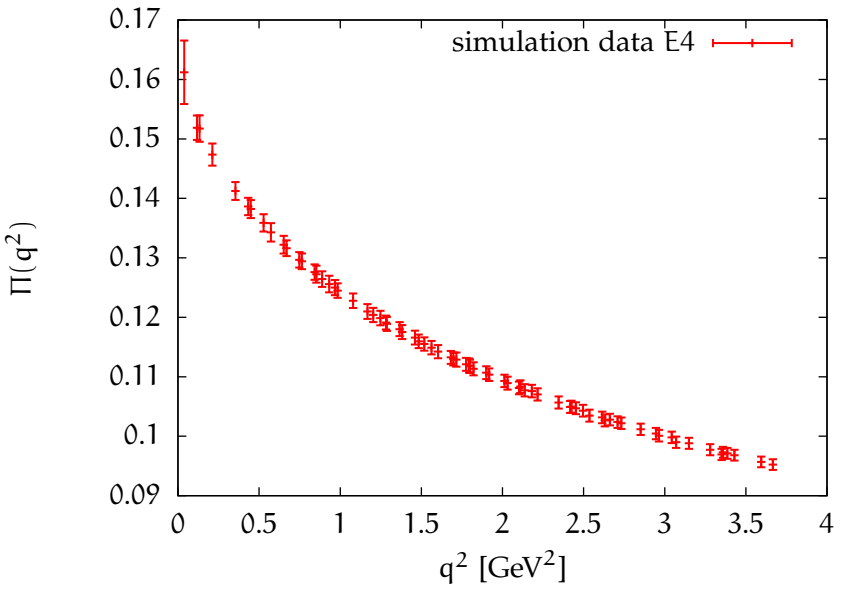

Figure 16: Simulation results for $\Pi(q^2)$ on the E4 ensemble with 162 configurations

For further discussions the quantity $\hat{\Pi}(q^2)$ is defined as:

$$\hat{\Pi}(q^2) = \Pi(0) - \Pi(q^2). \tag{4.28}$$

The charge factor

$$z = \sum_f z_f^2 \tag{4.29}$$

is measured in multiples of the elementary QED charge e and factorizes the charges of the quarks in equation (4.26).

4.4 APPLICATION OF PARTIALLY TWISTED BOUNDARY CONDITION

Partially twisted boundary condition (bc) is one of the major features of this diploma thesis, since it allows one to gain control over the momentum dependence of the vacuum polarization amplitude.

The twist of a quark and an anti-quark in flavor neutral hadron in the same way would lead to a net twisted momentum of $p_i = \frac{2\pi n_i}{L} + \frac{\Theta_i - \Theta_i}{L} = \frac{2\pi n_i}{L}$, thus a trick is used for the computations. The vacuum polarization tensor $\Pi_{\mu\nu}(q)$ is the correlation of two electromagnetic vector currents in equation (4.1). Lets assume for simplicity that the electromagnetic vector current is given by the local current:

$$J_\mu(x) = \bar{\psi}(x)\gamma_\mu\psi(x). \tag{4.30}$$

It is straightforward to apply these considerations to the general case in section 4.1. Using this definition of the vector current, the vacuum polarization tensor can be written as:

$$\Pi^{(1)}_{\mu\nu}(\hat{q}) = a^4 \sum_{x\in\Lambda} e^{i\hat{q}x} \left\langle J_\mu(x) J_\nu(0) \right\rangle . \tag{4.31}$$

The second part of the vacuum polarization tensor $\Pi^{(2)}_{\mu\nu}(\hat{q})$ involves the calculation of one propagator, so the twist cancels here anyway. So the contractions need the evaluation of the two propagators. A twist of those propagators in the same way leads to a vanishing net twisting angle as mentioned before. The electromagnetic current is per definition a flavor-diagonal quantity causing a net twist $\Theta_i = 0$. Imposing iso-spin symmetry in the two-flavor theory allows one to re-interpret the contribution

$$\begin{aligned}\Pi^{(1)}_{\mu\nu}(\hat{q}) &= a^4 \sum_{x\in\Lambda} e^{i\hat{q}x} \left\langle \mathrm{Tr}\, \bar{\psi}(x)\gamma_\mu\psi(x)\bar{\psi}(0)\gamma_\nu\psi(0) \right\rangle \\ &= a^4 \sum_{x\in\Lambda} e^{i\hat{q}x} \left\langle \mathrm{Tr}\, \bar{u}(x)\gamma_\mu d(x)\bar{d}(0)\gamma_\nu u(0) \right\rangle ,\end{aligned} \tag{4.32}$$

as a flavor-non-diagonal quantity, for which twisted bondary conditions have a non-trivial effect. The contractions now contain the evaluation of two different propagators, so for instance the up quark propagator can be twisted, where as the down quark propagator remains untwisted.

Going towards zero momentum the precision of the vacuum polarization $\Pi(q^2)$ decreases, since its denominator is the combination of the momenta squared and constant precission for the vacuum polarization is assumed. The application of partially twisted boundary condition can move data points closer to $q^2 = 0$, it also lifts the degeneracy of positive and negative momentum. All momenta are shifted by the transformation. It turns out that the signal obtained with a twist angle that shifts the lowest momentum by about 30% towards zero still

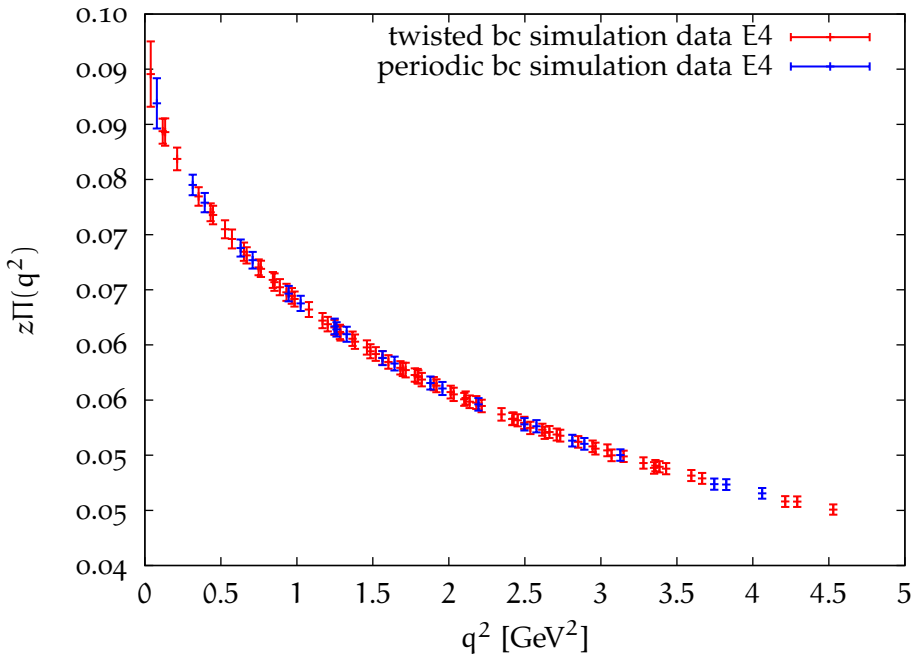

Figure 17: Effect of partial twisted boundary condition on E4 ensemble

has reasonable error bars. Also the degeneracy arranges the momenta in a way that former gaps are filled with data points.

Figure 17 shows the result of the application of partially twisted boundary conditions on the vacuum polarization for E4 ensemble. These additional points reveal more details of the curvature of the vacuum polarization. This may assist the fits which are needed for the extraction of a_μ. To what extent the additional points increase the accuracy and confidence of lattice results for a_μ^{had} will be analyses in section 6.2.

Having fitted a suitable function to the data, the complete integrand of equation (4.26) is shown in figure 18. Here the momentum is plotted on a logarithmic scale. The peak region of the integrand is not directly reachable with lattice techniques, but partially twisted boundary conditions help to reach lower momenta and give a better control on the systematic effects of the extrapolation in q^2.

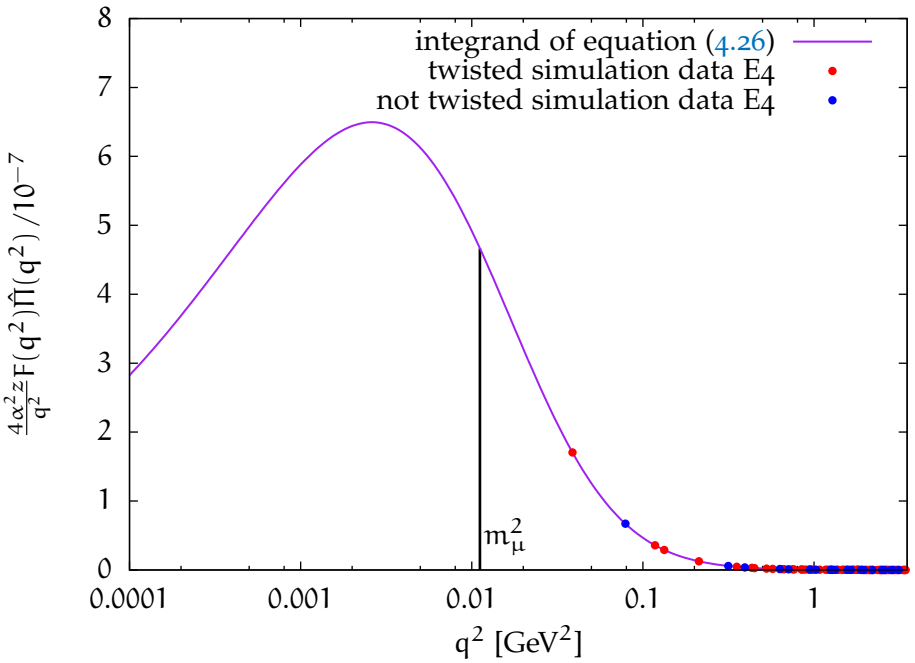

Figure 18: Showing the whole integrand of equation (4.26) for a suitable fit function on the E4 ensemble and the range of the data points twisted and without twisting on a logarithmic momentum scale

5

DETERMINATION OF a_μ

To determine a_μ, a reliable functional representation of the q^2-dependence is required to describe the vacuum polarization amplitude $\Pi(q^2)$ in order to integrate equation (4.26) to obtain its the contribution to the anomalous magnetic moment a_μ. Therefore different types of functions should be considered: Model-independent functions, such as polynomials and Padé approximations, and physically motivated functions. Since the behavior of the vacuum polarization is not known for low momentum transfer, model-independent functions also serve as an approximation. These function show no model dependence, but that does not imply that there are no ambiguities, as different choices of fit functions may produce different results. Estimators motivated by physics can be obtained from effective field theories like chiral perturbation theory or continuum perturbation theory.

5.1 NUMERICAL AND FITTING TECHNIQUES

In a least-squares fit the quantity χ^2 is defined as:

$$\chi^2 = \sum_{i=1}^{n} \frac{(f(\alpha, x_i) - y_i)^2}{\sigma_i^2}. \tag{5.1}$$

Given the set of n data points x_i, y_i and its errors σ_i, χ^2 has to be minimized with respect to the m parameters α of the fit function f. If the data points can be considered to be statistically independent, an uncorrelated fit should be performed using equation (5.1).

If the data points are not statically independent, they show a correlation among themselves which is reflected by the covariance matrix C. In this case the χ^2 can be written in a more general way as:

$$\chi^2 = \sum_{i=1}^{n} \sum_{j=1}^{n} (f(\alpha, x_i) - y_i)\, C_{ij}^{-1} \left(f(\alpha, x_j) - y_j\right). \tag{5.2}$$

The quantity χ^2_{red} is obtained by dividing the χ^2 by the numbers of degrees of freedom $n - m$. In a perfect normal distributed case the χ^2_{red} should have an expectation value of 1. If the χ^2_{red} is far bigger than 1, the data is not described well by the fit function. For the case of χ^2_{red} far smaller than 1, the fitted function describes the data better than expected by statistics.

One crucial problem is the minimization of χ^2, since depending on the fit function this is a non-linear minimization problem, which may contain many

local minima. So an efficient minimization algorithm is needed to obtain the global minimum. The *Levenberg-Marquardt-algorithm* [47] has shown to produce stable results compared to different minimization algorithms like random search or simulated annealing [48] in the framework Mathematica by Wolfram Research [49]. The Levenberg-Marquardt-algorithm has been integrated into the fit programs by me.

For all fits *Singular Value Decomposition* [50] of the covariance matrix has been applied. Singular Value Decomposition allows to factorize a (n,m)-matrix A in the following form:

$$A = U \Sigma V^*. \tag{5.3}$$

The matrices U and V are unitary (m,m)- and (n,n)-matrices. The matrix Σ is a diagonal (m,n)-matrix with sorted l non-vanishing singular values $\sigma_1 > \ldots > \sigma_l$ on the diagonal. If the matrix A is a positive definite (n,n)- matrix, it can be inverted via

$$A^{-1} = V \Sigma^{-1} U^*, \tag{5.4}$$

where Σ^{-1} is a diagonal matrix with the reciprocal singular values $\frac{1}{\sigma_1} \ldots \frac{1}{\sigma_n}$ on its diagonal. This procedure is used to invert the covariance matrix, which is needed for the calculation of χ^2. The covariance matrix is by definition a positive definite (n,n)-matrix, so the singular value decomposition is applicable. Using the singular values, the condition number $\kappa = \frac{\sigma_1}{\sigma_n}$ of a matrix, which estimates numerical instabilities, is constructed in a simple way. The estimated covariance matrix for the simulation data shows in some cases a condition number greater than 10^9 causing numerical difficulties when being inverted. Data points producing singular values five orders of magnitudes smaller than the biggest singular value $\sigma_i < 10^{-5} \cdot \sigma_1$ are eliminated by setting the inverse singular value to zero. So numerical errors are avoided and the covariance matrix is thinned out to reduce the dimensionality of the minimization problem for χ^2. Otherwise the minimization fails frequently. In order to have fits which describe the data, this thin out method using SVD is mandatory and applied to all data sets.

5.2 FITTING THE VACUUM POLARIZATION AMPLITUDE $\Pi(q^2)$

An approach to extract the vacuum polarization can be obtained by a cubic spline to the data. By construction the cubic spline produces a two times continuously differentiable function, which can be used to extract the contribution to a_μ. Since the value at zero momentum is needed a fit has to be performed anyway. Nevertheless, a spline is known to work well for interpolations but not for extrapolations.

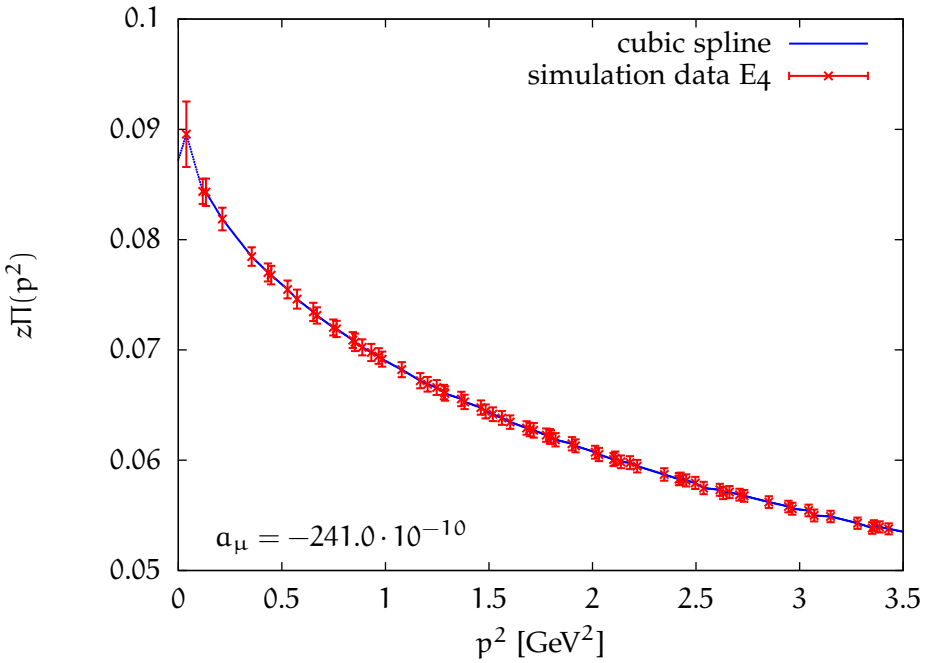

Figure 19: Cubic spline to E4 ensemble

Figure 19 shows an example of a cubic spline applied to the E4 ensemble. Obviously the spline fails to produce a reasonable value for the magnetic moment as expected. The reason is seen in the low momentum region in which the spline turns down leading to a negative value for a_μ. Also for other ensembles this splines approach does not produce reasonable values. The cubic spline demonstrates that any direct numerical integration of the vacuum polarization amplitude is not sufficient to obtain a_μ.

In the following four different approaches to determine the q^2 dependency will be compared. In order to test the stability of the fits, different fit intervals have been used for the fits. Varying the intervals corresponds to the variation of the degrees of freedom in χ^2.

A simple ansatz for the fit is a polynomial in q^2. A general polynomial is of the form

$$f(x = q^2) = \sum_{i=0}^{m} a_i \, x^i, \tag{5.5}$$

where a_i are the free parameters of this ansatz. Tests show that polynomials seem to undershoot the region of low momentum which is essential for the determination of a_μ. Also outside the fitting interval, especially for large momentum, the function does not describe the data at all, which can be seen in figure 20. Indeed it is well-known that polynomial fits are more suited to interpolate data than extrapolate values. As an illustration, the fits and the results for a_μ are shown in the corresponding figures. The integration, needed to extract a_μ shown

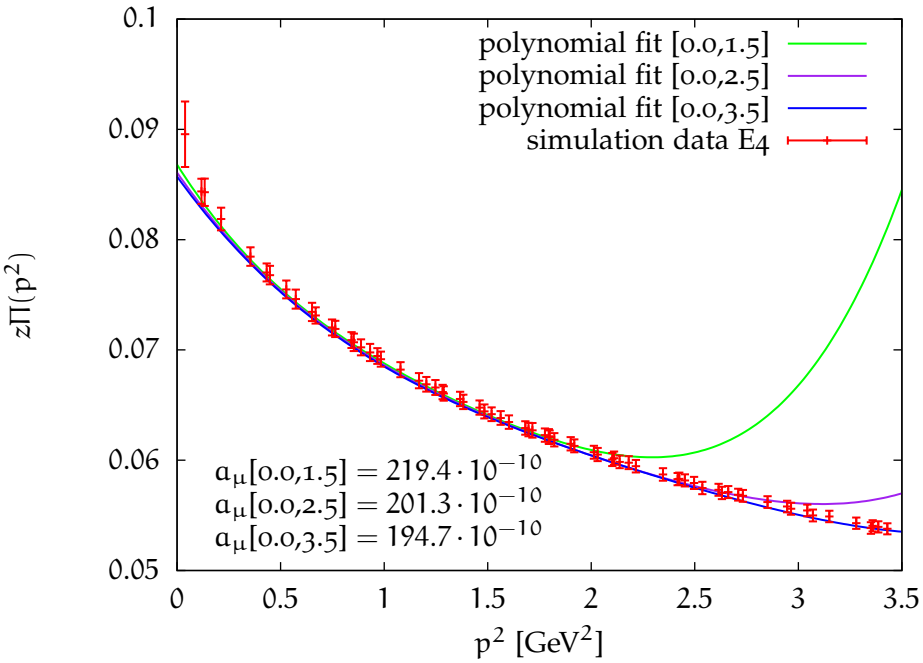

Figure 20: Polynomial of order 4 fit on E4 for different intervals

in equation (4.26), can be performed here in the fitting interval exclusively. Since the fits over different intervals produce a wide range of results for a_μ and the extrapolation shows a trend to smaller values as the interval length increases, this ansatz is discarded.

Aubin and Blum [33] showed the dominance of a tree-level vector contribution in the vacuum polarization $\Pi(q^2)$. This could serve as an ansatz for a fit function, with the vector mass m_V and its decay constant f_V as free parameters:

$$f(q^2) = \frac{\alpha}{3\pi} \frac{(4\pi f_V)^2}{q^2 + m_V^2} + C. \tag{5.6}$$

The fits to the vector dominance model are shown in figure 21. These show similar problems as the polynomial fits and exhibit a trend to smaller values of a_μ when increasing the fit intervals. Here the problem might be the relatively small number of parameters. If the fit interval is increased the vector dominance curve reduces in the low momentum region, which can be seen in figure 21.

A completely different approach is to postulate a simple model for the dispersion relation $R(s)$ and to obtain a function for the vacuum polarization using the optical theorem discussed in section 3.4. Such a model has been introduced by Göckeler in [31]. In the expression

$$R(s) = A\,\delta(s - m_V^2) + B\,\Theta(s - s_0) \tag{5.7}$$

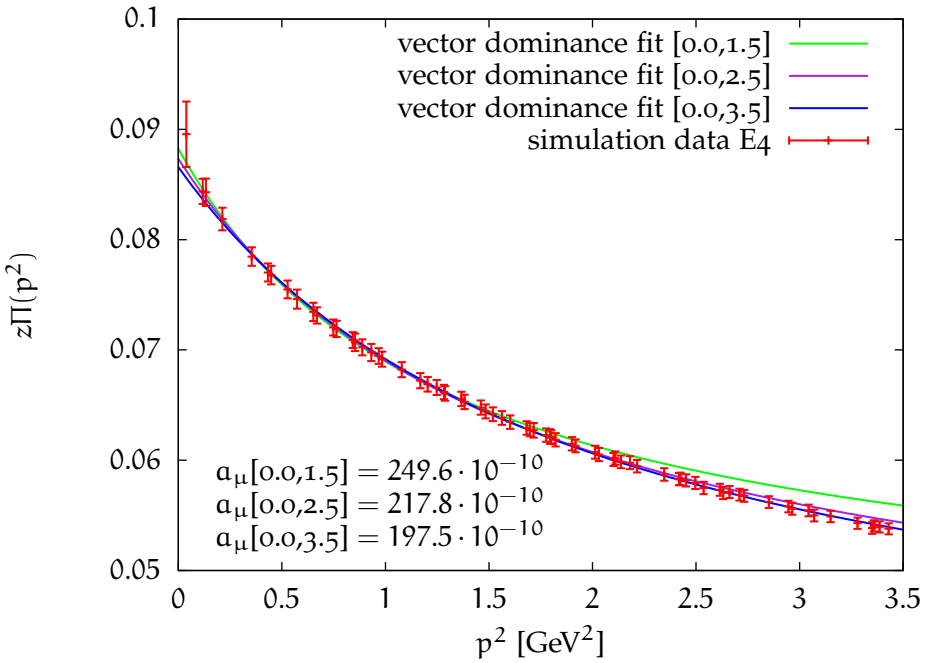

Figure 21: Vector dominance fit on E4 for different intervals

a δ peak models the vector resonance and a Heaviside function the threshold for the production of hadrons. Inserting this into equation (3.14) and performing the integration in equation (3.15) leads to a functional form like:

$$f(q^2) = B \ln\left(q^2 + s_0\right) - \frac{A}{q^2 + m_V^2} + C. \tag{5.8}$$

The combination of logarithmic and rational parts result in a highly non-linear function, including also the vector dominance model. In total there are five free parameters B, s_0, A, m_V, C to be determined. Figure 22 show the result of three different fits to the dispersion relation motivated fit function in equation (5.8) for variable fit intervals. The tendency for the estimate of a_μ to decrease with increasing q^2-interval is reduced.

In order to compare the results of the fit motivated by the dispersion relation, a different set of function with comparable properties is needed. A model independent approximation known to work well for extrapolations is obtained by the *Padé-Approximation*, a ratio of two polynomials of order n and order m:

$$f(x = q^2) = \frac{a_0 + \sum_{i=1}^{n} a_i\, x^i}{\sum_{i=1}^{m} b_i\, x^i}. \tag{5.9}$$

Since the definition (5.9) contains singularities in the first quadrant, it is useful

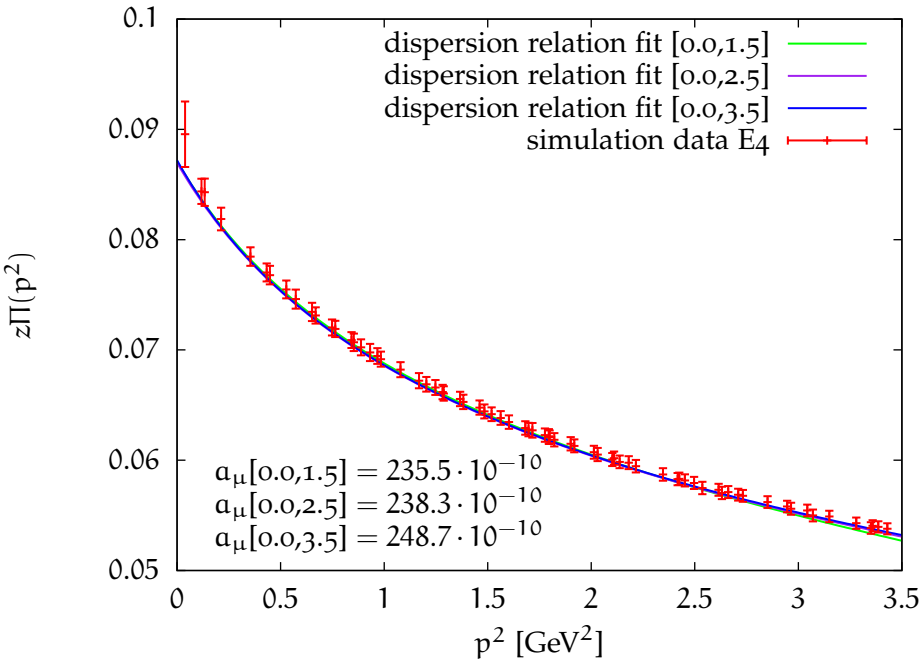

Figure 22: Dispersion relation motivated fit on E4 for different intervals

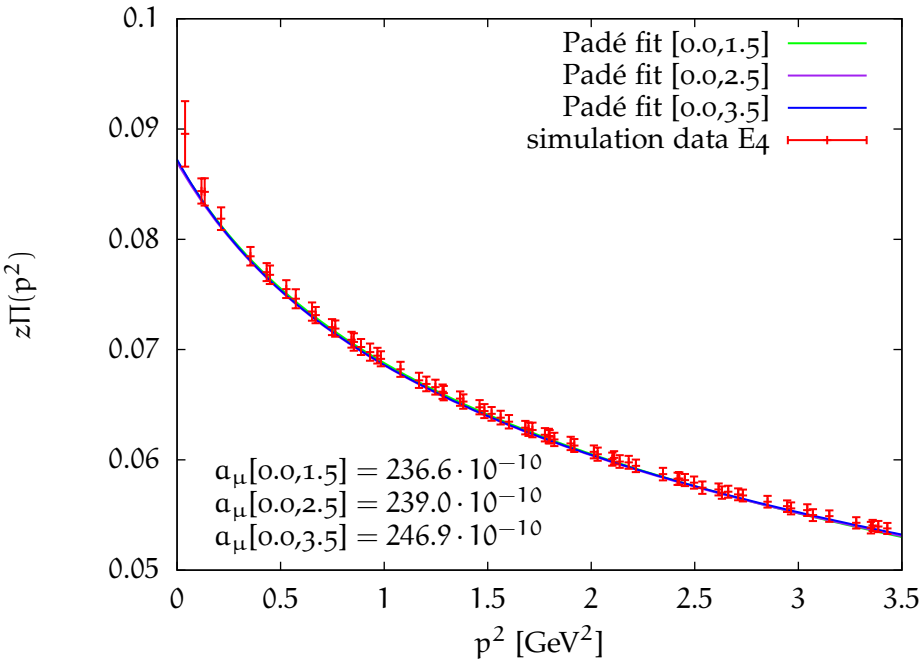

Figure 23: Padé fit with $n = 3$ and $m = 2$ to E4 for different intervals

to rewrite the polynomials in a different form in order to avoid singularities. The new basis for the fits is

$$f(x = q^2) = \frac{c_0 \prod_{i=1}^{n} (x + c_i^2)}{\prod_{i=1}^{m} (x + d_i^2)}, \tag{5.10}$$

where the c_i, d_i are free parameters of this ansatz. This function again is non-linear and therefore the Levenberg-Marquardt algorithm is applied to perform the fits. As expected the Padé fits reproduce similar results as the dispersion relations shown in figure 23. Here the behavior of the data is reflected by the function even outside the fit range.

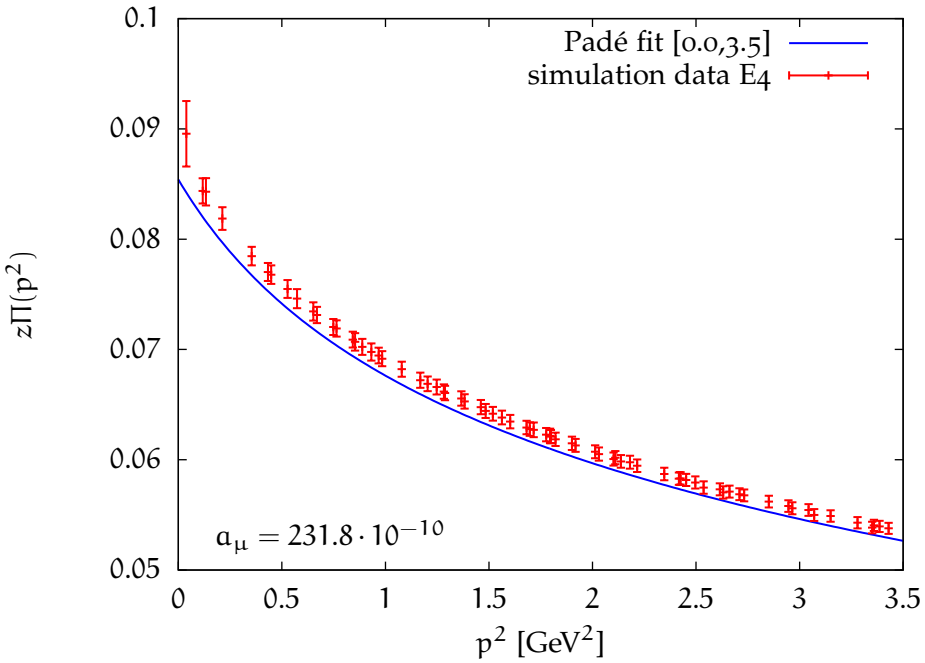

Figure 24: Padé fit with $n = 3$ and $m = 2$ to E4 without reducing the covariance matrix using Singular Value Decomposition based thinning out method.

Figure 24 shows a Padé-fit, exactly with the same initial conditions for the fit in figure 23, but without the use of the thinning method based on Singular Value Decomposition discussed in 5.1. As it can be seen in figure 24, the fitting procedure fails to deliver a good description of the data. Correlated fits frequently show the problem of missing a good description of the data. SVD is crucial for an accurate and reliable modelling of the q^2-dependence.

5.3 COMPARISON WITH CHIRAL PERTURBATION THEORY

Another approach to obtain the vacuum polarization, which does not require any lattice data, is to use chiral perturbation theory. Here the masses of the heavy quarks charm, bottom and top are fixed to infinity and the theory can be expanded around the chiral limit of exactly massless up, down and strange quarks. The vacuum polarization can be evaluated in this approach, which has been done by Golowich and Kambor [51] up to 1-loop contributions. This

formula has been adapted to address the connected diagram in figure 13 (a) by Jüttner and Della Morte [36]. The resulting formula for the vacuum polarization

$$\hat{\Pi}(q^2) = \frac{10}{9}\frac{1}{4\pi^2}\sqrt{1+\frac{4m_\pi^2}{q^2}}\ln\left(\frac{\sqrt{1+\frac{4m_\pi^2}{q^2}}+1}{\sqrt{1+\frac{4m_\pi^2}{q^2}}-1}-2\right) \tag{5.11}$$

contains no free parameters and is shown in figure 25 together with the simulation data for E4. Since here the vacuum polarization $\Pi(q^2)$ is plotted and

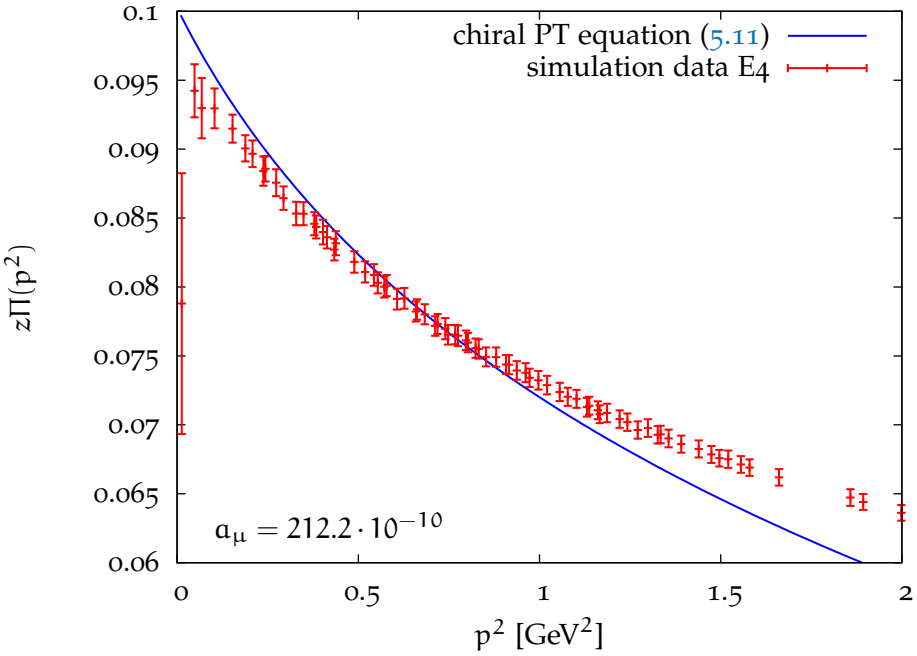

Figure 25: Comparison of chiral pertubation theory for the vacuum polarization with the lattice data from the F6 ensemble

not the difference $\Pi(0) - \Pi(q^2)$ an additional constant is needed, which has been matched to an intermediate data point of F6. The F6 ensemble is lightest ensemble studied in this work corresponding to a pion mass of *297.9 MeV*. The chiral perturbation curve does not describe the simulation data in the low and high momentum region. The obtained result for the anomalous magnetic moment a_μ consequently does not compare to the results determined by fits. Lattice artefacts and a relative heavy pion mass can be considered to deliver an explanation for the mismatch. The chiral perturbation theory treats masses as a small perturbation, which might not be fulfilled for a pion twice as heavy as in nature.

5.4 ERROR ESTIMATION

The hadronic contribution to the anomalous magnetic moment a_μ can be determined in a few steps. The first step is to determine $\hat{\Pi}(q^2)$ from a fit as described in the previous section. The result is multiplied by the kernel $F(q^2)$, shown

in equation (4.27), to obtain the integrand. The next step is to evaluate the convolution integral in equation (4.26) to obtain a_μ using numerical integration. This work uses the *QAG adaptive integration* of the GNU Scientific Library [53, 54]. Since the main contributions come from the low momentum region, an integration algorithm that samples this important region with more details is needed. The algorithm from the GNU Scientific Library is an adaptive algorithm which decomposes the integration interval into several smaller intervals, concentrating on the important low-momentum part. The error of the numerical integration is chosen to be below 10^{-4}, so its contribution to the error can be completely neglected. The results have been in several cases cross-checked with the numerical integration routine of *Mathematica*. Although the fits show a stable behavior in the region in which data points occur, those fits can be completely wrong in a momentum range outside the data points due to the extrapolation and as discussed in the previous chapter. The integral is truncated at a value, so that the contribution for a_μ is estimated accurately enough. The integration interval is chosen to include all data points for the different ensembles. This means for the D ensembles the momentum is integrated up to $6.5\,\mathrm{GeV}^2$, the E ensembles up to $3.5\,\mathrm{GeV}^2$ and the F ensemble up to $2.0\,\mathrm{GeV}^2$. A systematic error arises from the truncation of the integration interval which has been roughly estimated by using a constant for $\hat{\Pi}(q^2 \geqslant q^2_{\mathrm{cut}})$. Here the first data point of the lightest ensemble is used for the estimation of this constant. This should limit the error to its upper bound:

$$\begin{aligned} a_\mu[q^2 \geqslant 2.0\mathrm{GeV}^2] &\leqslant 3 \cdot 10^{-10}, \\ a_\mu[q^2 \geqslant 3.5\mathrm{GeV}^2] &\leqslant 1 \cdot 10^{-10}, \\ a_\mu[q^2 \geqslant 6.5\mathrm{GeV}^2] &\leqslant 3 \cdot 10^{-11}. \end{aligned} \tag{5.12}$$

To estimate the statistical error of the contribution to the anomalous magnetic moment a_μ the *Jackknife* error procedure [55, 43] is applied. The Jackknife method is a statistical re-sampling method which allows to estimate a statistical error and the covariance matrix on a data set. A Jackknife-sample

$$z_{\beta,i} = \frac{1}{N_{cfg} - 1} \sum_{\alpha=1,\alpha\neq\beta}^{N_{cfg}} y_{\alpha,i} \tag{5.13}$$

is obtained by removing one configuration from the determination of the gauge average of a quantity. In general more than one configuration can be removed to construct a Jackknife sample, but here a single-elimination Jackknife is used to obtain the gauge average and its statistical error. Assuming there are N_{cfg} configurations for the gauge average formulated with Greek indices and n data

points for a quantity y shown in Latin indices, the gauge average and the error of a data point i can be calculated by:

$$\bar{z}_i = \frac{1}{N_{cfg}} \sum_{\alpha=1}^{N_{cfg}} y_{\alpha,i}, \tag{5.14}$$

$$\sigma_i^2 = \frac{N_{cfg}-1}{N_{cfg}} \sum_{\beta=1}^{N_{cfg}} \left(z_{\beta,i} - \bar{z}_i\right)^2 . \tag{5.15}$$

The covariance matrix C_{ij} is obtained by

$$C_{ij} = \frac{N_{cfg}-1}{N_{cfg}} \sum_{\beta=1}^{N_{cfg}} \left(z_{\beta,i} - \bar{z}_i\right) \cdot \left(z_{\beta,j} - \bar{z}_j\right) . \tag{5.16}$$

The factor $\frac{N_{cfg}-1}{N_{cfg}}$ takes the reuse of data-samples into account. This covariance matrix is used to perform a correlated fit, using the definition of χ^2 in equation (5.2). A fit for each Jackknife sample is performed and used to obtain one

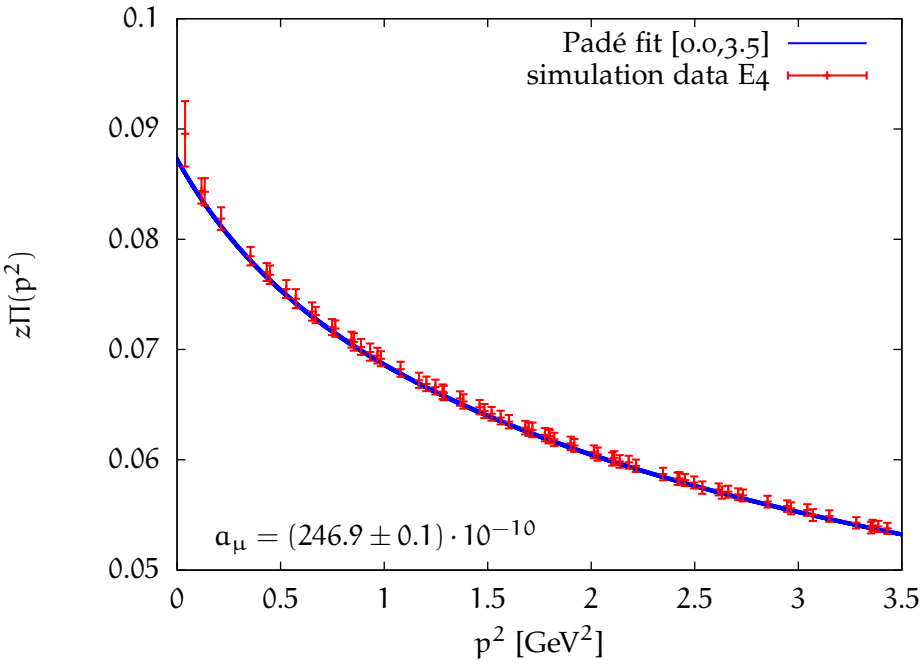

Figure 26: Padé fits $n = 3$, $m = 2$ to E4 ensemble for all Jackkife-samples

value for a_μ using equation (4.26). A narrow blue band in figure 26 represents fits to the entire set of 162 Jackknife samples. Since the deviations are that small, the resulting statistical Jackknife error is tiny. For the E4 ensemble and a fit range of $0.0 - 3.5\,\text{GeV}^2$ this procedure results in:

$$a_\mu[0.0 - 3.5\,\text{GeV}^2, \text{E4}] = 246.92(0.09) \cdot 10^{-10}. \tag{5.17}$$

There are two types of errors: statistical and systematic errors. The statistical errors, estimated by a Jackknife procedure, cover the statistical fluctuations in

the data points relevant for the fits. A systematic error has been introduced by the truncation of the integral necessary for the determination of a_μ. In addition different fit function and intervals show various results. The systematic uncertainty of a_μ can be estimated by the spread of different fit functions and degrees of freedom. After sorting the results, the spread of the central 68% estimates the systematic uncertainty. In this way outliers are not overestimated. These systematic effects dominate the estimation of the error on a_μ. The statistical uncertainty can be neglected compared to the estimated systematic uncertainty. On top of that, there are inherent systematic errors of the lattice approach, like finite volume and finite lattice spacing just to mention a few examples, which have to be studied in detail.

6

RESULTS

In this chapter the results for a_μ on the studied $\beta = 5.3$ ensembles are shown. The necessary fits describing the q^2-dependence have been performed using the techniques from the previous chapter. At first ensembles with different volumes are studied in order to identify volume effects. After presenting the result for a_μ, the chiral extrapolation to the physical value for m_π is performed. In addition a comparison to other lattice simulations is shown in the last section of this chapter.

6.1 VOLUME EFFECTS

Volume effects are the result of simulations in a finite box with periodic boundary conditions due to correlations between two points. These volume effects are expected to increase for smaller values of $m_\pi L$. There are three sets of ensembles D2 $\leftrightarrow$ E2, D3 $\leftrightarrow$ E4 and D5 $\leftrightarrow$ E5, which have the same input parameter κ and β but different volumes $L = 1.7\,\text{fm} \leftrightarrow L = 2.2\,\text{fm}$. These ensembles allow to study volume effects on the vacuum polarization. The following figures show the hadronic vacuum polarization for the corresponding ensembles plotted on top of each other.

The ensembles D2 and E2 corresponding to a pion mass $\sim 700\,\text{MeV}$ show almost no sign of volume effects in figure 27. A minimal trend to lower values can be observed for the data of D2 ensemble in red. The values for a_μ determined from different fits

$$\begin{aligned} a_\mu^{(D2)} &= 184.3(4.4) \cdot 10^{-10}, \\ a_\mu^{(E2)} &= 177.5(1.3) \cdot 10^{-10}, \end{aligned} \tag{6.1}$$

differ by 1.5 σ. One expects that in these rather heavy ensembles the volume effect should not be visible, probably the error is underestimated for the E2 ensemble, since the data almost agree with each other.

The next set of ensembles cover D3 and E4 lattices in which the corresponding pion mass has a value of $\sim 550\,\text{MeV}$. For these ensembles the data for the smaller lattice $L = 1.7\,\text{fm}$ in figure 28 lie below those corresponding $L = 2.2\,\text{fm}$ data, nevertheless both data sets do agree within the statistical uncertainties except of the first data point. The hadronic contribution to a_μ for those ensembles have been evaluated to:

$$\begin{aligned} a_\mu^{(D3)} &= 245.2(6.7) \cdot 10^{-10}, \\ a_\mu^{(E4)} &= 243.9(3.8) \cdot 10^{-10}, \end{aligned} \tag{6.2}$$

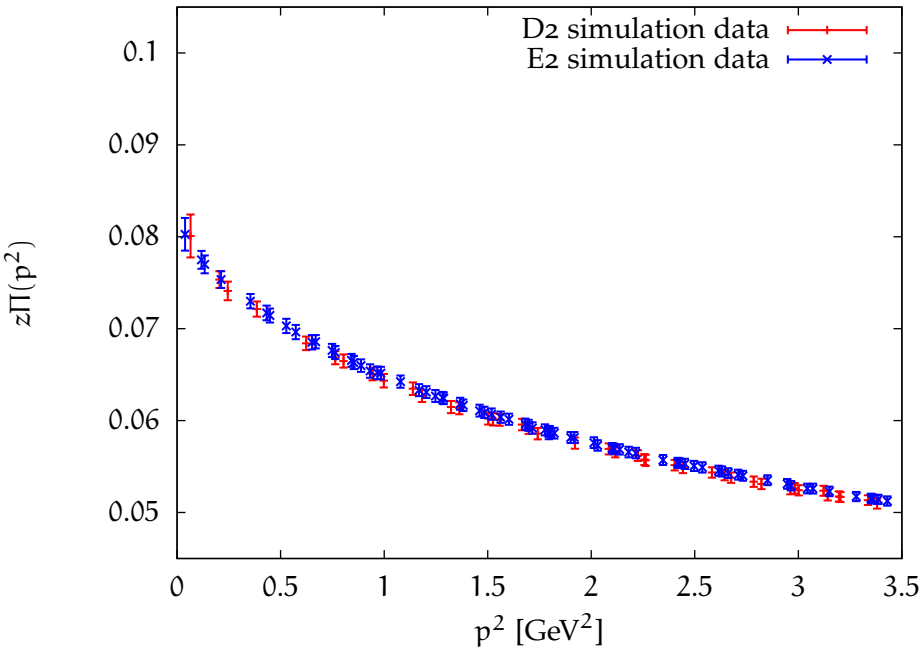

Figure 27: Vacuum polarization for two different ensembles with different volume: D2 L = 1.7 fm in red and E2 L = 2.2 fm in blue

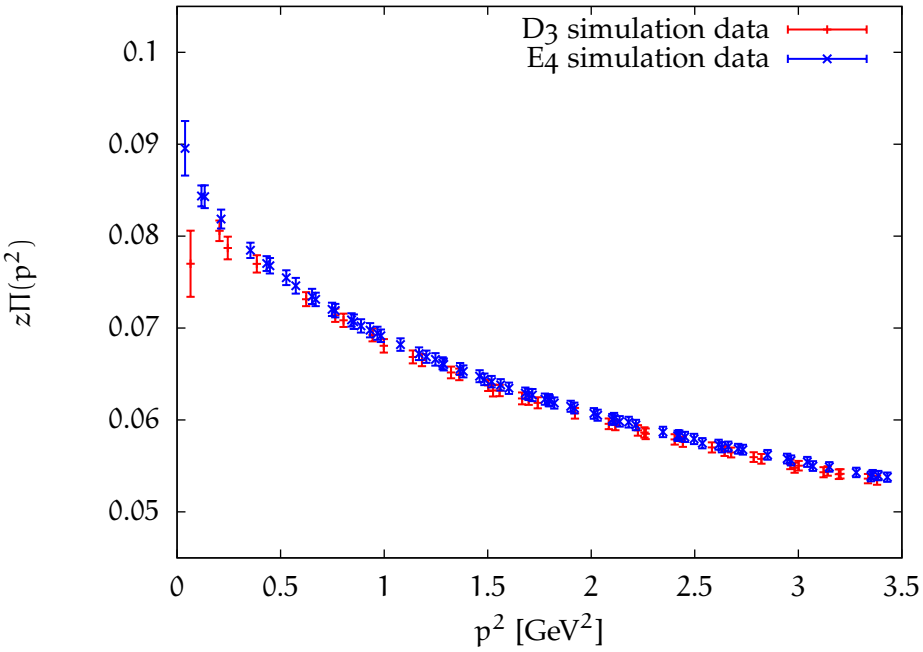

Figure 28: Vacuum polarization for two different ensembles with different volume: D3 L = 1.7 fm in red and E4 L = 2.2 fm in blue

which perfectly agrees within the error bars and no volume effect is visible.

Finite volume effects should be larger at the smaller pion mass of ~ 425 MeV. The data for the smaller volume, plotted in red, lie significant below the corre-

sponding ensemble, but still agree within the statistical errors. This trend can be seen in figure 29 and affects the calculation of contribution to a_μ. The results for a_μ:

$$a_\mu^{(D5)} = 282.3(20.3) \cdot 10^{-10}, \qquad (6.3)$$
$$a_\mu^{(E5)} = 329.6(8.4) \cdot 10^{-10}$$

show a difference of 2.3 σ. So the volume has an influence of more than 14% on the determination of the vacuum polarization.

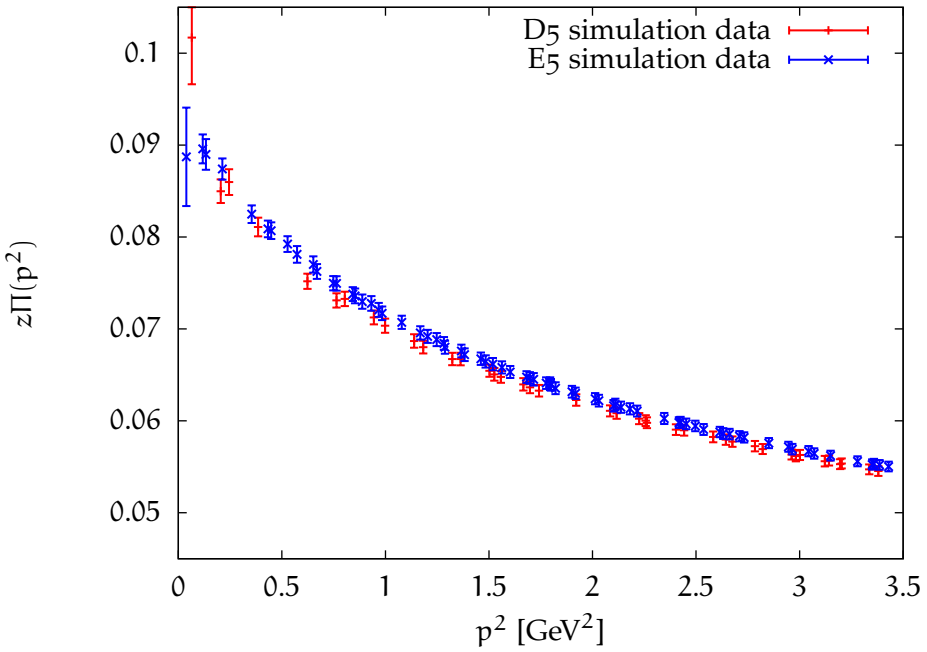

Figure 29: Vacuum polarization for two different ensembles with different volume: D5 L = 1.7 fm in red and E5 L = 2.2 fm in blue

6.2 RESULTS FOR a_μ

The vacuum polarization has been determined for the 11 different ensembles of table 2. The methods described in chapter 5 have been applied to determine the hadronic contribution to a_μ. In order to estimate a systematic error, five different fit functions have been used: Padé with $n = 3, m = 2$; Padé with $n = 3, m = 3$; Padé with $n = 4, m = 3$; Padé with $n = 4, m = 2$ and the fit motivated from dispersion relation defined in equation (5.8). The fits are varied over seven fit ranges individually, so in total there are 35 evaluations of a_μ in each ensemble serving as an estimator for the spread of the real value. The median of the 35 distributed results is used as an estimator for a_μ, since the median is more robust to outliers than the arithmetic mean. After sorting the results, the spread of the central 68% serves as an estimator for the uncertainty of a_μ. This systematic error dominates the uncertainty of a_μ, so the statistical

Jackknife error can be neglected completely. The individual fit results can be found in appendix A, showing the degrees of freedom and the χ^2_{red}. The results are presented in table 3 for the $N_f = 2$ and the $N_f = 2+1$ partially quenched simulations. A graphical representation of those result is shown in figure 30.

	$N_f = 2$	$N_f = 2+1$ PQ
name	$a_\mu/10^{-10}$	$a_\mu/10^{-10}$
D1	108.1(3.2)	–
D2	184.3(4.4)	231.1(15.6)
D3	245.2(6.7)	292.3(5.8)
D4	237.9(10.3)	274.1(5.5)
D5	282.3(20.3)	317.3(19.5)
E2	177.5(1.3)	221.9(2.3)
E3	194.6(5.6)	234.5(3.3)
E4	243.9(3.8)	288.4(4.6)
E4 no twist	227.7(7.2)	275.9(8.7)
E5	327.6(8.4)	368.0(13.4)
F6	408.2(10.8)	452.7(14.5)

Table 3: Results for a_μ in $N_f = 2$ and $N_f = 2+1$ partially quenched simulations

The estimated errors increase when going to lighter pion masses, since the fluctuations in the low momentum region are increased. These fluctuations reflect the errors of the fits. In order to see the effect of partially twisted boundary conditions, one particular ensemble, the E4 ensemble, has been studied in the same way without twisting. It produces a value for a_μ which is 10% smaller, but whose error is twice as large. The different results for a_μ are due to the lack of data points in the low momentum region.

If the three quarks are degenerate, the additional contribution of the strange quarks would add up a correction of 20%, which comes from the increased charge factor z. If the strange quark is more massive than the up and down quarks, as in nature, its contribution to a_μ shrinks. All partially quenched $N_f = 2+1$ simulations results lie as expected above the corresponding $N_f = 2$ results, which confirms the expectations. In the D3 ensemble the degenerate case is almost fulfilled, here the additional contribution is 20.5%, which is close to the expectation.

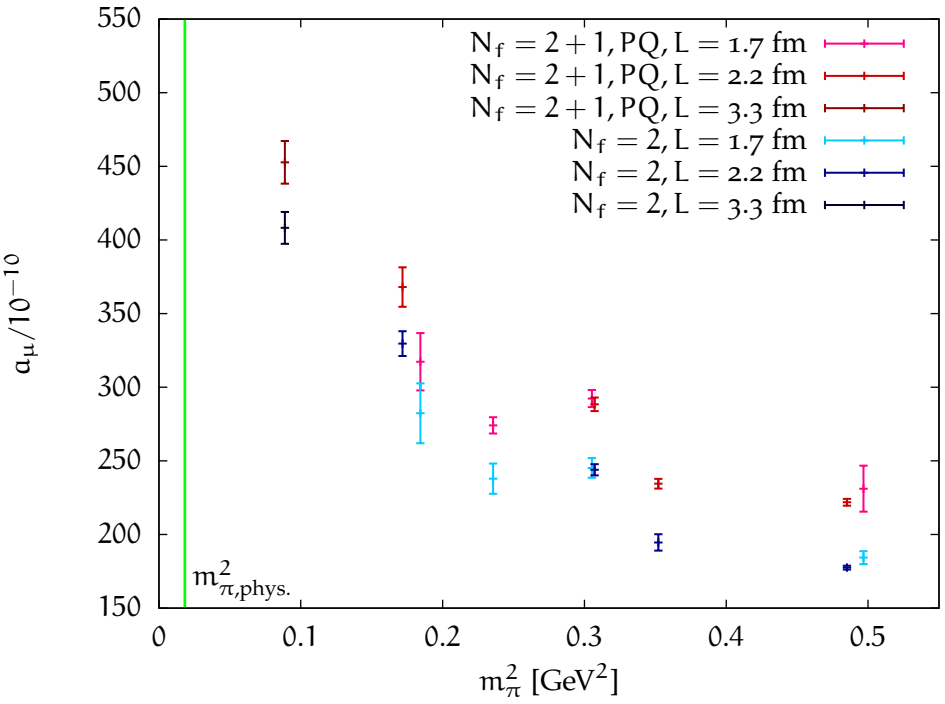

Figure 30: $N_f = 2$ results in blue colors and $N_f = 2+1$ partially quenched results in red colors for a_μ plotted against the pion mass. Vertical line: physical pion mass

6.3 CHIRAL EXTRAPOLATION OF a_μ

All simulations correspond to a pion mass heavier than in nature. So simulations for different pion masses have been performed to enable yet another extrapolation of a_μ to the physical point $m_\pi = 134.9766(6)^{\text{MeV}}/c^2$ [46].

Since there is no theoretical constraint on the chiral behavior, again different ansätze are possible. The chiral perturbation theory for two flavors up to 1-loop has no free parameters left in $\hat{\Pi}(q^2)$.This ansatz for the vacuum polarization can be integrated to obtain a_μ. The chiral curve has been matched to the F6 ensemble, the ensemble with the smallest pion mass studied in this work, by adding a constant offset. Chiral perturbation theory should be valid in a range of small pion masses, since the masses of the quarks are treated as perturbation. In section 5.2 the chiral perturbation theory ansatz did not describe the simulation data for the vacuum polarization $\Pi(q^2)$, although it reproduced the chiral behavior for small pion masses to some extent. Anyway, higher order corrections are needed in order to have a better description of the whole range of data points. Using the chiral perturbation theory formula, the vacuum polarization at the physical point is given by:

$$a_\mu = 828.2(10.8) \cdot 10^{-10}. \tag{6.4}$$

The error is difficult to determine, but by construction is given by the error on the F6 ensemble. Probably the error is underestimated in such a simple

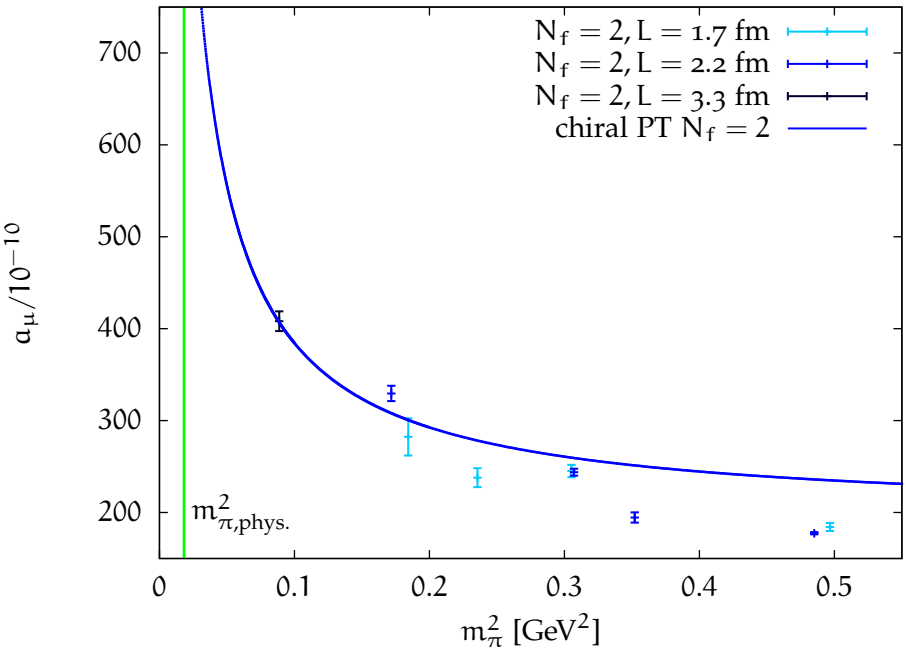

Figure 31: Chiral perturbation theory applied to $N_f = 2$ results matched to F6

evaluation. The value for a_μ and its error are listed here for comparison, since the chiral perturbation theory does not reflect other data points. The result from chiral perturbation theory is larger than the current world average, which has been discussed in section 3.4. The estimate in (6.4) is expected to undershoot the value from the PDG, since additional contributions, for instance the contribution from a strange quark, were not considered here. Nevertheless the shape of the curve can help to construct a model for the chiral behavior of a_μ.

Instead of finding an expression for the vacuum polarization, an ansatz for the chiral behavior of $a_\mu(m_\pi^2)$ can be postulated. Motivated by a chiral expansion, a fit function

$$f(m_\pi^2) = A + B \cdot m_\pi^2 + C \cdot m_\pi^2 \ln(m_\pi^2) \tag{6.5}$$

can be used. Here an expansion of a_μ in terms of m_π^2/Λ^2 can be performed, treating the pion mass as a perturbation in units of some arbitrary scale Λ, which can be absorbed into the fitting parameters A, B, C.
Since there are only a few data points, the function should not contain too many parameters in order to perform a reliable fit. The E and F ensembles are used for the chiral extrapolation, since the corresponding D lattices showed relics of finite volume effects. Alternatively, an expansion in polynomials of m_π^2 is possible. With five data points, a expansion up to third order in m_π^2 can be used:

$$f(m_\pi^2) = A + B \cdot m_\pi^2 + C \cdot m_\pi^4. \tag{6.6}$$

In both cases an uncorrelated fit has been performed. Figure 32 shows both functions applied to the $N_f = 2$ and $N_f = 2 + 1$ partially quenched data.

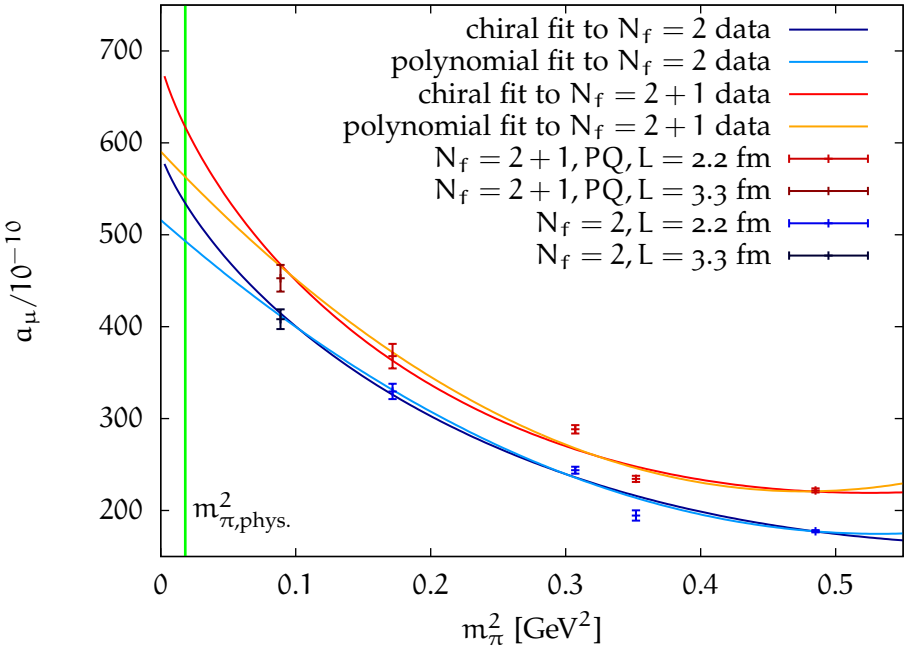

Figure 32: Chiral extrapolation using polynomial fit and chiral fit of equation (6.5)

In figure 31 the chiral perturbation theory indicated a steep dependency on the pion mass, so a non-linear term in the fit function is necessary to describe the behavior of the data. The polynomial and the chiral fit in figure 32 show different extrapolation behavior, which can be used to estimate a systematic uncertainty of a_μ at the physical point. The mean of both fit results serves as an estimate for a_μ, whereas the spread indicates the systematic uncertainty. The extrapolated values are:

$$a_\mu[N_f = 2] = 513.7(20.5) \cdot 10^{-10}, \tag{6.7}$$

$$a_\mu[N_f = 2+1, PQ] = 590.0(27.0) \cdot 10^{-10}. \tag{6.8}$$

The error in this determination could be estimated wrong, since only two fits have been considered. Both fits are constrained by the E2 data point, which has a rather small estimated error. This ensemble corresponds to a pion mass of about 700 MeV, which cannot be considered to be small. The results for a_μ show to be smaller than the phenomenological result by the dispersive approach using e^+e^- data discussed in section 3.4.

6.4 COMPARISON TO OTHER LATTICE CALCULATIONS

This work uses non-perturbatively $\mathcal{O}(a)$ improved Wilson fermions with $N_f = 2$ dynamical quarks. In addtion, partially twisted boundary conditions have been applied to reach lower momentum. In the past, different actions and techniques have been studied to determine the hadronic contribution to the anomalous magnetic moment of the muon. Aubin and Blum in [33] have used improved

rooted staggered fermions with $2+1$ flavors. Twisted mass fermions with 2 flavors have been studied by the European Twisted Mass Collaboration (ETMC) [34]. There have been also quenched simulations in [31, 32], which are not considered in this comparison. Also, as a reference the phenomenological result from the Particle Data Group [25] is shown in the plots.

Figure 33 shows the results for two flavor simulations with twisted mass fermions and our worked based on $\mathcal{O}(a)$ improved Wilson fermions. The results from twisted mass fermions [34] involves statistical errors only. Also a different fit procedure has been applied. ETMC have used polynomial fits to determine the vacuum polarization, which had been show in section 5.2 to deliver unstable results. The results from this work showed small statistical error, but these value were dominated by systematic effects choosing fit function and intervals.

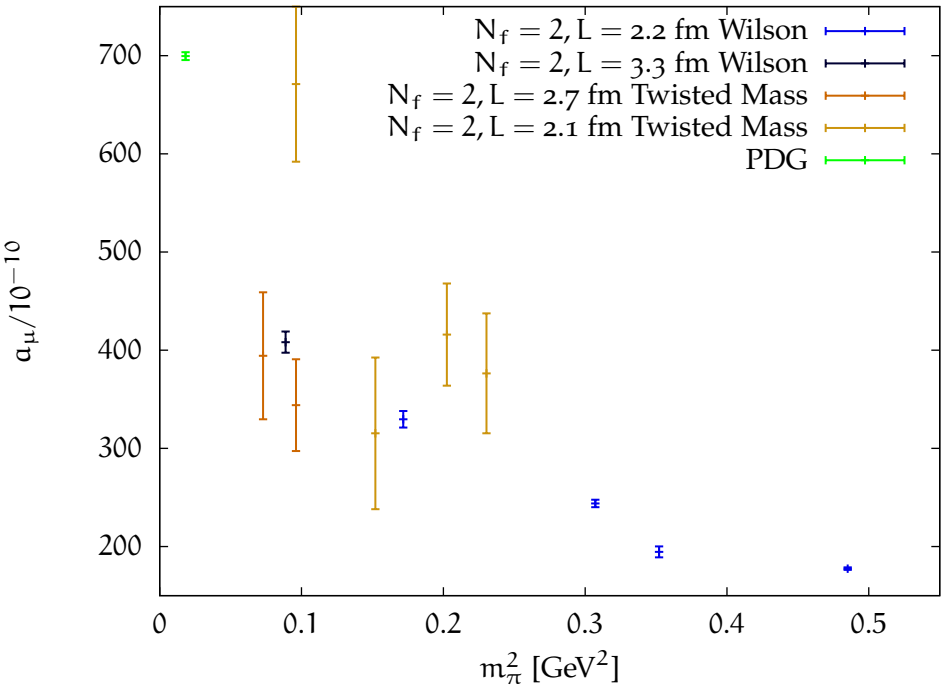

Figure 33: Comparing different actions for a two flavor lattice simulation

The comparison shows that the errors can be improved by using partially twisted boundary conditions and more suited fit functions. If only "untwisted" data would be used to determine the q^2-dependence, the stability of the fits would be impaired, which leads to smaller values with significant increased systematic errors. The values obtain in these different simulations do agree within the estimated errors. One data point of ETMC can be considered as outlier.

Considering the contribution of a strange quark, staggered simulations are performed using dynamical 2+1 flavors, where as this work includes the strange quark quenched. Figure 34 shows the different results obtained for the $N_f = 2+1$ simulations. Small errors and the trend to approach the phenomenological value

as m_π is decreased towards the physical point relies on the use of the staggered chiral perturbative ansatz including a vector dominance model. The errors of the staggered calculation are statistical only and it might be that they are missing systematic effects. If they use a polynomial fit for the momentum dependence of the vacuum polarization, the values for a_μ are different and show a larger error. A cubic fit would lead to lower values whereas a fourth order polynomial fit would produce larger values [33].

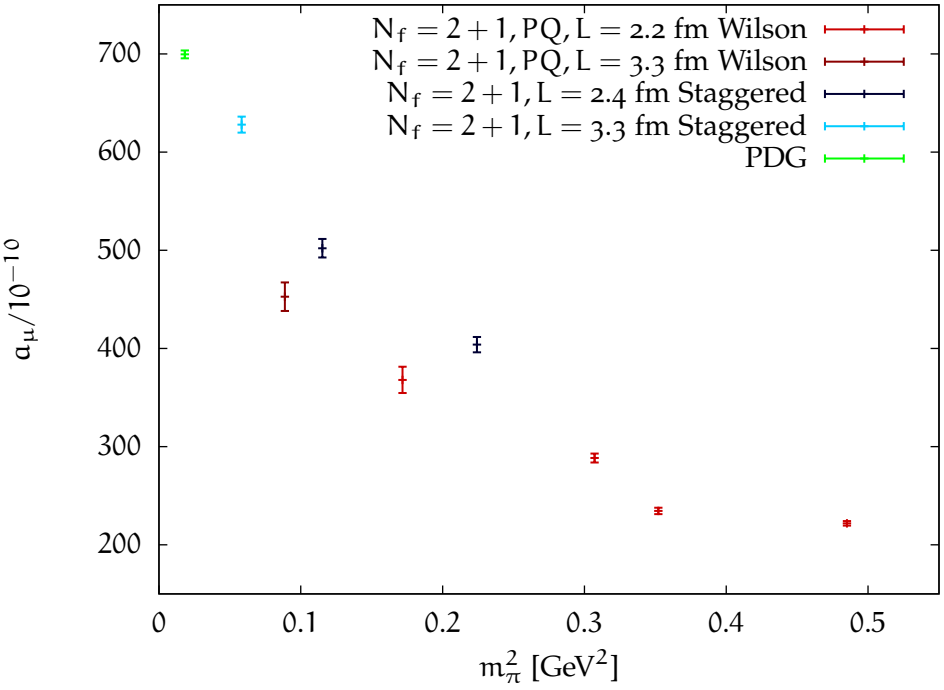

Figure 34: Comparing different actions for $N_f = 2+1$ lattice simulation

The chiral behavior shows to be similar in both calculations, but the result of this work is significantly lower than the staggered result. The gap between the different simulations could indicate an additional contribution by a dynamic strange quark, but it is more likely the systematic errors in the staggered determination are underestimated.

7

SUMMARY AND OUTLOOK

The determination of the hadronic contribution to a_μ is complicated to compute on the lattice since the important momentum region cannot be sampled directly. Partially twisted boundary conditions have shown to improve this situation by adding additional data points to the vacuum polarization. These additional data greatly improve the stability of the fits and the extrapolation to $p^2 = 0$ is more reliable comparing to untwisted data. A particular comparison showed that the systematic error is reduced by a factor of two, if partially twisted boundary condition have been applied to the computation. In addition a trend to lower values for a_μ has been seen, indicating the difficulties of the extrapolation without twisting once more.

To determine the hadronic contribution to a_μ, two different types of fit functions have been used to describe the momentum dependency of the vacuum polarization $\Pi(q^2)$: a Padé approximation and a fit motivated by a dispersion relation. The variation of the degrees of freedom by changing the fit interval has shown to deliver different results, which do not agree within the evaluated statistical uncertainties estimated by Jackknife. The spread of those results has been used to estimate the systematic influence of different fit intervals and functions. These systematic effects dominating the determination of a_μ serve as an estimate for the real errors. Other fit ansätze, especially polynomials, have problems to produce a stable result for a_μ when varying the fit intervals. If polynomials were used, the instability of those fits would increase systematic error significantly.

A chiral extrapolation is needed to obtain the hadronic contribution to a_μ at the physical value of the pion mass. Here two simple models are used to fit the pion mass dependence of a_μ. The models are an improvement of a linear extrapolation taking logarithms or squares into account. Such approaches seem reasonable, since the estimate by chiral perturbation theory discussed in section 5.3, showed a comparable behavior. The number of free parameter is kept small, since only five data points were available for the extrapolation. The error on a_μ at the physical point has been estimated by the spread of both models.

In addition the contribution of a strange quarks has been investigated by performing partially quenched simulations. It shows that the additional contribution from a strange quark, even quenched, can be quite sizeable. The comparison to staggered fermions [33] also indicates that a dynamical strange quark would provide an additional contribution to a_μ.

Having performed all necessary steps to obtain the hadronic contribution to the anomalous magnetic moment of the muon, the result for the two flavor theory is obtained as :

$$a_\mu[N_f = 2] = 513.7(20.5) \cdot 10^{-10}.$$

If a quenched strange quark is included, the result increases to:

$$a_\mu[N_f = 2+1, PQ] = 590.0(27.0) \cdot 10^{-10}.$$

These values for a_μ have been obtained using all currently available E and F ensembles for $\beta = 5.3$, except for the E1 ensemble with an unphysically heavy pion. The E2 ensemble shows a relatively small systematic uncertainty, so the fits used for the extrapolation are strongly constrained by this data point. The E2 ensemble with a pion mass of about $700\,MeV$ is far off the physical value for the pion mass, so it should not be trusted as much as the estimated systematic uncertainty indicates. The estimate obtained for a_μ this work does not agree with the current world average [25]:

$$a_\mu^{PDG} = 695.5(4.1) \cdot 10^{-10}.$$

The result of this work shows a too small value for a_μ compared to the current world average. Since the simulations are not performed to cover full QCD, it would be interesting to see whether a fully dynamical strange quark brings the lattice results closer to the phenomenological estimate. Nevertheless this work has shown that a lattice calculation of the hadronic vacuum polarization can be performed and will be in the future a valuable approach to determine the hadronic contribution to the anomalous magnetic moment of the muon. Lattice QCD allows one to study the strong interaction non-perturbatively and in a pure theoretical framework. In the following a few remarks for further improvements will be made.

The chiral extrapolation can be improved by including ensembles with lighter pion masses. Getting closer to the physical point would show more details on the chiral behavior of a_μ, this would allow to construct a better model for the chiral extrapolation. Chiral perturbation theory could deliver a better approximation by including higher correction, which also could improve the extrapolation model. Lighter ensembles also could supersede the ensembles with a rather large pion mass, so probably the chiral extrapolation would become more reliable. In the near future the F7 ensemble, an ensemble with even lighter pion mass, will be studied, which probably will improve the chiral extrapolation.

If the computing power increases continuously, simulations on lattices larger volumes can be studied in the future allowing to reach to even lower momenta $p_i = \frac{2\pi}{L} n_i$ directly. This of course would improve the extrapolation of the vacuum polarization, which could improve the fit used to determine the hadronic contribution.

Lattice artifacts will be considered in further studies by performing simulations with different lattice spacings a. For a complete analysis this type of systematic errors need to be estimated. In addition the point-split current, introduced in section 4.1, can be $\mathcal{O}(a)$ improved in order to reduce discretization errors.

The contribution to a_μ by the disconnected diagram shown in section 4.1 needs to be computed in order to have a complete lattice determination of the hadronic contribution in leading order. Jüttner and Della Morte [36] have estimated the disconnected diagram using chiral perturbation theory for two flavors, they expect a reduction of the connected diagram by 10%.

The results of this thesis are an important step towards a more reliable determination of a_μ^{had} from first principles, but many other effects must be better controlled before the lattice determination is competitive with phenomenology.

A

APPENDIX

FIT RESULTS FOR MOMENTUM DEPENDENCE OF $\Pi(q^2)$

This appendix shows the plots for all ensembles analysed in this study. Additionally the results for the different fits are listed in the corresponding tables. In some cases the fit procedure failed to produce a reasonable fit for the vacuum polarization, which has different reasons discussed below. These failed fits have been discarded and marked by – in the tables.
Primary the Padé fit converged into a singularity at $p^2 = 0$ for one or more Jackknife samples, which caused a failure of the numerical integration. In some cases the minimization for χ^2 failed to obtain a global minimum within a reasonably high number of iterations, resulting in a $\chi^2_{\text{red}} \gg 1$.

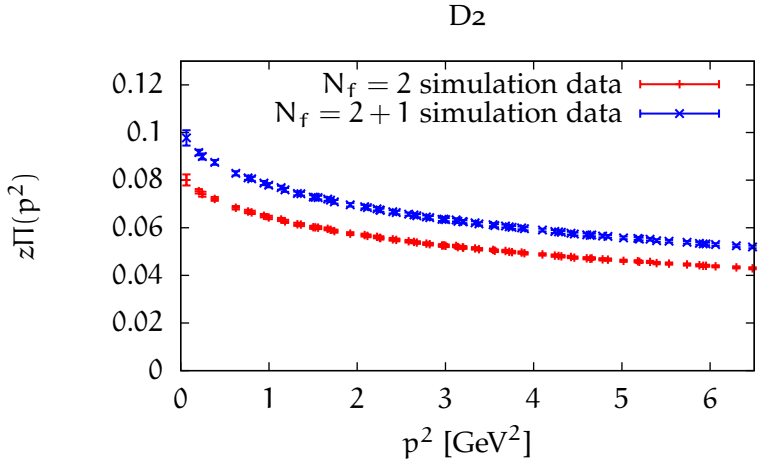

$N_f = 2$					$N_f = 2+1$ partially quenched				
function	interval	N	χ^2_{red}	$a_\mu/10^{-10}$	function	interval	N	χ^2_{red}	$a_\mu/10^{-10}$
pade32	[0.0,2.5]	21	-	–	pade32	[0.0,2.5]	21	-	–
pade32	[0.0,3.0]	28	1.56	185.42 ± 0.13	pade32	[0.0,3.0]	28	1.43	234.71 ± 0.24
pade32	[0.0,3.5]	35	1.44	184.35 ± 0.11	pade32	[0.0,3.5]	35	1.25	261.31 ± 0.32
pade32	[0.0,4.0]	42	1.34	182.64 ± 0.08	pade32	[0.0,4.0]	42	1.16	238.97 ± 0.17
pade32	[0.0,4.5]	48	1.36	184.64 ± 0.08	pade32	[0.0,4.5]	48	1.19	234.82 ± 0.16
pade32	[0.0,5.0]	53	1.44	170.51 ± 0.03	pade32	[0.0,5.0]	53	1.19	231.06 ± 0.16
pade32	[0.0,5.5]	58	1.45	169.30 ± 0.03	pade32	[0.0,5.5]	58	1.19	231.56 ± 0.13
pade33	[0.0,2.5]	20	-	–	pade33	[0.0,2.5]	20	1.74	230.04 ± 0.10
pade33	[0.0,3.0]	27	1.67	185.57 ± 0.13	pade33	[0.0,3.0]	27	1.53	224.25 ± 0.07
pade33	[0.0,3.5]	34	1.54	184.68 ± 0.11	pade33	[0.0,3.5]	34	1.51	217.12 ± 0.06
pade33	[0.0,4.0]	41	1.43	182.66 ± 0.08	pade33	[0.0,4.0]	41	1.35	213.61 ± 0.05
pade33	[0.0,4.5]	47	1.45	184.64 ± 0.08	pade33	[0.0,4.5]	47	1.35	213.86 ± 0.05
pade33	[0.0,5.0]	52	-	–	pade33	[0.0,5.0]	52	1.32	213.92 ± 0.05
pade33	[0.0,5.5]	57	1.48	176.80 ± 0.07	pade33	[0.0,5.5]	57	1.34	212.67 ± 0.04
pade43	[0.0,2.5]	19	-	–	pade43	[0.0,2.5]	19	1.86	230.04 ± 0.10
pade43	[0.0,3.0]	26	1.80	180.86 ± 0.38	pade43	[0.0,3.0]	26	1.62	234.69 ± 0.24
pade43	[0.0,3.5]	33	-	–	pade43	[0.0,3.5]	33	1.60	217.12 ± 0.06
pade43	[0.0,4.0]	40	1.52	182.61 ± 0.08	pade43	[0.0,4.0]	40	1.43	213.61 ± 0.05
pade43	[0.0,4.5]	46	1.54	184.64 ± 0.08	pade43	[0.0,4.5]	46	1.44	213.86 ± 0.05
pade43	[0.0,5.0]	51	1.63	170.51 ± 0.03	pade43	[0.0,5.0]	51	1.40	213.92 ± 0.05
pade43	[0.0,5.5]	56	1.58	176.79 ± 0.07	pade43	[0.0,5.5]	56	1.43	212.67 ± 0.04
pade42	[0.0,2.5]	20	-	–	pade42	[0.0,2.5]	20	1.74	230.04 ± 0.10
pade42	[0.0,3.0]	27	1.67	185.37 ± 0.12	pade42	[0.0,3.0]	27	1.52	234.69 ± 0.24
pade42	[0.0,3.5]	34	1.54	184.28 ± 0.11	pade42	[0.0,3.5]	34	1.32	261.29 ± 0.32
pade42	[0.0,4.0]	41	1.43	182.61 ± 0.08	pade42	[0.0,4.0]	41	1.22	238.97 ± 0.17
pade42	[0.0,4.5]	47	1.45	184.59 ± 0.08	pade42	[0.0,4.5]	47	1.26	234.82 ± 0.16
pade42	[0.0,5.0]	52	1.48	180.02 ± 0.09	pade42	[0.0,5.0]	52	1.26	231.06 ± 0.16
pade42	[0.0,5.5]	57	1.48	176.79 ± 0.07	pade42	[0.0,5.5]	57	1.26	231.55 ± 0.13
disp	[0.0,2.5]	22	-	–	disp	[0.0,2.5]	22	-	–
disp	[0.0,3.0]	29	1.46	191.27 ± 0.21	disp	[0.0,3.0]	29	1.33	250.14 ± 0.28
disp	[0.0,3.5]	36	1.35	191.42 ± 0.18	disp	[0.0,3.5]	36	-	–
disp	[0.0,4.0]	43	1.27	187.11 ± 0.15	disp	[0.0,4.0]	43	1.08	255.95 ± 0.27
disp	[0.0,4.5]	49	1.30	190.58 ± 0.16	disp	[0.0,4.5]	49	1.12	240.92 ± 0.73
disp	[0.0,5.0]	54	1.31	184.83 ± 0.14	disp	[0.0,5.0]	54	1.10	247.50 ± 0.19
disp	[0.0,5.5]	59	1.31	178.88 ± 0.09	disp	[0.0,5.5]	59	1.11	245.07 ± 0.19

Figure 35: Results for different fits on D2 ensemble

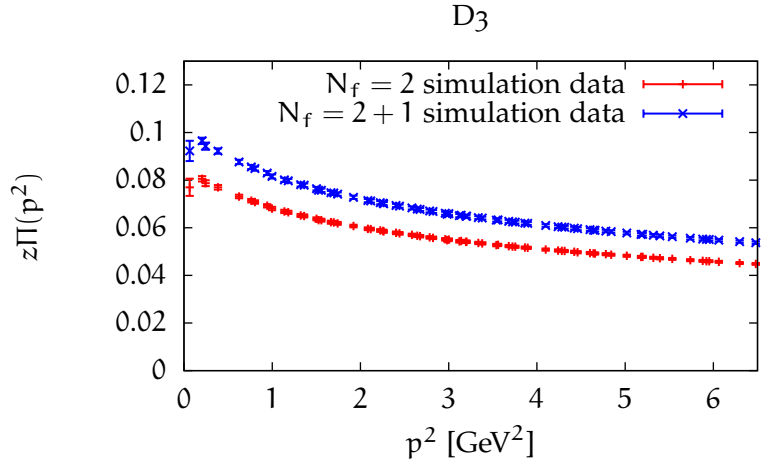

$N_f = 2$					$N_f = 2+1$ partially quenched				
function	interval	N	χ^2_{red}	$a_\mu/10^{-10}$	function	interval	N	χ^2_{red}	$a_\mu/10^{-10}$
pade32	[0.0,2.5]	21	1.58	238.27 ± 0.10	pade32	[0.0,2.5]	21	1.60	284.18 ± 0.13
pade32	[0.0,3.0]	28	1.50	238.59 ± 0.19	pade32	[0.0,3.0]	28	1.52	285.01 ± 0.23
pade32	[0.0,3.5]	35	1.67	237.59 ± 0.11	pade32	[0.0,3.5]	35	1.70	283.61 ± 0.13
pade32	[0.0,4.0]	42	1.62	236.88 ± 0.10	pade32	[0.0,4.0]	42	1.71	288.85 ± 0.14
pade32	[0.0,4.5]	48	1.49	245.73 ± 0.12	pade32	[0.0,4.5]	48	1.51	292.77 ± 0.14
pade32	[0.0,5.0]	53	1.44	250.98 ± 0.12	pade32	[0.0,5.0]	53	1.46	299.29 ± 0.14
pade32	[0.0,5.5]	58	1.52	245.54 ± 0.11	pade32	[0.0,5.5]	58	1.54	292.63 ± 0.13
pade33	[0.0,2.5]	20	1.68	238.22 ± 0.19	pade33	[0.0,2.5]	20	1.70	289.19 ± 0.59
pade33	[0.0,3.0]	27	1.57	252.39 ± 0.27	pade33	[0.0,3.0]	27	1.61	280.93 ± 0.83
pade33	[0.0,3.5]	34	1.76	237.63 ± 0.11	pade33	[0.0,3.5]	34	1.78	283.61 ± 0.13
pade33	[0.0,4.0]	41	1.70	236.89 ± 0.10	pade33	[0.0,4.0]	41	1.80	288.85 ± 0.14
pade33	[0.0,4.5]	47	1.56	245.73 ± 0.12	pade33	[0.0,4.5]	47	1.59	292.79 ± 0.14
pade33	[0.0,5.0]	52	1.51	250.99 ± 0.12	pade33	[0.0,5.0]	52	1.53	299.29 ± 0.14
pade33	[0.0,5.5]	57	1.60	245.54 ± 0.11	pade33	[0.0,5.5]	57	1.62	292.99 ± 0.13
pade43	[0.0,2.5]	19	1.80	238.62 ± 0.33	pade43	[0.0,2.5]	19	1.81	284.86 ± 0.43
pade43	[0.0,3.0]	26	1.68	232.37 ± 0.25	pade43	[0.0,3.0]	26	1.69	301.57 ± 0.32
pade43	[0.0,3.5]	33	1.85	247.12 ± 0.23	pade43	[0.0,3.5]	33	1.87	295.57 ± 0.28
pade43	[0.0,4.0]	40	1.79	236.74 ± 0.10	pade43	[0.0,4.0]	40	1.90	288.85 ± 0.14
pade43	[0.0,4.5]	46	1.64	245.69 ± 0.12	pade43	[0.0,4.5]	46	1.67	292.74 ± 0.14
pade43	[0.0,5.0]	51	1.59	250.92 ± 0.12	pade43	[0.0,5.0]	51	1.60	298.71 ± 0.14
pade43	[0.0,5.5]	56	1.68	245.86 ± 0.11	pade43	[0.0,5.5]	56	1.70	292.52 ± 0.13
pade42	[0.0,2.5]	20	1.68	238.28 ± 0.10	pade42	[0.0,2.5]	20	1.70	284.14 ± 0.13
pade42	[0.0,3.0]	27	1.58	238.58 ± 0.20	pade42	[0.0,3.0]	27	1.60	285.00 ± 0.23
pade42	[0.0,3.5]	34	1.76	237.55 ± 0.11	pade42	[0.0,3.5]	34	1.78	283.59 ± 0.13
pade42	[0.0,4.0]	41	1.70	236.87 ± 0.10	pade42	[0.0,4.0]	41	1.80	288.78 ± 0.14
pade42	[0.0,4.5]	47	1.56	245.69 ± 0.12	pade42	[0.0,4.5]	47	1.58	292.74 ± 0.14
pade42	[0.0,5.0]	52	1.51	250.91 ± 0.12	pade42	[0.0,5.0]	52	1.53	299.21 ± 0.14
pade42	[0.0,5.5]	57	1.60	245.44 ± 0.11	pade42	[0.0,5.5]	57	1.62	292.52 ± 0.13
disp	[0.0,2.5]	22	1.50	237.65 ± 0.22	disp	[0.0,2.5]	22	1.51	283.76 ± 0.28
disp	[0.0,3.0]	29	1.42	246.19 ± 0.29	disp	[0.0,3.0]	29	1.44	294.31 ± 0.34
disp	[0.0,3.5]	36	1.60	238.74 ± 0.12	disp	[0.0,3.5]	36	1.62	285.06 ± 0.14
disp	[0.0,4.0]	43	1.54	238.01 ± 0.12	disp	[0.0,4.0]	43	1.63	290.45 ± 0.17
disp	[0.0,4.5]	49	1.44	245.23 ± 0.10	disp	[0.0,4.5]	49	1.46	292.32 ± 0.12
disp	[0.0,5.0]	54	1.43	255.41 ± 0.37	disp	[0.0,5.0]	54	1.44	295.72 ± 0.51
disp	[0.0,5.5]	59	1.47	248.74 ± 0.12	disp	[0.0,5.5]	59	1.49	295.27 ± 0.13

Figure 36: Results for different fits on D3 ensemble

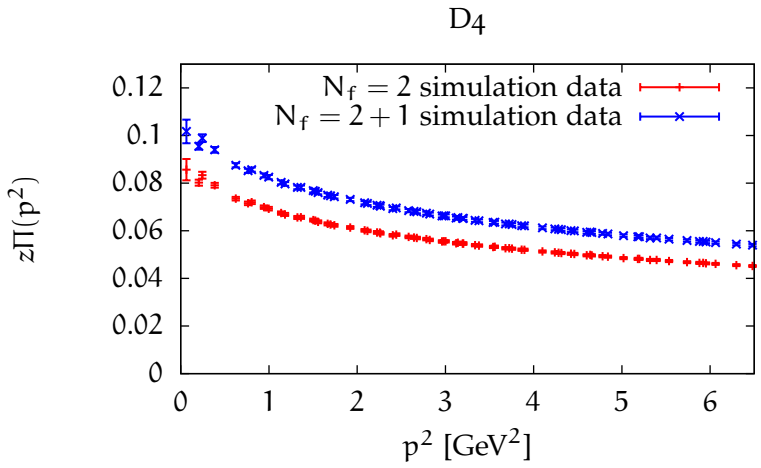

$N_f = 2$					$N_f = 2+1$ partially quenched				
function	interval	N	χ^2_{red}	$a_\mu/10^{-10}$	function	interval	N	χ^2_{red}	$a_\mu/10^{-10}$
pade32	[0.0,2.5]	21	1.79	233.51 ± 0.11	pade32	[0.0,2.5]	21	1.84	272.99 ± 0.12
pade32	[0.0,3.0]	28	1.93	251.73 ± 0.10	pade32	[0.0,3.0]	28	1.61	275.03 ± 0.12
pade32	[0.0,3.5]	35	1.71	256.03 ± 0.10	pade32	[0.0,3.5]	35	1.75	295.76 ± 0.11
pade32	[0.0,4.0]	42	1.59	241.88 ± 0.08	pade32	[0.0,4.0]	42	1.65	279.83 ± 0.09
pade32	[0.0,4.5]	48	1.78	241.97 ± 0.10	pade32	[0.0,4.5]	48	1.84	278.02 ± 0.11
pade32	[0.0,5.0]	53	1.84	234.61 ± 0.10	pade32	[0.0,5.0]	53	1.87	269.72 ± 0.09
pade32	[0.0,5.5]	58	1.76	231.16 ± 0.06	pade32	[0.0,5.5]	58	1.79	268.92 ± 0.07
pade33	[0.0,2.5]	20	1.89	233.27 ± 0.11	pade33	[0.0,2.5]	20	1.94	272.69 ± 0.12
pade33	[0.0,3.0]	27	1.98	251.04 ± 0.10	pade33	[0.0,3.0]	27	1.68	274.07 ± 0.11
pade33	[0.0,3.5]	34	1.73	253.95 ± 0.10	pade33	[0.0,3.5]	34	1.78	293.43 ± 0.10
pade33	[0.0,4.0]	41	1.65	237.86 ± 0.07	pade33	[0.0,4.0]	41	1.71	275.39 ± 0.08
pade33	[0.0,4.5]	47	1.86	241.96 ± 0.10	pade33	[0.0,4.5]	47	1.92	278.01 ± 0.11
pade33	[0.0,5.0]	52	1.92	234.52 ± 0.10	pade33	[0.0,5.0]	52	1.95	271.83 ± 0.10
pade33	[0.0,5.5]	57	1.83	225.80 ± 0.07	pade33	[0.0,5.5]	57	1.86	263.05 ± 0.08
pade43	[0.0,2.5]	19	2.63	188.02 ± 0.04	pade43	[0.0,2.5]	19	2.06	272.69 ± 0.12
pade43	[0.0,3.0]	26	1.98	246.11 ± 0.09	pade43	[0.0,3.0]	26	1.77	274.07 ± 0.11
pade43	[0.0,3.5]	33	1.82	253.95 ± 0.10	pade43	[0.0,3.5]	33	1.87	293.43 ± 0.10
pade43	[0.0,4.0]	40	1.72	237.87 ± 0.07	pade43	[0.0,4.0]	40	1.79	275.39 ± 0.08
pade43	[0.0,4.5]	46	1.94	242.48 ± 0.10	pade43	[0.0,4.5]	46	2.01	278.19 ± 0.11
pade43	[0.0,5.0]	51	2.00	234.63 ± 0.10	pade43	[0.0,5.0]	51	2.04	271.84 ± 0.10
pade43	[0.0,5.5]	56	1.91	225.88 ± 0.07	pade43	[0.0,5.5]	56	1.95	268.92 ± 0.07
pade42	[0.0,2.5]	20	1.90	233.51 ± 0.11	pade42	[0.0,2.5]	20	1.95	272.99 ± 0.12
pade42	[0.0,3.0]	27	2.03	251.73 ± 0.10	pade42	[0.0,3.0]	27	1.69	275.04 ± 0.12
pade42	[0.0,3.5]	34	1.79	256.03 ± 0.10	pade42	[0.0,3.5]	34	1.83	295.76 ± 0.11
pade42	[0.0,4.0]	41	1.66	241.88 ± 0.08	pade42	[0.0,4.0]	41	1.73	279.84 ± 0.09
pade42	[0.0,4.5]	47	1.86	242.15 ± 0.10	pade42	[0.0,4.5]	47	1.92	278.20 ± 0.11
pade42	[0.0,5.0]	52	1.92	234.64 ± 0.10	pade42	[0.0,5.0]	52	1.95	271.86 ± 0.10
pade42	[0.0,5.5]	57	1.84	231.16 ± 0.06	pade42	[0.0,5.5]	57	1.86	268.93 ± 0.07
disp	[0.0,2.5]	22	1.68	232.48 ± 0.10	disp	[0.0,2.5]	22	1.72	271.70 ± 0.11
disp	[0.0,3.0]	29	1.70	248.42 ± 0.09	disp	[0.0,3.0]	29	1.50	271.63 ± 0.11
disp	[0.0,3.5]	36	1.49	248.25 ± 0.09	disp	[0.0,3.5]	36	1.53	287.10 ± 0.09
disp	[0.0,4.0]	43	1.50	230.13 ± 0.07	disp	[0.0,4.0]	43	1.56	267.97 ± 0.09
disp	[0.0,4.5]	49	1.72	238.15 ± 0.09	disp	[0.0,4.5]	49	1.78	274.07 ± 0.09
disp	[0.0,5.0]	54	1.77	233.12 ± 0.09	disp	[0.0,5.0]	54	1.80	270.53 ± 0.10
disp	[0.0,5.5]	59	1.68	224.63 ± 0.10	disp	[0.0,5.5]	59	1.71	262.39 ± 0.11

Figure 37: Results for different fits on D4 ensemble

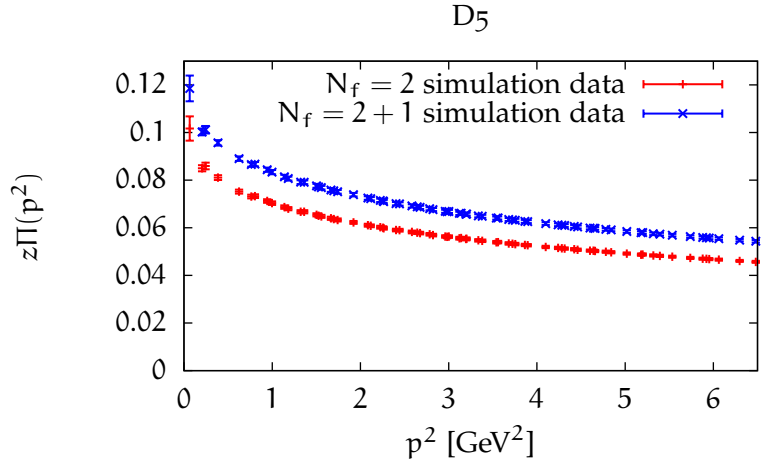

$N_f = 2$					$N_f = 2+1$ partially quenched				
function	interval	N	χ^2_{red}	$a_\mu/10^{-10}$	function	interval	N	χ^2_{red}	$a_\mu/10^{-10}$
pade32	[0.0,2.5]	21	1.67	285.07 ± 0.15	pade32	[0.0,2.5]	21	1.67	319.31 ± 0.15
pade32	[0.0,3.0]	28	1.50	282.37 ± 0.21	pade32	[0.0,3.0]	28	1.51	317.93 ± 0.21
pade32	[0.0,3.5]	35	1.46	287.74 ± 0.26	pade32	[0.0,3.5]	35	1.48	323.72 ± 0.26
pade32	[0.0,4.0]	42	1.37	301.72 ± 0.30	pade32	[0.0,4.0]	42	1.39	334.75 ± 0.28
pade32	[0.0,4.5]	48	1.40	258.26 ± 0.10	pade32	[0.0,4.5]	48	1.42	292.92 ± 0.10
pade32	[0.0,5.0]	53	1.44	266.99 ± 0.15	pade32	[0.0,5.0]	53	1.45	303.19 ± 0.15
pade32	[0.0,5.5]	58	1.39	261.13 ± 0.13	pade32	[0.0,5.5]	58	1.40	295.76 ± 0.13
pade33	[0.0,2.5]	20	1.76	285.07 ± 0.15	pade33	[0.0,2.5]	20	1.76	318.19 ± 0.15
pade33	[0.0,3.0]	27	1.58	277.86 ± 0.20	pade33	[0.0,3.0]	27	1.59	317.30 ± 0.24
pade33	[0.0,3.5]	34	1.53	287.75 ± 0.26	pade33	[0.0,3.5]	34	1.55	324.13 ± 0.27
pade33	[0.0,4.0]	41	1.43	301.75 ± 0.30	pade33	[0.0,4.0]	41	1.45	334.85 ± 0.28
pade33	[0.0,4.5]	47	1.46	258.07 ± 0.09	pade33	[0.0,4.5]	47	1.48	292.68 ± 0.09
pade33	[0.0,5.0]	52	1.50	267.13 ± 0.15	pade33	[0.0,5.0]	52	1.51	303.35 ± 0.15
pade33	[0.0,5.5]	57	1.44	261.18 ± 0.13	pade33	[0.0,5.5]	57	1.46	295.76 ± 0.13
pade43	[0.0,2.5]	19	1.85	283.35 ± 0.15	pade43	[0.0,2.5]	19	1.85	317.55 ± 0.15
pade43	[0.0,3.0]	26	1.65	282.35 ± 0.21	pade43	[0.0,3.0]	26	1.67	317.90 ± 0.21
pade43	[0.0,3.5]	33	1.60	287.66 ± 0.26	pade43	[0.0,3.5]	33	1.65	301.12 ± 0.12
pade43	[0.0,4.0]	40	1.50	301.67 ± 0.30	pade43	[0.0,4.0]	40	1.51	334.69 ± 0.28
pade43	[0.0,4.5]	46	1.53	258.32 ± 0.10	pade43	[0.0,4.5]	46	1.55	292.64 ± 0.09
pade43	[0.0,5.0]	51	1.56	266.97 ± 0.15	pade43	[0.0,5.0]	51	1.58	303.14 ± 0.15
pade43	[0.0,5.5]	56	1.50	261.13 ± 0.13	pade43	[0.0,5.5]	56	1.52	295.70 ± 0.13
pade42	[0.0,2.5]	20	1.76	285.07 ± 0.15	pade42	[0.0,2.5]	20	1.76	319.31 ± 0.15
pade42	[0.0,3.0]	27	1.57	282.38 ± 0.21	pade42	[0.0,3.0]	27	1.59	317.93 ± 0.20
pade42	[0.0,3.5]	34	1.53	287.64 ± 0.26	pade42	[0.0,3.5]	34	1.55	323.62 ± 0.25
pade42	[0.0,4.0]	41	1.43	301.66 ± 0.30	pade42	[0.0,4.0]	41	1.45	334.69 ± 0.28
pade42	[0.0,4.5]	47	1.46	258.29 ± 0.10	pade42	[0.0,4.5]	47	1.48	292.94 ± 0.10
pade42	[0.0,5.0]	52	1.50	266.95 ± 0.15	pade42	[0.0,5.0]	52	1.51	303.14 ± 0.15
pade42	[0.0,5.5]	57	1.44	261.11 ± 0.13	pade42	[0.0,5.5]	57	1.46	295.70 ± 0.13
disp	[0.0,2.5]	22	1.53	279.80 ± 0.14	disp	[0.0,2.5]	22	1.53	313.90 ± 0.14
disp	[0.0,3.0]	29	1.44	282.34 ± 0.23	disp	[0.0,3.0]	29	1.45	317.78 ± 0.22
disp	[0.0,3.5]	36	1.39	335.32 ± 0.69	disp	[0.0,3.5]	36	1.42	366.36 ± 0.58
disp	[0.0,4.0]	43	1.30	365.30 ± 0.80	disp	[0.0,4.0]	43	1.32	387.46 ± 0.62
disp	[0.0,4.5]	49	1.35	259.43 ± 0.16	disp	[0.0,4.5]	49	1.37	293.90 ± 0.16
disp	[0.0,5.0]	54	1.38	271.39 ± 0.19	disp	[0.0,5.0]	54	1.39	307.52 ± 0.19
disp	[0.0,5.5]	59	1.33	263.31 ± 0.15	disp	[0.0,5.5]	59	1.35	297.88 ± 0.15

Figure 38: Results for different fits on D5 ensemble

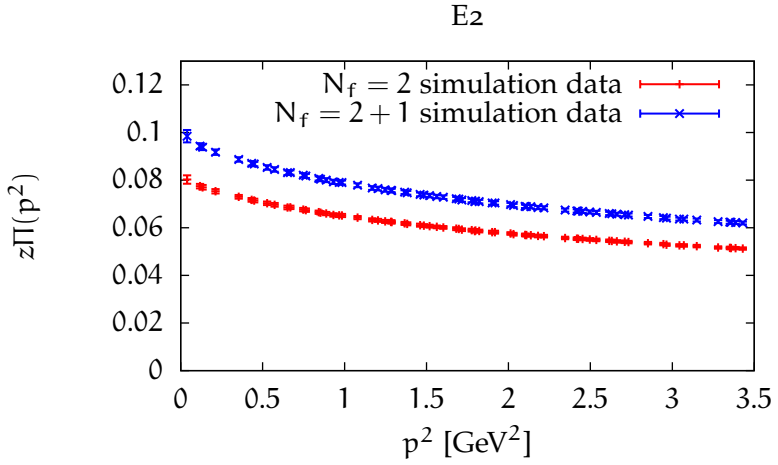

$N_f = 2$					$N_f = 2+1$ partially quenched				
function	interval	N	χ^2_{red}	$a_\mu/10^{-10}$	function	interval	N	χ^2_{red}	$a_\mu/10^{-10}$
pade32	[0.0,1.8]	32	0.87	178.91 ± 0.04	pade32	[0.0,1.8]	32	0.98	225.09 ± 0.07
pade32	[0.0,2.0]	35	0.87	177.46 ± 0.04	pade32	[0.0,2.0]	35	1.07	223.78 ± 0.09
pade32	[0.0,2.2]	41	0.83	177.69 ± 0.05	pade32	[0.0,2.2]	41	0.98	224.88 ± 0.09
pade32	[0.0,2.5]	47	0.80	177.26 ± 0.03	pade32	[0.0,2.5]	47	0.99	220.00 ± 0.09
pade32	[0.0,2.8]	53	0.80	176.47 ± 0.03	pade32	[0.0,2.8]	53	0.79	221.62 ± 0.06
pade32	[0.0,3.0]	56	0.79	178.76 ± 0.05	pade32	[0.0,3.0]	56	0.81	222.12 ± 0.08
pade32	[0.0,3.5]	64	0.75	176.18 ± 0.04	pade32	[0.0,3.5]	64	0.77	221.22 ± 0.06
pade33	[0.0,1.8]	31	0.93	178.72 ± 0.04	pade33	[0.0,1.8]	31	1.04	224.76 ± 0.07
pade33	[0.0,2.0]	34	0.94	177.12 ± 0.04	pade33	[0.0,2.0]	34	1.15	217.64 ± 0.06
pade33	[0.0,2.2]	40	0.89	176.58 ± 0.03	pade33	[0.0,2.2]	40	1.04	224.49 ± 0.09
pade33	[0.0,2.5]	46	0.85	177.25 ± 0.03	pade33	[0.0,2.5]	46	1.05	219.88 ± 0.08
pade33	[0.0,2.8]	52	0.78	133.82 ± 0.32	pade33	[0.0,2.8]	52	0.84	221.63 ± 0.06
pade33	[0.0,3.0]	55	0.85	178.67 ± 0.04	pade33	[0.0,3.0]	55	0.86	222.08 ± 0.08
pade33	[0.0,3.5]	63	0.80	176.14 ± 0.04	pade33	[0.0,3.5]	63	0.81	220.38 ± 0.06
pade43	[0.0,1.8]	30	1.01	178.72 ± 0.04	pade43	[0.0,1.8]	30	1.11	224.77 ± 0.07
pade43	[0.0,2.0]	33	1.02	177.11 ± 0.04	pade43	[0.0,2.0]	33	1.21	223.88 ± 0.09
pade43	[0.0,2.2]	39	0.96	177.69 ± 0.05	pade43	[0.0,2.2]	39	1.11	224.96 ± 0.09
pade43	[0.0,2.5]	45	0.92	176.87 ± 0.03	pade43	[0.0,2.5]	45	1.12	220.23 ± 0.09
pade43	[0.0,2.8]	51	0.91	177.94 ± 0.04	pade43	[0.0,2.8]	51	0.89	221.32 ± 0.06
pade43	[0.0,3.0]	54	0.91	178.76 ± 0.05	pade43	[0.0,3.0]	54	0.91	222.12 ± 0.08
pade43	[0.0,3.5]	62	0.86	176.16 ± 0.04	pade43	[0.0,3.5]	62	0.86	221.22 ± 0.07
pade42	[0.0,1.8]	31	0.94	178.91 ± 0.04	pade42	[0.0,1.8]	31	1.04	225.09 ± 0.07
pade42	[0.0,2.0]	34	0.94	177.47 ± 0.04	pade42	[0.0,2.0]	34	1.14	223.88 ± 0.09
pade42	[0.0,2.2]	40	0.89	177.70 ± 0.05	pade42	[0.0,2.2]	40	1.04	224.96 ± 0.09
pade42	[0.0,2.5]	46	0.85	177.27 ± 0.03	pade42	[0.0,2.5]	46	1.05	219.92 ± 0.09
pade42	[0.0,2.8]	52	0.85	177.94 ± 0.04	pade42	[0.0,2.8]	52	0.84	221.62 ± 0.05
pade42	[0.0,3.0]	55	0.85	178.78 ± 0.05	pade42	[0.0,3.0]	55	0.86	222.13 ± 0.08
pade42	[0.0,3.5]	63	0.80	176.19 ± 0.04	pade42	[0.0,3.5]	63	0.81	221.23 ± 0.06
disp	[0.0,1.8]	33	0.79	178.30 ± 0.04	disp	[0.0,1.8]	33	0.91	224.01 ± 0.06
disp	[0.0,2.0]	36	0.81	176.42 ± 0.03	disp	[0.0,2.0]	36	1.02	220.71 ± 0.09
disp	[0.0,2.2]	42	0.78	177.53 ± 0.05	disp	[0.0,2.2]	42	0.94	223.26 ± 0.24
disp	[0.0,2.5]	48	0.74	176.43 ± 0.04	disp	[0.0,2.5]	48	0.94	219.91 ± 0.07
disp	[0.0,2.8]	54	0.75	177.71 ± 0.05	disp	[0.0,2.8]	54	0.75	221.33 ± 0.07
disp	[0.0,3.0]	57	0.75	178.29 ± 0.04	disp	[0.0,3.0]	57	0.77	221.95 ± 0.07
disp	[0.0,3.5]	65	0.70	176.11 ± 0.04	disp	[0.0,3.5]	65	0.73	221.01 ± 0.06

Figure 39: Results for different fits on E2 ensemble

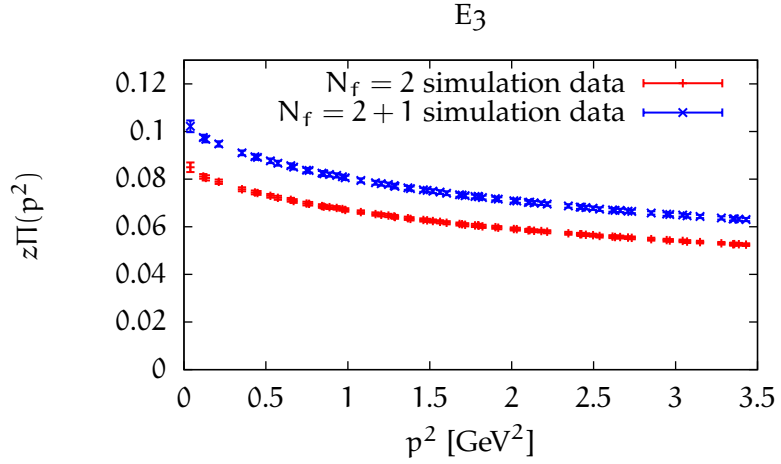

$N_f = 2$					$N_f = 2+1$ partially quenched				
function	interval	N	χ^2_{red}	$a_\mu/10^{-10}$	function	interval	N	χ^2_{red}	$a_\mu/10^{-10}$
pade32	[0.0,1.8]	32	1.42	186.33 ± 0.05	pade32	[0.0,1.8]	32	1.42	224.18 ± 0.06
pade32	[0.0,2.0]	35	1.53	192.69 ± 0.04	pade32	[0.0,2.0]	35	1.53	231.99 ± 0.05
pade32	[0.0,2.2]	41	1.42	194.87 ± 0.04	pade32	[0.0,2.2]	41	1.42	234.63 ± 0.05
pade32	[0.0,2.5]	47	1.02	196.30 ± 0.06	pade32	[0.0,2.5]	47	1.00	236.42 ± 0.08
pade32	[0.0,2.8]	53	1.17	193.85 ± 0.04	pade32	[0.0,2.8]	53	1.16	233.24 ± 0.04
pade32	[0.0,3.0]	56	1.35	197.64 ± 0.04	pade32	[0.0,3.0]	56	1.35	238.02 ± 0.04
pade32	[0.0,3.5]	64	1.39	199.53 ± 0.03	pade32	[0.0,3.5]	64	1.39	240.31 ± 0.04
pade33	[0.0,1.8]	31	1.51	186.35 ± 0.05	pade33	[0.0,1.8]	31	1.51	224.23 ± 0.05
pade33	[0.0,2.0]	34	1.43	153.49 ± 0.19	pade33	[0.0,2.0]	34	1.60	231.34 ± 0.05
pade33	[0.0,2.2]	40	1.48	193.77 ± 0.04	pade33	[0.0,2.2]	40	1.50	234.53 ± 0.05
pade33	[0.0,2.5]	46	1.09	196.28 ± 0.06	pade33	[0.0,2.5]	46	1.06	236.41 ± 0.08
pade33	[0.0,2.8]	52	1.24	193.82 ± 0.04	pade33	[0.0,2.8]	52	1.23	233.19 ± 0.04
pade33	[0.0,3.0]	55	1.41	197.20 ± 0.03	pade33	[0.0,3.0]	55	1.41	237.49 ± 0.04
pade33	[0.0,3.5]	63	1.44	198.94 ± 0.03	pade33	[0.0,3.5]	63	1.44	239.60 ± 0.04
pade43	[0.0,1.8]	30	1.61	186.33 ± 0.05	pade43	[0.0,1.8]	30	1.61	224.19 ± 0.06
pade43	[0.0,2.0]	33	1.73	192.73 ± 0.04	pade43	[0.0,2.0]	33	1.73	232.04 ± 0.05
pade43	[0.0,2.2]	39	1.61	194.79 ± 0.04	pade43	[0.0,2.2]	39	1.61	234.53 ± 0.05
pade43	[0.0,2.5]	45	1.16	196.69 ± 0.06	pade43	[0.0,2.5]	45	1.13	236.93 ± 0.08
pade43	[0.0,2.8]	51	1.32	193.69 ± 0.04	pade43	[0.0,2.8]	51	1.31	233.19 ± 0.04
pade43	[0.0,3.0]	54	1.50	197.20 ± 0.03	pade43	[0.0,3.0]	54	1.50	237.49 ± 0.04
pade43	[0.0,3.5]	62	1.53	198.94 ± 0.03	pade43	[0.0,3.5]	62	1.53	239.60 ± 0.04
pade42	[0.0,1.8]	31	1.51	186.33 ± 0.05	pade42	[0.0,1.8]	31	1.51	224.18 ± 0.06
pade42	[0.0,2.0]	34	1.62	192.69 ± 0.04	pade42	[0.0,2.0]	34	1.62	231.99 ± 0.05
pade42	[0.0,2.2]	40	1.51	194.87 ± 0.04	pade42	[0.0,2.2]	40	1.51	234.63 ± 0.05
pade42	[0.0,2.5]	46	1.08	196.69 ± 0.06	pade42	[0.0,2.5]	46	1.06	236.93 ± 0.08
pade42	[0.0,2.8]	52	1.24	193.88 ± 0.04	pade42	[0.0,2.8]	52	1.23	233.26 ± 0.04
pade42	[0.0,3.0]	55	1.43	197.64 ± 0.04	pade42	[0.0,3.0]	55	1.43	238.02 ± 0.04
pade42	[0.0,3.5]	63	1.47	199.53 ± 0.03	pade42	[0.0,3.5]	63	1.47	240.31 ± 0.04
disp	[0.0,1.8]	33	1.34	186.35 ± 0.05	disp	[0.0,1.8]	33	1.34	224.23 ± 0.05
disp	[0.0,2.0]	36	1.44	192.82 ± 0.04	disp	[0.0,2.0]	36	1.44	232.16 ± 0.05
disp	[0.0,2.2]	42	1.33	194.57 ± 0.04	disp	[0.0,2.2]	42	1.33	234.28 ± 0.05
disp	[0.0,2.5]	48	0.98	192.91 ± 0.09	disp	[0.0,2.5]	48	0.96	232.67 ± 0.12
disp	[0.0,2.8]	54	1.10	193.40 ± 0.04	disp	[0.0,2.8]	54	1.09	232.75 ± 0.05
disp	[0.0,3.0]	57	1.24	196.19 ± 0.03	disp	[0.0,3.0]	57	1.24	236.28 ± 0.04
disp	[0.0,3.5]	65	1.23	197.65 ± 0.03	disp	[0.0,3.5]	65	1.23	238.03 ± 0.04

Figure 40: Results for different fits on E3 ensemble

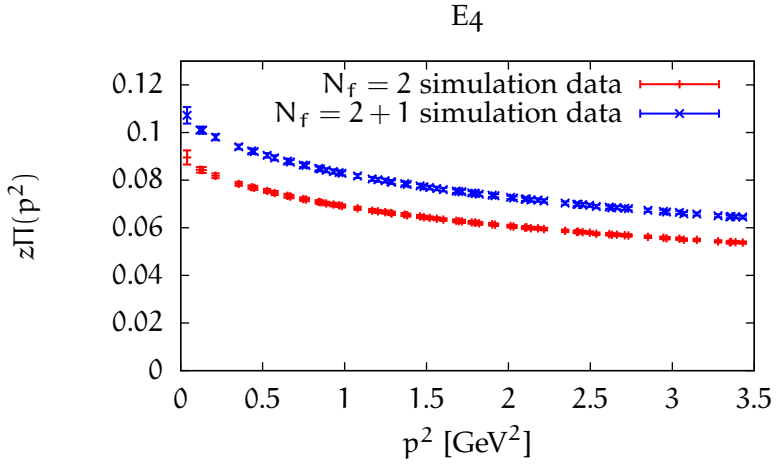

$N_f = 2$					$N_f = 2+1$ partially quenched				
function	interval	N	χ^2_{red}	$a_\mu/10^{-10}$	function	interval	N	χ^2_{red}	$a_\mu/10^{-10}$
pade32	[0.0,1.8]	32	1.18	245.36 ± 0.08	pade32	[0.0,1.8]	32	1.19	292.70 ± 0.10
pade32	[0.0,2.0]	35	1.21	248.90 ± 0.07	pade32	[0.0,2.0]	35	1.21	295.94 ± 0.09
pade32	[0.0,2.2]	41	1.35	241.69 ± 0.06	pade32	[0.0,2.2]	41	1.35	287.95 ± 0.07
pade32	[0.0,2.5]	47	1.18	239.26 ± 0.07	pade32	[0.0,2.5]	47	1.19	284.66 ± 0.08
pade32	[0.0,2.8]	53	1.11	245.73 ± 0.06	pade32	[0.0,2.8]	53	1.08	288.23 ± 0.07
pade32	[0.0,3.0]	56	1.06	242.22 ± 0.09	pade32	[0.0,3.0]	56	1.08	288.40 ± 0.10
pade32	[0.0,3.5]	64	1.08	246.92 ± 0.09	pade32	[0.0,3.5]	64	1.09	293.76 ± 0.10
pade33	[0.0,1.8]	31	1.24	244.95 ± 0.08	pade33	[0.0,1.8]	31	1.26	292.13 ± 0.09
pade33	[0.0,2.0]	34	1.26	247.99 ± 0.07	pade33	[0.0,2.0]	34	1.27	294.86 ± 0.08
pade33	[0.0,2.2]	40	1.42	240.25 ± 0.06	pade33	[0.0,2.2]	40	1.42	287.95 ± 0.07
pade33	[0.0,2.5]	46	1.24	237.81 ± 0.10	pade33	[0.0,2.5]	46	1.26	284.18 ± 0.11
pade33	[0.0,2.8]	52	1.16	243.94 ± 0.06	pade33	[0.0,2.8]	52	1.13	286.41 ± 0.07
pade33	[0.0,3.0]	55	1.12	242.16 ± 0.09	pade33	[0.0,3.0]	55	1.14	288.34 ± 0.10
pade33	[0.0,3.5]	63	1.14	246.92 ± 0.09	pade33	[0.0,3.5]	63	1.15	293.55 ± 0.10
pade43	[0.0,1.8]	30	1.30	242.85 ± 0.07	pade43	[0.0,1.8]	30	1.33	289.52 ± 0.09
pade43	[0.0,2.0]	33	1.34	247.99 ± 0.07	pade43	[0.0,2.0]	33	1.35	294.86 ± 0.08
pade43	[0.0,2.2]	39	1.50	240.26 ± 0.06	pade43	[0.0,2.2]	39	1.50	286.26 ± 0.07
pade43	[0.0,2.5]	45	1.32	238.80 ± 0.09	pade43	[0.0,2.5]	45	1.34	284.24 ± 0.10
pade43	[0.0,2.8]	51	1.22	243.95 ± 0.06	pade43	[0.0,2.8]	51	1.20	286.41 ± 0.07
pade43	[0.0,3.0]	54	1.19	242.22 ± 0.09	pade43	[0.0,3.0]	54	1.21	288.41 ± 0.10
pade43	[0.0,3.5]	62	1.21	246.96 ± 0.09	pade43	[0.0,3.5]	62	1.22	293.80 ± 0.10
pade42	[0.0,1.8]	31	1.25	245.36 ± 0.08	pade42	[0.0,1.8]	31	1.27	292.71 ± 0.10
pade42	[0.0,2.0]	34	1.28	248.91 ± 0.07	pade42	[0.0,2.0]	34	1.28	295.94 ± 0.09
pade42	[0.0,2.2]	40	1.42	241.70 ± 0.06	pade42	[0.0,2.2]	40	1.42	287.96 ± 0.07
pade42	[0.0,2.5]	46	1.24	239.29 ± 0.07	pade42	[0.0,2.5]	46	1.26	284.67 ± 0.08
pade42	[0.0,2.8]	52	1.17	245.73 ± 0.06	pade42	[0.0,2.8]	52	1.14	288.24 ± 0.07
pade42	[0.0,3.0]	55	1.12	242.23 ± 0.09	pade42	[0.0,3.0]	55	1.14	288.42 ± 0.10
pade42	[0.0,3.5]	63	1.14	246.96 ± 0.09	pade42	[0.0,3.5]	63	1.15	293.80 ± 0.10
disp	[0.0,1.8]	33	1.10	244.05 ± 0.08	disp	[0.0,1.8]	33	1.11	290.88 ± 0.09
disp	[0.0,2.0]	36	1.10	245.81 ± 0.07	disp	[0.0,2.0]	36	1.11	292.28 ± 0.08
disp	[0.0,2.2]	42	1.27	237.61 ± 0.06	disp	[0.0,2.2]	42	1.27	283.05 ± 0.07
disp	[0.0,2.5]	48	1.12	238.63 ± 0.10	disp	[0.0,2.5]	48	1.14	284.06 ± 0.11
disp	[0.0,2.8]	54	1.02	240.29 ± 0.05	disp	[0.0,2.8]	54	1.01	282.62 ± 0.06
disp	[0.0,3.0]	57	1.01	242.03 ± 0.09	disp	[0.0,3.0]	57	1.03	288.18 ± 0.10
disp	[0.0,3.5]	65	1.05	248.70 ± 0.27	disp	[0.0,3.5]	65	1.05	293.33 ± 0.11

Figure 41: Results for different fits on E4 ensemble

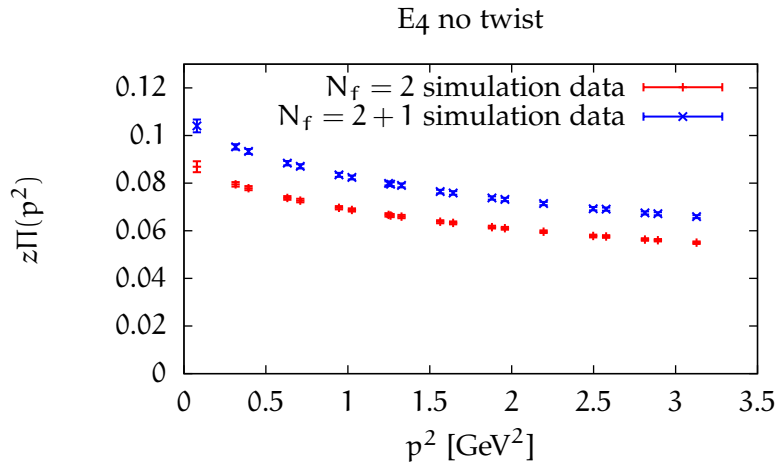

$N_f = 2$					$N_f = 2+1$ partially quenched				
function	interval	N	χ^2_{red}	$a_\mu/10^{-10}$	function	interval	N	χ^2_{red}	$a_\mu/10^{-10}$
pade32	[0.0,1.8]	6	0.96	232.08 ± 0.12	pade32	[0.0,1.8]	6	0.98	276.82 ± 0.14
pade32	[0.0,2.0]	8	1.06	217.88 ± 0.08	pade32	[0.0,2.0]	8	1.08	259.89 ± 0.10
pade32	[0.0,2.2]	9	0.92	217.95 ± 0.07	pade32	[0.0,2.2]	9	0.94	259.80 ± 0.09
pade32	[0.0,2.5]	10	0.92	228.37 ± 0.07	pade32	[0.0,2.5]	10	1.05	278.10 ± 0.11
pade32	[0.0,2.8]	11	1.08	226.92 ± 0.07	pade32	[0.0,2.8]	11	1.25	266.83 ± 0.09
pade32	[0.0,3.0]	13	1.08	231.15 ± 0.15	pade32	[0.0,3.0]	13	1.09	276.00 ± 0.18
pade32	[0.0,3.5]	14	1.08	232.40 ± 0.14	pade32	[0.0,3.5]	14	1.09	277.28 ± 0.17
pade33	[0.0,1.8]	5	1.21	232.08 ± 0.12	pade33	[0.0,1.8]	5	1.22	276.82 ± 0.14
pade33	[0.0,2.0]	7	1.27	217.88 ± 0.08	pade33	[0.0,2.0]	7	1.30	259.89 ± 0.10
pade33	[0.0,2.2]	8	1.10	217.95 ± 0.07	pade33	[0.0,2.2]	8	1.12	259.80 ± 0.09
pade33	[0.0,2.5]	9	1.07	228.37 ± 0.07	pade33	[0.0,2.5]	9	1.21	277.29 ± 0.11
pade33	[0.0,2.8]	10	1.25	226.85 ± 0.07	pade33	[0.0,2.8]	10	1.49	266.00 ± 0.09
pade33	[0.0,3.0]	12	1.27	225.95 ± 0.20	pade33	[0.0,3.0]	12	1.27	275.81 ± 0.18
pade33	[0.0,3.5]	13	1.26	232.30 ± 0.15	pade33	[0.0,3.5]	13	1.27	277.16 ± 0.17
pade43	[0.0,1.8]	4	1.61	232.08 ± 0.12	pade43	[0.0,1.8]	4	1.63	276.81 ± 0.14
pade43	[0.0,2.0]	6	1.59	217.88 ± 0.08	pade43	[0.0,2.0]	6	1.62	259.89 ± 0.10
pade43	[0.0,2.2]	7	1.37	217.94 ± 0.07	pade43	[0.0,2.2]	7	-	–
pade43	[0.0,2.5]	8	1.25	227.00 ± 0.06	pade43	[0.0,2.5]	8	1.52	277.29 ± 0.11
pade43	[0.0,2.8]	9	1.49	225.69 ± 0.06	pade43	[0.0,2.8]	9	1.87	266.82 ± 0.09
pade43	[0.0,3.0]	11	1.52	225.31 ± 0.06	pade43	[0.0,3.0]	11	1.53	276.02 ± 0.18
pade43	[0.0,3.5]	12	1.51	232.30 ± 0.15	pade43	[0.0,3.5]	12	1.57	267.20 ± 0.07
pade42	[0.0,1.8]	5	1.21	232.09 ± 0.12	pade42	[0.0,1.8]	5	-	–
pade42	[0.0,2.0]	7	-	–	pade42	[0.0,2.0]	7	-	–
pade42	[0.0,2.2]	8	-	–	pade42	[0.0,2.2]	8	-	–
pade42	[0.0,2.5]	9	1.07	228.37 ± 0.07	pade42	[0.0,2.5]	9	1.27	278.10 ± 0.11
pade42	[0.0,2.8]	10	1.25	226.92 ± 0.07	pade42	[0.0,2.8]	10	1.50	266.83 ± 0.09
pade42	[0.0,3.0]	12	1.26	231.19 ± 0.15	pade42	[0.0,3.0]	12	1.27	276.05 ± 0.18
pade42	[0.0,3.5]	13	1.26	232.43 ± 0.14	pade42	[0.0,3.5]	13	1.27	277.31 ± 0.17
disp	[0.0,1.8]	7	-	–	disp	[0.0,1.8]	7	-	–
disp	[0.0,2.0]	9	-	–	disp	[0.0,2.0]	9	-	–
disp	[0.0,2.2]	10	-	–	disp	[0.0,2.2]	10	-	–
disp	[0.0,2.5]	11	0.74	224.08 ± 0.06	disp	[0.0,2.5]	11	0.79	275.10 ± 0.10
disp	[0.0,2.8]	12	0.91	223.18 ± 0.06	disp	[0.0,2.8]	12	1.05	264.32 ± 0.09
disp	[0.0,3.0]	14	0.95	230.86 ± 0.16	disp	[0.0,3.0]	14	0.96	275.74 ± 0.20
disp	[0.0,3.5]	15	0.95	232.74 ± 0.17	disp	[0.0,3.5]	15	0.96	280.91 ± 0.34

Figure 42: Results for different fits without twisting on E4 ensemble

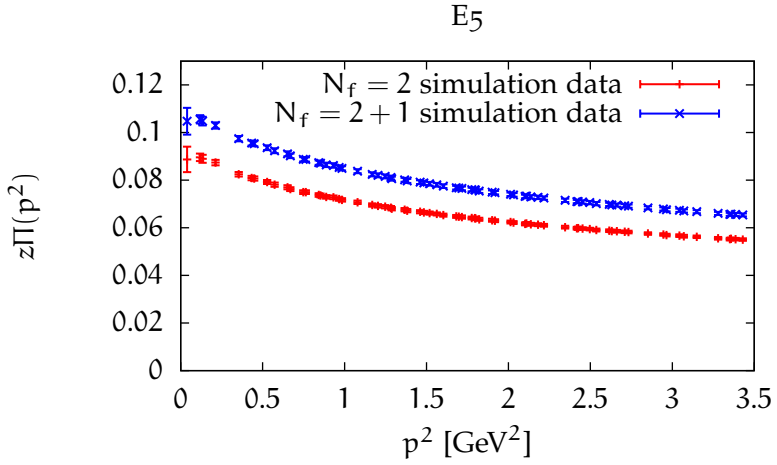

$N_f = 2$					$N_f = 2+1$ partially quenched				
function	interval	N	χ^2_{red}	$a_\mu / 10^{-10}$	function	interval	N	χ^2_{red}	$a_\mu / 10^{-10}$
pade32	[0.0,1.8]	32	0.97	322.86 ± 0.14	pade32	[0.0,1.8]	32	0.95	366.69 ± 0.15
pade32	[0.0,2.0]	35	1.10	330.56 ± 0.28	pade32	[0.0,2.0]	35	1.11	376.29 ± 0.28
pade32	[0.0,2.2]	41	1.03	328.05 ± 0.25	pade32	[0.0,2.2]	41	1.04	366.30 ± 0.24
pade32	[0.0,2.5]	47	1.02	331.64 ± 0.28	pade32	[0.0,2.5]	47	1.02	373.21 ± 0.28
pade32	[0.0,2.8]	53	0.96	316.13 ± 0.21	pade32	[0.0,2.8]	53	1.00	339.30 ± 0.09
pade32	[0.0,3.0]	56	0.90	331.16 ± 0.19	pade32	[0.0,3.0]	56	0.92	370.74 ± 0.20
pade32	[0.0,3.5]	64	0.96	316.08 ± 0.17	pade32	[0.0,3.5]	64	0.96	349.55 ± 0.18
pade33	[0.0,1.8]	31	1.02	322.79 ± 0.15	pade33	[0.0,1.8]	31	0.99	366.70 ± 0.15
pade33	[0.0,2.0]	34	1.15	332.95 ± 0.30	pade33	[0.0,2.0]	34	1.16	376.53 ± 0.29
pade33	[0.0,2.2]	40	1.08	328.28 ± 0.26	pade33	[0.0,2.2]	40	1.09	366.31 ± 0.24
pade33	[0.0,2.5]	46	1.06	331.76 ± 0.28	pade33	[0.0,2.5]	46	1.07	373.21 ± 0.28
pade33	[0.0,2.8]	52	1.00	316.36 ± 0.34	pade33	[0.0,2.8]	52	1.02	357.90 ± 0.40
pade33	[0.0,3.0]	55	0.93	331.16 ± 0.19	pade33	[0.0,3.0]	55	0.96	370.74 ± 0.20
pade33	[0.0,3.5]	63	1.00	330.37 ± 0.35	pade33	[0.0,3.5]	63	1.00	349.69 ± 0.18
pade43	[0.0,1.8]	30	1.07	321.60 ± 0.15	pade43	[0.0,1.8]	30	1.04	365.24 ± 0.16
pade43	[0.0,2.0]	33	1.21	332.96 ± 0.30	pade43	[0.0,2.0]	33	1.21	377.42 ± 0.29
pade43	[0.0,2.2]	39	1.12	328.08 ± 0.26	pade43	[0.0,2.2]	39	1.15	348.36 ± 0.11
pade43	[0.0,2.5]	45	1.11	334.62 ± 0.34	pade43	[0.0,2.5]	45	1.11	373.21 ± 0.28
pade43	[0.0,2.8]	51	1.06	297.99 ± 0.09	pade43	[0.0,2.8]	51	1.09	339.30 ± 0.09
pade43	[0.0,3.0]	54	0.97	331.07 ± 0.19	pade43	[0.0,3.0]	54	1.00	370.64 ± 0.20
pade43	[0.0,3.5]	62	1.06	303.25 ± 0.08	pade43	[0.0,3.5]	62	1.03	388.45 ± 0.56
pade42	[0.0,1.8]	31	1.02	322.89 ± 0.14	pade42	[0.0,1.8]	31	0.99	366.73 ± 0.15
pade42	[0.0,2.0]	34	1.15	330.50 ± 0.28	pade42	[0.0,2.0]	34	1.16	376.37 ± 0.28
pade42	[0.0,2.2]	40	1.08	327.92 ± 0.25	pade42	[0.0,2.2]	40	1.09	366.25 ± 0.24
pade42	[0.0,2.5]	46	1.06	331.58 ± 0.28	pade42	[0.0,2.5]	46	1.07	373.18 ± 0.28
pade42	[0.0,2.8]	52	1.00	316.12 ± 0.21	pade42	[0.0,2.8]	52	1.02	357.59 ± 0.21
pade42	[0.0,3.0]	55	0.93	331.07 ± 0.18	pade42	[0.0,3.0]	55	0.96	370.63 ± 0.20
pade42	[0.0,3.5]	63	1.00	316.01 ± 0.17	pade42	[0.0,3.5]	63	1.00	349.68 ± 0.18
disp	[0.0,1.8]	33	0.93	318.97 ± 0.20	disp	[0.0,1.8]	33	0.90	362.16 ± 0.20
disp	[0.0,2.0]	36	1.06	337.34 ± 0.43	disp	[0.0,2.0]	36	1.06	384.67 ± 0.43
disp	[0.0,2.2]	42	0.99	332.02 ± 0.53	disp	[0.0,2.2]	42	1.00	367.97 ± 0.39
disp	[0.0,2.5]	48	0.98	345.89 ± 0.43	disp	[0.0,2.5]	48	0.98	387.41 ± 0.42
disp	[0.0,2.8]	54	0.92	329.65 ± 0.34	disp	[0.0,2.8]	54	0.94	372.67 ± 0.33
disp	[0.0,3.0]	57	0.88	339.77 ± 0.37	disp	[0.0,3.0]	57	0.90	381.34 ± 0.36
disp	[0.0,3.5]	65	0.93	320.06 ± 0.23	disp	[0.0,3.5]	65	0.92	353.30 ± 0.24

Figure 43: Results for different fits on E5 ensemble

F6

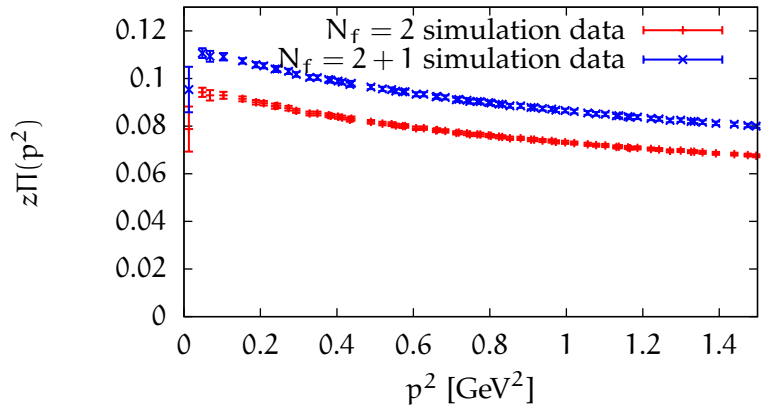

$N_f = 2$					$N_f = 2+1$ partially quenched				
function	interval	N	χ^2_{red}	$a_\mu/10^{-10}$	function	interval	N	χ^2_{red}	$a_\mu/10^{-10}$
pade32	[0.0,0.7]	23	1.51	407.37 ± 0.27	pade32	[0.0,0.7]	23	1.47	435.35 ± 0.24
pade32	[0.0,0.8]	30	1.42	422.50 ± 0.26	pade32	[0.0,0.8]	30	1.43	471.74 ± 0.26
pade32	[0.0,0.9]	35	1.38	418.78 ± 0.29	pade32	[0.0,0.9]	35	1.39	466.27 ± 0.30
pade32	[0.0,1.0]	41	1.43	416.49 ± 0.28	pade32	[0.0,1.0]	41	1.35	436.32 ± 0.15
pade32	[0.0,1.1]	44	1.37	408.18 ± 0.14	pade32	[0.0,1.1]	44	1.37	440.93 ± 0.14
pade32	[0.0,1.3]	54	1.33	414.49 ± 0.13	pade32	[0.0,1.3]	54	1.33	454.28 ± 0.13
pade32	[0.0,1.5]	61	1.35	398.89 ± 0.17	pade32	[0.0,1.5]	61	1.29	453.31 ± 0.12
pade33	[0.0,0.7]	22	1.58	407.37 ± 0.27	pade33	[0.0,0.7]	22	1.54	435.30 ± 0.24
pade33	[0.0,0.8]	29	1.47	420.65 ± 0.25	pade33	[0.0,0.8]	29	1.49	464.33 ± 0.24
pade33	[0.0,0.9]	34	1.44	387.34 ± 0.72	pade33	[0.0,0.9]	34	1.44	466.25 ± 0.30
pade33	[0.0,1.0]	40	1.48	402.12 ± 0.15	pade33	[0.0,1.0]	40	1.39	436.31 ± 0.15
pade33	[0.0,1.1]	43	1.40	401.79 ± 0.13	pade33	[0.0,1.1]	43	1.41	440.90 ± 0.14
pade33	[0.0,1.3]	53	1.36	412.96 ± 0.12	pade33	[0.0,1.3]	53	1.37	454.27 ± 0.13
pade33	[0.0,1.5]	60	1.39	393.56 ± 0.20	pade33	[0.0,1.5]	60	1.33	451.28 ± 0.12
pade43	[0.0,0.7]	21	1.65	404.74 ± 0.25	pade43	[0.0,0.7]	21	1.62	435.20 ± 0.24
pade43	[0.0,0.8]	28	1.53	422.95 ± 0.26	pade43	[0.0,0.8]	28	1.54	464.24 ± 0.24
pade43	[0.0,0.9]	33	1.47	421.31 ± 0.30	pade43	[0.0,0.9]	33	1.48	469.67 ± 0.31
pade43	[0.0,1.0]	39	1.52	416.60 ± 0.28	pade43	[0.0,1.0]	39	1.43	453.81 ± 0.30
pade43	[0.0,1.1]	42	1.45	407.28 ± 0.14	pade43	[0.0,1.1]	42	1.46	440.30 ± 0.14
pade43	[0.0,1.3]	52	1.40	412.97 ± 0.12	pade43	[0.0,1.3]	52	1.41	452.73 ± 0.13
pade43	[0.0,1.5]	59	1.42	398.89 ± 0.17	pade43	[0.0,1.5]	59	1.37	453.30 ± 0.12
pade42	[0.0,0.7]	22	1.58	407.39 ± 0.27	pade42	[0.0,0.7]	22	1.54	435.36 ± 0.24
pade42	[0.0,0.8]	29	1.47	423.01 ± 0.26	pade42	[0.0,0.8]	29	1.49	472.05 ± 0.26
pade42	[0.0,0.9]	34	1.42	421.33 ± 0.30	pade42	[0.0,0.9]	34	1.43	468.71 ± 0.30
pade42	[0.0,1.0]	40	1.48	416.63 ± 0.28	pade42	[0.0,1.0]	40	1.39	453.71 ± 0.29
pade42	[0.0,1.1]	43	1.41	408.19 ± 0.14	pade42	[0.0,1.1]	43	1.41	440.94 ± 0.14
pade42	[0.0,1.3]	53	1.37	414.49 ± 0.13	pade42	[0.0,1.3]	53	1.37	454.28 ± 0.13
pade42	[0.0,1.5]	60	1.39	398.95 ± 0.18	pade42	[0.0,1.5]	60	1.33	453.35 ± 0.12
disp	[0.0,0.7]	24	1.45	405.42 ± 0.26	disp	[0.0,0.7]	24	1.41	434.78 ± 0.23
disp	[0.0,0.8]	31	1.37	416.84 ± 0.24	disp	[0.0,0.8]	31	1.38	467.99 ± 0.24
disp	[0.0,0.9]	36	1.35	406.47 ± 0.31	disp	[0.0,0.9]	36	1.36	447.97 ± 0.70
disp	[0.0,1.0]	42	1.39	410.11 ± 0.20	disp	[0.0,1.0]	42	1.30	444.18 ± 0.26
disp	[0.0,1.1]	45	1.33	405.23 ± 0.13	disp	[0.0,1.1]	45	1.33	438.89 ± 0.14
disp	[0.0,1.3]	55	1.28	409.52 ± 0.12	disp	[0.0,1.3]	55	1.29	449.27 ± 0.12
disp	[0.0,1.5]	62	1.31	398.02 ± 0.17	disp	[0.0,1.5]	62	1.25	449.39 ± 0.16

Figure 44: Results for different fits on F6 ensemble

FIT RESULTS FOR CHIRAL EXTRAPOLATION OF a_μ

This part of the appendix shows the fit results for the chiral extrapolation.

$N_f = 2+1$ partially quenched

function	N	χ^2_{red}	A	B	C	$a_\mu/10^{-10}$
Poly (6.6)	2	16.9	590.6	1551.1	1626.5	562.9
Chiral (6.5)	2	20.2	688.0	-316.8	894.0	617.0

Table 4: Extrapolation results for $N_f = 2+1$ partially quenched

$N_f = 2$

function	N	χ^2_{red}	A	B	C	$a_\mu/10^{-10}$
Poly (6.6)	2	8.2	516.1	-1283.3	1205.7	493.1
Chiral (6.5)	2	9.7	588.9	-373.4	657.0	534.2

Table 5: Extrapolation results for $N_f = 2$

BIBLIOGRAPHY

[1] D. J. Gross and F. Wilczek. Ultraviolet behavior of non-abelian gauge theories. *Physical Review Letters*, 30(26):1343–1346, 1973.

[2] H. Wittig. QCD on the lattice. In *Theory and Experiments, Landolt-Börnstein-Group I Elementary Particles, Nuclei and Atoms, Volume A. Springer Berlin Heidelberg*, page 89, 2008.

[3] C. Gattringer and C. B. Lang. *Quantum Chromodynamics on the Lattice*. Springer, Berlin, 1st edition, 2010.

[4] I. Montvay and G. Münster. *Quantum Fields on a Lattice*. Cambridge University Press, 1994.

[5] J. Smit. *Introduction to Quantum Fields on a Lattice*. Cambridge University Press, 2002.

[6] M. Creutz. *Quarks, gluons, and lattices*. Cambridge University Press, 1983.

[7] H. B. Nielsen and M. Ninomiya. A no-go theorem for regularizing chiral fermions. *Physics Letters B*, 105(2-3):219 – 223, 1981.

[8] K. G. Wilson. Confinement of quarks. *Phys. Rev. D*, 10(8), 1974.

[9] K. Symanzik. Continuum limit and improved action in lattice theories : (I). Principles and [phi]4 theory. *Nuclear Physics B*, 226(1):187 – 204, 1983.

[10] K. Symanzik. Continuum limit and improved action in lattice theories : (II). O(N) non-linear sigma model in perturbation theory. *Nuclear Physics B*, 226 (1):205 – 227, 1983.

[11] B. Sheikholeslami and R. Wohlert. Improved continuum limit lattice action for QCD with wilson fermions. *Nuclear Physics B*, 259(4):572 – 596, 1985.

[12] L. Susskind. Lattice fermions. *Phys. Rev. D*, 16(10):3031–3039, 1977.

[13] H. Neuberger. Exactly massless quarks on the lattice. *Physics Letters B*, 417 (1-2):141–144, 1998.

[14] H. Neuberger. More about exactly massless quarks on the lattice. *Physics Letters B*, 427(3-4):353–355, 1998.

[15] D. B. Kaplan. A method for simulating chiral fermions on the lattice. *Physics Letters B*, 288(3-4):342 – 347, 1992.

[16] A. Shindler. Twisted mass lattice QCD. *Physics Reports*, 461(2-3):37–110, 2008.

[17] P. Hasenfratz. Prospects for perfect actions. *Nuclear Physics B*, 63(1-3):53 – 58, 1998.

[18] C. T. Sachrajda and G. Villadoro. Twisted boundary conditions in lattice simulations. *Phys. Lett.*, B609, 2005.

[19] J.M. Flynn, A. Jüttner, C.T. Sachrajda, P.A. Boyle, and J.M. Zanotti. Hadronic form factors in lattice QCD at small and vanishing momentum transfer. *Journal of High Energy Physics*, 2007:016, 2007.

[20] N. Metropolis, A.W. Rosenbluth, M.N. Rosenbluth, A.H. Teller, E. Teller, et al. Equation of state calculations by fast computing machines. *The Journal of chemical physics*, 21(6):1087, 1953.

[21] S. Duane et al. Hybrid Monte Carlo. *Physics Letters B*, 195(2):216 – 222, 1987.

[22] L.D. Debbio, L. Giusti, M. Lüscher, R. Petronzio, and N. Tantalo. QCD with light Wilson quarks on fine lattices (II): DD-HMC simulations and data analysis. *Journal of High Energy Physics*, 2007:082, 2007.

[23] L.D. Debbio, L. Giusti, M. Lüscher, R. Petronzio, and N. Tantalo. QCD with light wilson quarks on fine lattices (I): first experiences and physics results. *Journal of High Energy Physics*, 2007:056, 2007.

[24] F. Jegerlehner and A. Nyffeler. The muon g-2. *Phys. Rept.*, 477(1-3):1–110, 2009.

[25] C. Amsler et al. (PARTICLE Data Group). The muon anomalous magnetic moment. *Physics Letters B*, 667, 1 (2008) and 2009 partial update for the 2010 edition.

[26] G. W. Bennett et al. Final report of the E821 muon anomalous magnetic moment measurement at BNL. *Phys. Rev. D*, 73(7):072003, 2006.

[27] J. Schwinger. On Quantum-Electrodynamics and the Magnetic Moment of the Electron. *Phys. Rev.*, 73(4):416–417, 1948.

[28] B.L. Roberts. Status of the fermilab muon (g-2) experiment. *Arxiv preprint arXiv:1001.2898*, 2010.

[29] M. Tsutomu. New g-2 experiment at J-PARC. *Chinese Physics C*, 34:745–748, 2010.

[30] M. Davier. New results on the hadronic vacuum polarization to the muon g-2. *Arxiv preprint arXiv:1001.2243*, 2010.

[31] M. Göckeler et al. Vacuum polarisation and hadronic contribution to muon g-2 from lattice QCD. *Nucl. Phys.*, B688, 2004.

[32] T. Blum. Lattice calculation of the lowest order hadronic contribution to the muon anomalous magnetic moment. *Phys. Rev. Lett.*, 91, 2003.

[33] C. Aubin and T. Blum. Calculating the hadronic vacuum polarization and leading hadronic contribution to the muon anomalous magnetic moment with improved staggered quarks. *Phys. Rev.*, D75, 2007.

[34] D.B. Renner and X. Feng. Hadronic contribution to g-2 from twisted mass fermions. *Arxiv preprint arXiv:0902.2796*, 2009.

[35] M. Creutz. Comments on staggered fermions / Panel discussion. *PoS*, CONFINEMENT8:016, 2008.

[36] A. Jüttner and M. Della Morte. New ideas for g-2 on the lattice. *PoS*, LAT2009, 2009.

[37] W. Kürzinger. *Untersuchung der Vakuumpolarisation auf dem Gitter*. PhD thesis, Freie Universität Berlin, 2001.

[38] J. C. Ward. An identity in Quantum Electrodynamics. *Phys. Rev.*, 78(2):182, Apr 1950.

[39] Y. Takahashi. On the generalized ward identity. *Nuovo Cim.*, 6, 1957.

[40] K. Gallivan, A. Sameh, and Z. Zlatev. Solving general sparse linear systems using conjugate gradient-type methods. *ACM SIGARCH Computer Architecture News*, 18(3b):132–139, 1990.

[41] K. Jansen and R. Sommer. O (a) improvement of lattice QCD with two flavors of Wilson quarks. *Nuclear Physics B*, 530(1-2):185–203, 1998.

[42] M. Lüscher. Schwarz-preconditioned HMC algorithm for two-flavour lattice QCD. *Comput. Phys. Commun.*, 165:199–220, 2005.

[43] M. Lüscher. Computational Strategies in Lattice QCD. *ArXiv e-prints*, 2010.

[44] M. Lüscher. Solution of the dirac equation in lattice QCD using a domain decomposition method. *Computer physics communications*, 156(3):209–220, 2004.

[45] B. Knippschild. private communication.

[46] K. Nakamura et al. (PARTICLE Data Group). Summary tables. *Journal of Physics G*, 37, (2010) Cut-off date for this update was January 15, 2010. URL http://pdg.lbl.gov/2010/tables/contents_tables.html.

[47] J.J. Moré, D.C. Sorenson, B.S. Garbow, and K.E. Hillstrom. The MINPACK project. *Sources and Development of Mathematical Software*, pages 88–111, 1984.

[48] S. Kirkpatrick et al. Optimization by simulated annealing. *Science*, 220 (4598):671, 1983.

[49] Wolfram Research Inc. Mathematica, technical and scientific software, September 2010. URL http://www.wolfram.com/.

[50] G. Golub and W. Kahan. Calculating the singular values and pseudo-inverse of a matrix. *Journal of the Society for Industrial and Applied Mathematics: Series B, Numerical Analysis*, pages 205–224, 1965.

[51] E. Golowich and J. Kambor. Two-loop analysis of vector-current propagators in chiral perturbation theory. *Nuclear Physics B*, 447(2-3):373–404, 1995.

[52] J. Gasser and H. Leutwyler. Chiral perturbation theory to one loop* 1. *Annals of Physics*, 158(1):142–210, 1984.

[53] Free Software Foundation. *GNU Scientific Library Reference Manual - Third Edition*. Network Theory Ltd., 2009. ISBN 0954612078.

[54] Free Software Foundation. GSL - GNU Scientific Library, August 2010. URL http://www.gnu.org/software/gsl/.

[55] U. Wolff. Monte Carlo errors with less errors. *Arxiv preprint hep-lat/0306017*, 2003.

ACKNOWLEDGMENTS

This diploma thesis was supported by many people. I would like to use this opportunity to thank:

- First of all my supervisor Prof. Hartmut Wittig, for his guidance and helpful discussions during the research. In addition for providing the necessary computing power on the Wilson cluster.
- My parents Reiner and Vera Jäger for their unconditional support during the whole course of studies and their encouragement to study physics.
- My colleagues and especially Bastian Brandt, Georg von Hippel, Andreas Jüttner, Bastian Knippschild, Michele Della Morte and Björn Walk for their patience with any open question. Additionally Dalibor Djukanovic for his support using the Wilson cluster.
- My fellow students and friends especially Steffen Dörner, Jennifer Mutschall, Andreas Neiser, Fabian Nillius and Björn Walk for their encouragement and proofreading of this diploma thesis.
- André Miede for providing the classicthesis style.

DECLARATION

Ich versichere hiermit, dass ich die Arbeit selbständig verfasst und außer den in der Arbeit angegebenen keine anderen Hilfsmittel und Quellen benutzt habe.

Mainz, 23.09.2010

Benjamin Jäger